

UNIVERSITÀ DEGLI STUDI DI MILANO

FACOLTÀ DI SCIENZE E TECNOLOGIE

CORSO DI LAUREA IN CHIMICA



**SYNTHESIS AND CHARACTERIZATION OF
METAL-ORGANIC FRAMEWORKS WITH OPEN
METAL SITES FOR WATER HARVESTING**

SUPERVISOR: PROF.SSA VALENTINA COLOMBO

CO-SUPERVISOR: DR. LUCA BRAGLIA

AUTHOR: DOMITILLA ALESSANDRA ALOI

N° MATRICOLA 943090

ACADEMIC YEAR 2021-2022

Elettrone

*Etereo fermione
in armonico stato,
una direzione
hai specificato.*

*Ruotando fissato,
in un cono fermato,
in armoniche vuote
ti sei rivelato.*

*Di modulo noto
tu resti ignoto.*

D. A.

Index

CHAPTER 1 MOFS: METAL ORGANIC FRAMEWORKS	1
1.1 TERMINOLOGY	1
1.2 EARLY STUDIES	2
1.3 EVOLUTION OF RETICULAR CHEMISTRY	2
1.4 PROPERTIES AND APPLICATIONS	3
1.5 SYNTHESIS ROUTES	5
CHAPTER 2 WATER HARVESTING	7
2.1 WATER STABILITY OF MOFS	7
2.2 WATER HARVESTING FROM AIR	9
CHAPTER 3 PURPOSE OF THE THESIS	16
CHAPTER 4 SYNTHESIS AND PXRD&IR CHARACTERIZATION OF TARGET MOFS	17
4.1 CO AND MN MOF-74	17
4.2 FE MIL-100	32
CHAPTER 5 ADVANCED SYNCHROTRON RADIATION TECHNIQUES	38
5.1 XPS: X-RAY PHOTOELECTRON SPECTROSCOPY	39
CHAPTER 6 XPS CHARACTERIZATION OF SYNTHESIZED SAMPLES	42
6.1: (MN) AND (CO) MOF-74	42
6.2 (FE)-MIL-100	52
CHAPTER 7 EXPERIMENTAL SECTION	57
7.1 INSTRUMENTAL CHARACTERISTICS	57
7.2 SUPPLEMENTARY IR SPECTRA	58
CHAPTER 8 CONCLUSIONS AND FUTURE PROJECTS	59
8.1 CONCLUSIONS	59
8.3 FUTURE PROJECTS	60
GREETINGS	61
BIBLIOGRAPHY	62

Chapter 1

MOFs: Metal Organic Frameworks

MOFs or Metal Organic Frameworks are relatively new organic-inorganic hybrid materials that consist of a regular array of positive metal ions connected by organic 'linker' molecules to create a periodic and crystalline structure.

They have been widely studied in the last past two decades for their promising properties (such as porosity, gas adsorption and storage, flexibility/rigidness, low density...) and chemical tunability [1].

1.1 Terminology

To aid understanding various terms have been defined as follows, according to IUPAC recommendations:

- **Coordination polymer:**
«A coordination compound with repeating coordination entities extending in 1, 2, or 3 dimensions».[2]. Note that, according to IUPAC definition; coordination polymers do not need to be crystalline [2]
- **Coordination network:**
«A coordination compound extending, through repeating coordination entities, in 1 dimension, but with cross-links between two or more individual chains, loops, or spiro-links, or a coordination compound extending through repeating coordination entities in 2 or 3 dimensions» [2]. A coordination network is, in fact, a subset of coordination polymer.
- **Metal organic framework:**
«A metal–organic framework, abbreviated to MOF, is a coordination network with organic ligands containing potential voids» [2]. Note that, according to this definition, it is not required that a MOF be crystalline. However, it is common to ascribe crystalline properties to MOFs by definition [3].

1.2 Early studies

In the year 1999 two articles were published about two new and highly porous materials: MOF-5[4] and HKUST-1[5] (fig. 1.1). In both cases the new material was a periodic combination of inorganic metal ion clusters with organic linkers into a 3D channelled structure, stable to high temperatures and easy to functionalize. They were both referred to as “MOF”.

Before MOFs, common and known porous materials were for example inorganic zeolites (inorganic aluminosilicates solids made up by the periodic repetition of $[\text{SiO}_4]^{4-}$ and $[\text{AlO}_4]^{5-}$) or active carbons. Although those materials combine nano-porosity with high thermal stability, they are difficult to derivatize in a systematic way [6]. MOFs, instead, have the potential for more flexible rational design through the control of the architecture and functionalization of the pores [4].

For example, in the field of water adsorption, the water uptake of classical desiccants (e.g., CaCl_2 , silica gel, or zeolites) is high but their strong affinity to water makes their regeneration energy intensive, while MOFs can be tailored for a reversible water adsorption with low energy regeneration by proper functionalization of the framework structure [4].

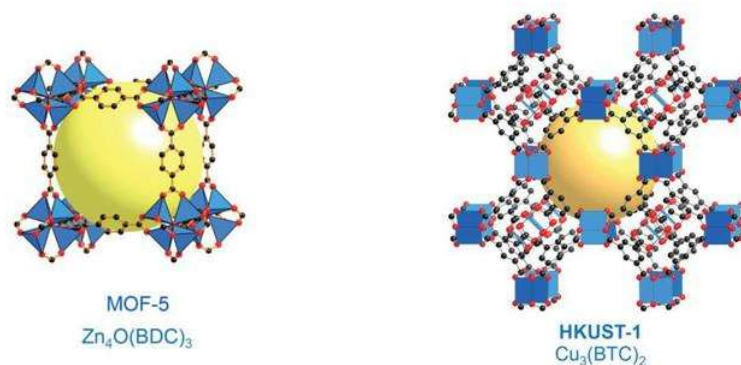


Fig. 1.1: MOF-5 and HKUST-1 structures. In HKUST-1 (right) Cu paddlewheel secondary building units (SBUs) are coordinated via 1,3,5-benzenetricarboxylate (BTC) to form three-dimensional porous cubic networks, MOF-5 (left) consists of Zn_4O clusters connected to ditopic linear BDC linkers [7]

1.3 Evolution of reticular chemistry

Reticular chemistry (based on the Latin *reticulum*: small net) is concerned with linking molecular building blocks through strong bonds to form porous crystalline 1D, 2D and 3D frameworks in a designed manner. At the dawn of the field, structures with such properties

(strong bonds, porosity, crystalline) were very rare and challenging to make. One important reason was the disconnection between solid state organic and inorganic chemistry.

Organic synthesis forms strong covalent bonds that enable the multistep pathways that lead to precise complex organic molecules or polymers, however the crystallization into extended 2D or 3D structure is complicated. On the other hand, inorganic synthesis is often carried under thermodynamic control in a single step and creates crystalline 2D or 3D structure. However, it's difficult to control the size and shape of the product and it's more likely to obtain a dense crystal [1].

Early reported coordination polymers mixed inorganic metal ions and organic linkers [8], but they were often simple solids whose structure showed one metal ion node bonded to the organic linkers with pure electrostatic (weak) coordinative bonds (usually M-N), so they easily collapsed when guest molecules inside their pores got removed [9].

In contrast, recent MOFs are linked through strong and directional bonds: organic units are ditopic or polytopic organic carboxylates (and other similar negatively charged molecules) linked to metal-containing units. The resulting structure is architecturally robust and stable against the removal of the guest molecules, thus enabling permanent porosity and high surface area [10] (examples are MOF-74 series [11], MIL-100 [12] and 101 [13], [14], HKUST-1 [5] etc).

1.4 Properties and applications

MOFs owe their appeal to the variety of properties they can show and specifically to the tunability of such properties. Without doubts, the principal one is their inherent porosity and thus high surface area, which make them perfect materials for gas storage, gas separation, catalysis, sensing, drug delivery and more. Typically, all the phenomena happening inside the pore structure of MOFs are highly influenced by the pore size. In the case of gas storage, indeed selectivity, capacity, and reversibility of the adsorption process are directly correlated with this parameter [15]–[17].

As the other porous solids, MOFs are divided into three categories according to their pore size [15]:

- Microporous: pore size below 20 Å
- Mesoporous: pore size between 20 and 500 Å
- Macroporous: pore size above 500 Å

Each of these three categories, thanks to the different properties, finds applications in different processes.

In recent years, within the enormous plethora of MOFs systems known, the one featuring open metal sites (OMS) have witnessed great interest. OMSs are coordination vacancies in the coordination sphere of the metal atoms. These can be naturally present in the framework or being introduced following activation procedures or the formation of defects. An example is provided by MIL-100(Fe) MOFs which, upon activation, features three Fe^{3+} OMS in its inorganic building unit (fig 1.2).

The presence of metal atoms directly facing into the pores structure of MOFs can be exploited to build better performing materials for different physicochemical processes. For example, in the case of gasses adsorption, the direct interaction between guest molecules and metal d-orbitals can induce high selectivity towards specific types of molecules. Long *et Al* has shown in the case of Fe-BTTri ($\text{Fe}_3[(\text{Fe}_4\text{Cl})_3(\text{BTTri})_8]_2 \cdot 18\text{CH}_3\text{OH}$, $\text{H}_3\text{BTTri} = 1,3,5$ -tris(*1H*-1,2,3-triazol-5-yl)benzene)) how the direct interaction between Fe and CO molecules enhances its selective adsorption towards different gasses thanks to a spin crossover mechanism taking place at the iron sites [18].

Nevertheless, MOFs featuring open metal sites also find applications in catalysis. Indeed, the OMSs' chemical environment can be easily functionalized, tuning the electrochemical situation of metal sites involved in catalytical reactions with guest molecules. To date, many different catalytic processes are performed using MOFs as heterogenous catalysts, consequently achieving the annexed advantages [19], [20].

Although the great benefits coming from having OMSs, undercoordinated metal sites inside a metal-organic structure often induce lower stability of the framework, especially in humid conditions [21]. Water molecules can strongly bind metal sites creating strong interactions that can perturbate the framework geometry and stability.

Studying exposed metal-water interactions in water-stable MOFs can then improve the comprehension of the structural-electronic changes associated with this phenomenon.

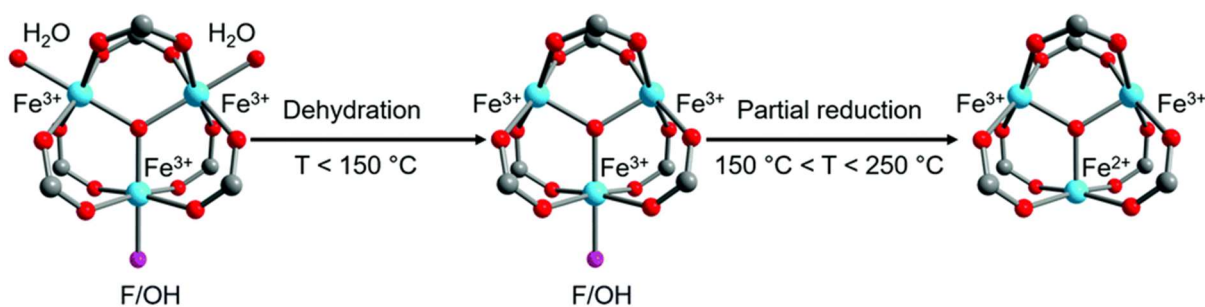


Fig. 1.2: Formation of open Fe^{3+} sites and Fe^{2+} site in an octahedral iron trimer of MIL-100(Fe) by dehydration and partial reduction through the removal of the anionic ligand [22].

The work presented here focuses on three different MOFs with OMS describing their synthesis procedure and characterization via X-ray-based experiments under different humid atmospheres.

1.5 Synthesis routes

MOFs are most synthesized following a *solvothermal* approach which consists of combining a solution of the ligand with a solution of the metal and heating the mixture via conventional electrical methods [23].

Although easy from a practical point of view, synthesizing MOFs following solvothermal methods often comes with many problems. Due to the many variables involved in a solvothermal synthesis, precise control of outcomes is challenging. It is still not completely clear how each parameter affects the result making it hard to predict the best conditions to obtain the desired compound.[24] For these reasons, the single-step route implies an accurate control of all the variables that occur during the reaction such as:

- Temperature
- Concentration of solutes
- pH
- Stirring
- Molar ratio between metal and linker
- Chosen solvents

Using pre-built inorganic building blocks instead of free metal ions may help achieve the target [23]. Here is the convenience of the reticular chemistry's approach of deconstructing the target MOFs into their topology nets. Topology nets originates from the combination of SBUs and ligands both modeled into geometric simple shapes. Each net is identified by a 3-letter acronym (fig. 1.3).

Over the years, other synthetic methodologies have been investigated as alternatives to the thermodynamically controlled solvothermal method, such as microwave-assisted, electrochemical, sonochemical, mechanochemical, and spray-drying synthesis[23].

Moreover, in recent times, *green syntheses* started to attract the interest of many. Due to the current and spreading social awareness on environmental issues such as pollution, over-exploitation of natural sources, shortage of raw materials, and climate change, the importance of new solvent-free non-toxic synthetic strategies is growing. Green syntheses aim to limit the use of organic solvents that are often toxic and difficult to dispose of and to use mild conditions such as room temperature and pressure [25]–[28]. Examples are the water-based synthesis of MOF-74 [28] or solvent-free mechanochemical synthesis of Fe MIL-100 [25].

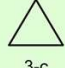




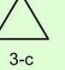

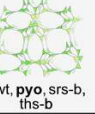


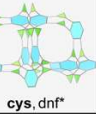


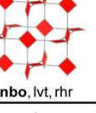
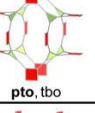
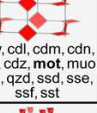
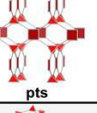
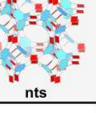
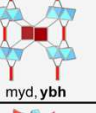

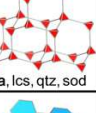
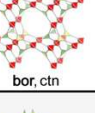
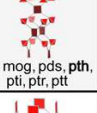


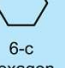
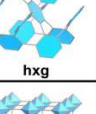
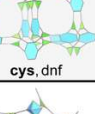
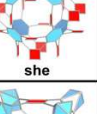
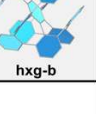

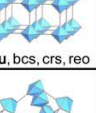
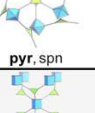
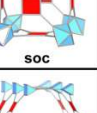
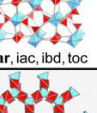
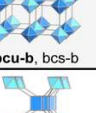
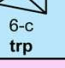
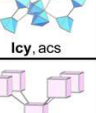
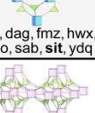
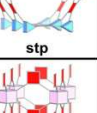
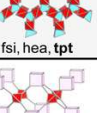
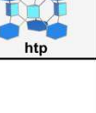
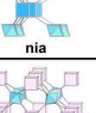
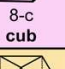
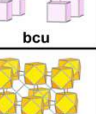
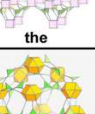
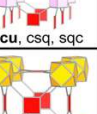
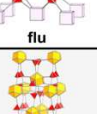
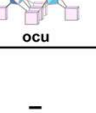

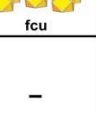

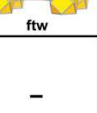
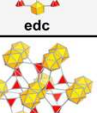


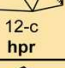
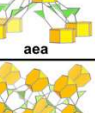
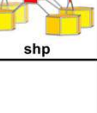
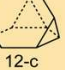
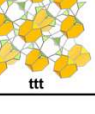
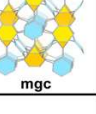
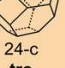
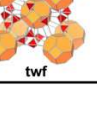
Building unit 1 \ Building unit 2	— 2-c Linear	 3-c Triangle	 4-c Square	 4-c tet	 6-c Hexagon	 6-c oct
 3-c Triangle	 srs	 bwt, pyo, srs-b, tns-b	 fjh, fmj, gee, iab, yac, yao	 asn, ept, ofp	 cys, dnf*	 anh, ant, apo, brk, cep*, cml, czz, eea, qom, rti, tsx, zzz
 4-c Square	 nbo, lvt, rhr	 pto, tbo	 cev, cdl, cdm, cdm, cds, cdz, mo*, muo, qdl, qzd, ssd, sse, ssf, sst	 pts	 nts	 myd, ybh
 4-c tet	 dia, lcs, qtz, sod	 bor, ctn	 fgl, mog, pds, pth, pti, ptr, ptt	 bnl, byl, cag, cbt, coe, crb, fel, icm, kea, lon, pcl, qtz-b, sca, tpd, ucn	—	 alw, bix, cor, ing, spl, toc
 6-c Hexagon	 hxg	 cys, dnf	 she	—	 hxg-b	—
 6-c oct	 pcu, bcs, crs, reo	 pyr, spn	 soc	 gar, iac, ibd, toc	—	 pcu-b, bcs-b
 6-c trp	 lcy, acs	 ceq, dag, fmz, hwx, moo, sab, sit, ydq	 stp	 fsi, hea, tpt	 htp	 nia
 8-c cub	 bcu	 the	 scu, csq, sqc	 flu	—	 ocu
 12-c cuo	 fcu	 sky	 ftw	 edc	—	—
 12-c ico	—	—	—	 ith	—	—
 12-c hpr	—	 aea	 shp	—	—	—
 12-c tte	—	 ttd	—	—	 mgc	—
 24-c tro	—	—	—	 twf	—	—

Fig. 1.3: Topology nets originated from the combination of geometric building units of ligands and metals. Most MOFs show simple nets while fewer structures are known to take complex nets. Moreover, many combinations are still not explored, no MOFs are known which take them, thus leaving room for researchers to challenge themselves in their realization [29].

Chapter 2

Water harvesting

2.1 Water stability of MOFs

A water stable MOF is one which retains its structure and configuration when exposed to water molecules. Instead, it is unstable if it loses its crystallinity and assumes an amorphous structure. As described in paragraph 1.4, the presence of exposed metal sites facing the pores can induce greater sensibility to water molecules, increasing the risk of water-driven degradation of the framework.

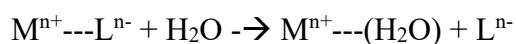
2.1.1 Degradation mechanisms

M. Yaghi *et al.* has proposed the following mechanism for the decompositions of MOFs systems through water interactions [30].

- **Hydrolysis:** the metal-ligand bond is broken by the insertion of OH⁻ anion on the metal cation leading to the formation of a hydroxylated cation and a protonated ligand:



- **Ligand displacement:** an H₂O molecule replaces the ligand leading to a hydrated cation and to the release of a free ligand molecule:



Here, the interaction of water molecules with metal centres is the starting point for a sequence of chemical reactions which lead to the formation of metal-aqua complex or metal oxides. Moreover, it was suggested that clusters of water molecules around the SBU drives the degradation of MOFs [31]. Water not only plays an important role in replacing the linker, but additional water molecules stabilize, by solvation, the hydrolyzed SBU as well as the expelled linker [28].

2.1.2 Improving water stability

As depicted in the previous paragraph, the weakest bond inside MOFs is often the metal-ligand bond [30]. To increase the water stability of MOFs it is necessary to increase the strength of this interaction or, as said, to protect the metal centres from the adsorption of water molecules. Another well exploited technique, indeed, is to increase the kinetical stability of the metal ligand bond meaning to protect it from the interaction with other guest molecules.

Thermodynamic stability

The prediction of the strength of the interaction between transition metals (often present in MOFs) and linkers is generally described recalling Hard and Soft acids and bases theory [33], [34]. According to this principle most stable bonds are formed coupling hard-hard/weak-weak pairs of acids and bases. The strength of their interaction is therefore governed by the basicity/acidity as well as by the polarizability of deprotonated linker and metal ions [33], [34]. Between the most stable MOFs therefore we find UiO family (made up by Zr^{4+} clusters and carboxylate linkers) and the azolate frameworks based on soft metals (Cu, Ni, Zn etc.) [35], [36].

Kinetic stability

Another common strategy to increase the stability of the framework regards the protection of the inorganic building units. In this case, in fact, it is kinetic stability that occurs when H_2O molecules cannot physically reach the metal centres [30]. This is usually achieved through two main strategies [30]:

- exploiting highly interconnected inorganic SBUs to prevent any possible interaction between the water molecules and the metal cluster (fig. 2.1).
- exploiting the high chemical tunability of the MOF structure thanks to which is possible to functionalize the organic linkers. Typically, hydrophobic organic pendants or functional groups are employed to build a water-repellent pocket around metal sites avoiding their contact with water guests. Another possibility is introducing hydrophilic groups far away from the metal centres, thus capturing water away from the SBUs.

Both strategies typically induce a diminished pore volume of the framework affecting consequently the adsorption capability of the material and its applicability.

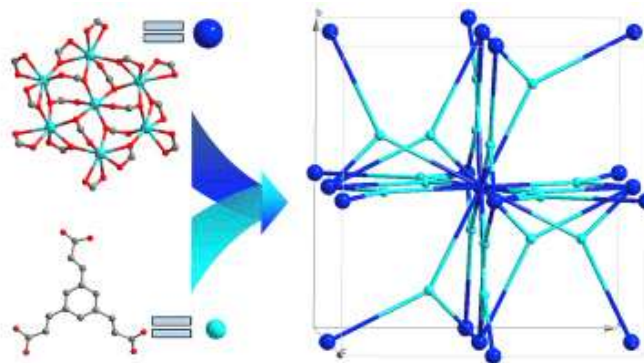


Fig. 2.1: example of highly connected SBU [37].

2.2 Water harvesting from air

The water vapour in the earth's atmosphere equals to about 10% of all liquid freshwater resources of the planet [30]. In many arid regions it is the richer source of water. Therefore, creating new water-adsorption devices able to produce fresh water would help solving the global water problem. As previously described, conventional desiccants or porous materials (as zeolites, porous carbons, CaCl_2 ...) often show energy intensive regeneration temperature or low capacity. MOFs, instead, are porous materials that can be tailored for a reversible water adsorption with low energy regeneration and high capacity, hence, they are promising materials in the research for developing new water harvesting devices.

2.3.1 Parameters

For clarity of exposure, here are some parameters used in water adsorption studies:

- CH_2O is the adsorption capacity that is the ratio of cm^3 of adsorbed water per grams of MOF sample [33].
- \mathbf{a} is the relative pressure P/P° (P° is the saturated vapour pressure at 298 K) at which half of the total capacity is reached [33].
- **Temperature and Pressure ranges** are ranges in which the adsorption takes place.
- **RH** or relative humidity is the amount of water vapor in air expressed as a percentage (%RH) of the amount needed to achieve saturation at the same temperature.

2.3.2 Ideal properties of adsorbent MOFs

As said, MOFs are promising systems for water harvesting applications. Thanks to their porous nature and to their chemical tunability it is possible to build appropriate materials exploiting the principles of reticular chemistry.

In particular, in the selection of the adsorbent material for water, according to Kalmutzki *et al.* [30], it is necessary to evaluate:

- **Water stability:** as already discussed, adsorbent materials must show high water stability in order to be employed in industrially relevant processes.
- **Cycling stability** (the stability under many adsorption-desorption cycles): in order to be used repeatedly in water harvesting devices, the material must exhibit a high cycling stability.
- **CH₂O** (maximum water capacity): a high maximum water capacity is desirable for more efficient water collection.
- **Temperature and pressure ranges** (ranges in which the material adsorbs and releases water): a steep water uptake in a narrow pressure region between 10 and 30% RH (i.e., Type IV or V isotherm with a small value for α) facilitates water adsorption at low relative pressures (i.e., low RH), while allowing for regeneration under mild conditions [30]. Moreover, a huge difference in the water uptake at high and low temperatures (low uptake for high T) would allow for an efficient temperature-depending water adsorption and desorption cycle.
- **Kinetics of the adsorption-desorption process:** relatively fast adsorption and desorption process at the working temperatures and pressures are desirable.
- **Thermic conductivity and heat capacity** (for thermally induced desorption devices only): high thermal conductivity and relatively low heat capacity allow for short response times with respect to temperature changes[30]. MOFs usually show low heat capacity due to their open structure [30].

To date, although many known MOFs show promising properties, none of them satisfies all the cited requirements. Fig 2.2 shows a comparison of water adsorption properties of the most known systems studied for this application.

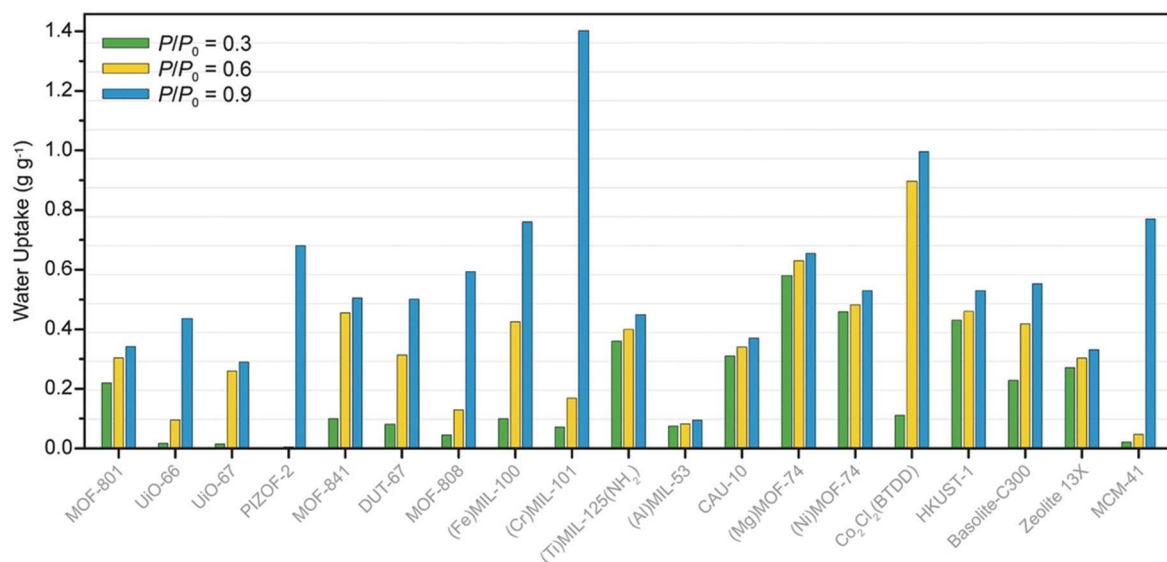


Fig. 2.2: Comparison of the water uptake of different porous materials at $P/P_0 = 0.3, 0.6,$ and 0.9 . A high water uptake at low relative pressures is desirable since it results in strong binding but also allows desorption under mild conditions [30]

2.3.3 Influence of ligands' structure on adsorption properties

In the search for better performing materials towards water harvesting applications various strategies have been developed to better satisfy the aforementioned requirements.

In particular, introducing hydrophilic groups on the ligand side (i.e., $-NH_2$, heteroatoms...) induces hydrophilic properties to the pores of the MOF and lowers the relative pressure α , so water is adsorbed also at lower pressures and the MOF is saturated at lower humidity [38]. At the same time, the maximum H_2O water capacity, which depends on free pore volume, would be reduced by applying this strategy, especially when functionalising with bulky hydrophilic groups [33].

On the other hand, the larger and longer the ligand is, the larger the pores are and higher the capacity is. Ligand expansion is often applied trying to obtain better guest molecules uptakes. The major difficulty encountered applying this strategy is the stability of the framework: the augmented dimension of the linker usually enhances the risk of structural collapsing after solvent removal and of framework intercalation, reducing the available pore volume. Moreover, pores too large tend to increase the risk of capillary condensation and hysteresis in the water cycling adsorption-desorption isotherm [30].

2.3.4 Influence of the metallic SBUs

Heavy metals usually generate highly charged cations hence strong M-L bonds and water stable MOFs. However, they show a high specific weight, so they lower the capacity of MOFs that contain them (calculated as cm^3 of water per grams of MOF sample) [30].

Not less important is the toxicity of the metals because, in the view of exploiting MOFs for drinking water harvesting, it should be considered that after repeated cycles of use the material may release metals into the harvested water. Therefore, for drinking water it is better to use low toxic metals as Al and Fe [30].

2.3.5 Influence of defects

Another known strategy to increase water uptakes is the defect introduction. It has been observed that MOFs with defects show a greater hydrophilicity and higher capacity than the defects-free ones, probably because defects create small additional hydrophilic pores in which water can fill and increase the pore volume [38] [39], [40].

For example, according to H. Furukawa *et al*, defective MOF-801 showed a maximum water uptake 1.3 times greater than the single crystal and defects-free MOF-801 sample [40]. This difference in maximum uptake between the two forms of MOF-801 was also observed in the N_2 sorption measurements and was ascribed to the presence of defects in the powder form [40].

Another example regards the case of defective UiO66: simulated adsorption isotherms for water showed significant changes depending on the concentration of defects [39]. Indeed, the presence of defects in the form of missing linkers makes this MOF more hydrophilic [39]. This was deduced by calculating adsorption heats: for the ideal UiO-66 adsorption heat increased sharply with water uptake (hydrophobic behaviour) while for the UiO-66 with defects it decreased at higher water loadings (hydrophilic behavior).

2.3.6 Scheme of a passive water harvesting device

An ideal water harvesting device is one that makes use of an adsorbent with high capacity and that exploits a renewable, low grade and abundant source of energy, as solar-thermal energy, in order to potentially allow its deployment in households, especially those located in sunny arid places [41].

The process through which such devices produce fresh water follows three main steps [30]:

1. **Adsorption** of water from air at low temperatures and high RH
2. **Desorption** at high temperatures
3. **Condensation** at low temperatures

A simple scheme of a passive water harvesting device is illustrated in fig. 2.3: a box is equipped with an adsorbent MOF layer and a condenser on opposite sites. First step, box open, is the adsorption of water by the adsorbent exposed to cool humid air (i.e. 20°C and 20% RH) with release of adsorption heat to the environment. These conditions are common during the night in hot desert areas. In the second step, the adsorbent saturated, box is closed and the temperature increases (i.e. solar heating during day time), the adsorbent releases water vapour inside the box, increasing the RH. Finally, cooling the air close to the condenser up to the dew point (100% RH) generates liquid water ready to use, while condensation heat is released to the environment.

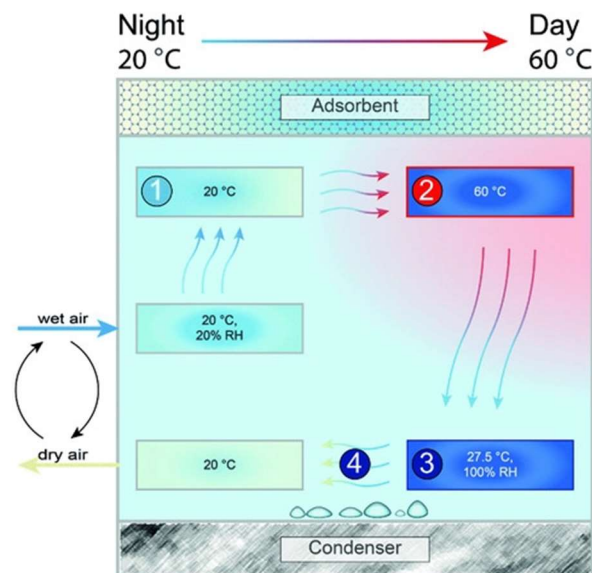


Fig. 2.3: Scheme of a passive water-harvesting device. The MOF is saturated with at 20 °C (20% RH, night conditions, point 1); subsequent heating during the day regenerates the MOF (point 2); the humidity ratio inside the device is increased until 100% RH is reached close to the condenser (point 3). Water condenses (point 4) and the dry air is exchanged by humid air again to close the cycle [30]

An example of such apparatus is the one studied by Yaghi *et al.* where MOF-801 has been used as an adsorbent layer [41]. Once water vapor is adsorbed into the MOF, solar energy was used to release the adsorbate. Water was then harvested using a condenser maintained at temperatures near that of the surrounding environment. For MOF-801, a temperature swing between 25° and 65°C can harvest more than 0.25 liters kg⁻¹ at >0.6 kPa vapor pressure (20% RH at 25°C) [41]. A photo of the device developed by Yaghi *et Al.* is illustrated in fig. 2.4 [41].

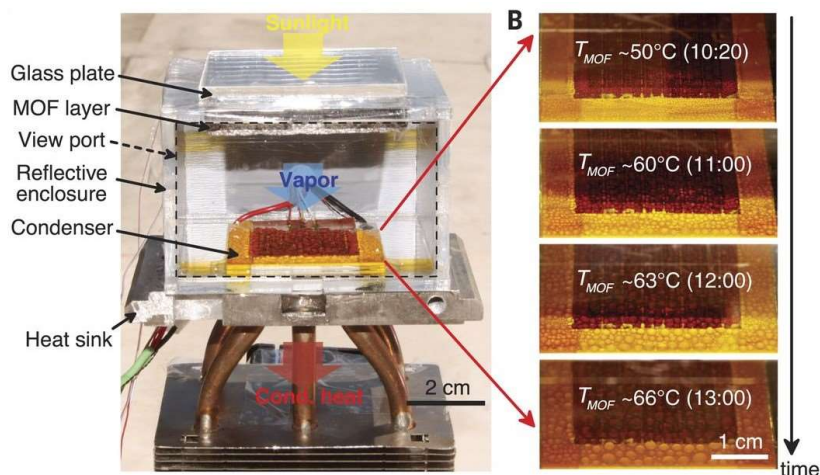


Fig. 2.4: Image of a water-harvesting prototype with activated MOF-801 with a weight of 1.34 g, a packing porosity of ~ 0.85 , and outer dimensions of 7 by 7 by 4.5 cm [41].

MOF-801 is a Zr based MOF with fumarate as organic linker. The structure features two types of tetrahedral pores (5.6 Å and 4.8 Å across) and one octahedral pore that has a diameter of about 7.4 Å (fig. 2.5). Such small pores are optimal for the adsorption of small molecules as water molecules [42].

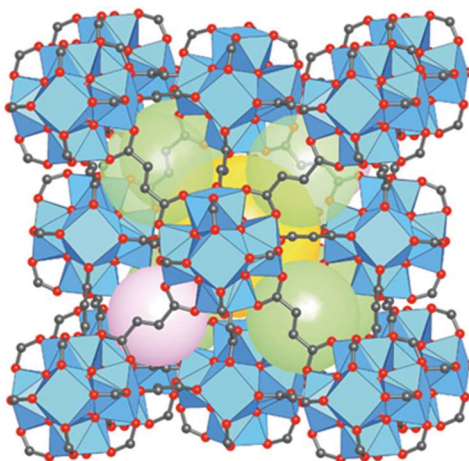


Fig. 2.5: structure of MOF-801 illustrating three different cavities, two of which are tetrahedral (green and pink spheres) and one of which is octahedral (yellow sphere) [30]

More recently Yaghi *et al* has reported another system, MOF 303 which has shown promising properties for the adsorption of water [43]. Thanks to a multi-technique approach they were able to deeply characterize the water adsorption mechanism in MOF-303 highlighting the role of the metal sites.

MOF303 is an aluminium based MOF obtained by coupling PZDC linkers and aluminium octahedra. The resulting structure features two type of pockets. The first one, due to the presence of polar organic linkers, is a hydrophilic one (fig. 2.6) and facilitate the adsorption of water while the second one possesses hydrophobic properties thanks to the relative arrangement of the organic linkers. This pore-configuration makes the material particularly interesting for water adsorption applications. Through *in situ* SC-XRD (Single Crystal X-ray diffraction) it has been possible to locate the first binding site of water inside the pore structure. This appears to be near the aluminium metal sites thanks to which first adsorbed water molecules act as nucleation sites for the following water molecules. By the use of the same technique was also possible to confirm the desorption of water in the hydrophobic pores which, due to their nature, would be the first sites hosting the desorption of water molecules.

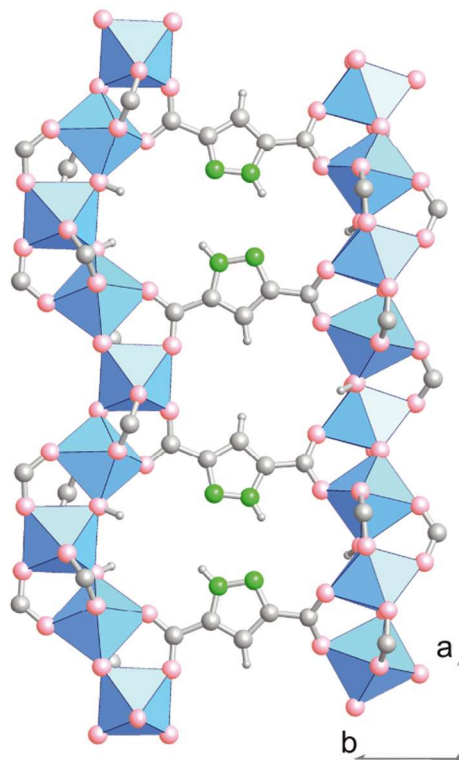


Fig. 2.6: side view visualizing two hydrophilic pockets defined by a pair of pyrazole-based linkers with their nitrogen atoms (green) pointing toward each other and flanked by two aluminum oxide rod-like SBUs [43]

As seen, the use of protected inorganic SBUs has hindered the water-guided degradation of the frameworks allowing the use of this material for water harvesting applications. Again, also in this case the deep comprehension of the water adsorption sites and the understanding of the metal-water interactions reveals to be a key point for the development of better performing materials.

Chapter 3

Purpose of the thesis

Purpose of this thesis work is the synthesis and characterization of various metal-organic frameworks with open metal sites with a view to a possible application in the field of water harvesting.

We chose to focus on MOFs featuring open metal sites because of their common hydrophilicity [44] and because of the intention to make use of XAS and XPS experiments through which, in the presence of open metal sites, it is possible to observe the local geometric and/or electronic structural modifications of the metal ions interacting directly with water molecules during the whole process of water adsorption at those mentioned exposed metal sites.

In particular, we studied water-stable MOFs in order to better understand the phenomena that occur during metal-water interaction in such compounds that exhibit both water stability and OMS.

We chose to synthesize Co and Mn of the series of MOF-74 (also known as CPO-27) and (Fe)-MIL-100. Co and Mn MOF-74 are known for their water stability and gas storage capacity as well as (Fe)-MIL-100 [12] and that makes them good candidates for the developing of a water harvesting device. Out of the series of MOF-74 we focused on Mn because it is one of the least studied until now and on Co because, according to previous literature, it shows great gas-adsorption properties [45], [46]. Moreover, Co and Mn can be analysed with XAS and XPS experiments, hence allowing to study the influence of the metal in such systems. On the other hand, (Fe)-MIL-100 is interesting because of its low toxicity and high cycling stability [12].

Chapter 4

Synthesis and PXRD&IR characterization of target MOFs

4.1 Co and Mn MOF-74

MOF-74 series have general formula M_2dobdc where *dobdc* stands for the deprotonated form of the 2,5-Dihydroxyterephthalic acid of formula $(HO)_2C_6H_2-1,4-(CO_2H)_2$.

The M_2dobdc structure type features one-dimensional metal oxide chains that are connected by *dobdc*⁴⁻ ligands to form a hexagonal array of channels, approximately 11 Å across. Moreover, it shows an infinite chain of square pyramidal metal cations that have an open coordination site directed into the channel [45] (fig. 4.1).

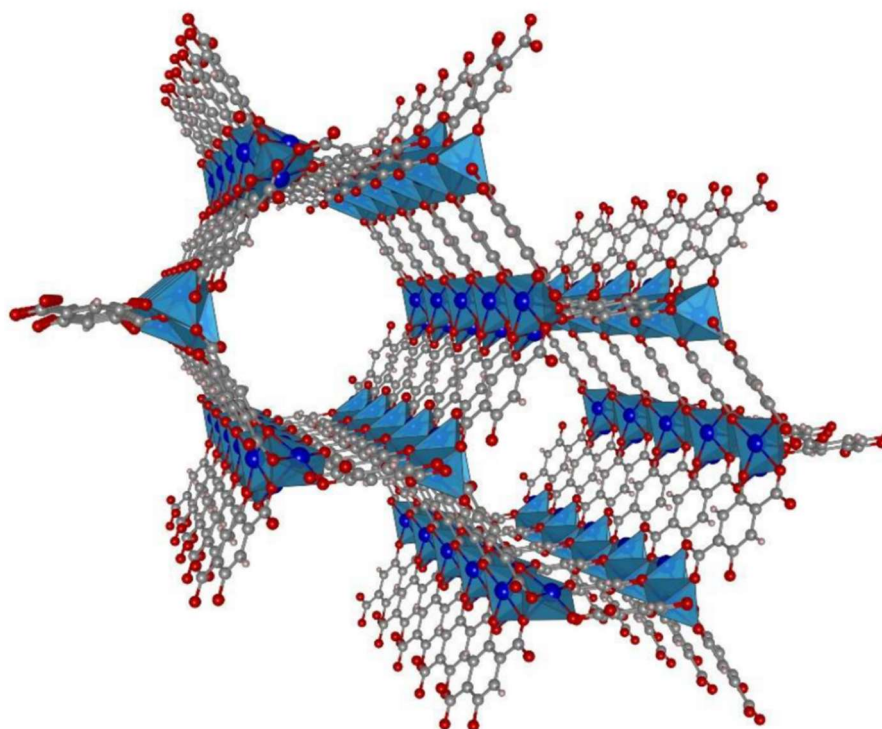


Fig. 4.1: Crystal structure representation of MOF-74 (M—blue, C—grey, O—red); view along the crystallographic *c* axis. The structure is shown for the solvent-free state: the metal centers are penta-coordinated (blue pyramids) with one open site directed into the channel [47].

According to M. H. Rosnes *et al* [48], (Mn)-MOF-74, synthesized as reported in the literature [49], started to decompose at 520 K and at 700 K was fully decomposed, while (Co)-MOF-74, synthesized as reported in [50], started at 680 K and ended at 800 K. TGA (thermogravimetric analysis) analyses in the same study showed loss of non-coordinated water between 293 and 350 K and loss of coordinated water between 350 and 390 K for (Mn)-MOF-74 and loss of water from 300 and 500 K for (Co)-MOF-74.

4.1.1 First synthesis of (Mn) and (Co)-MOF-74

For the synthesis of the first (Mn)-MOF74-1 the procedures reported in literature were followed with little variations [46], [51]. For a typical synthesis $\text{MnCl}_2 \cdot 4\text{H}_2\text{O}$ (220.3 mg, 1.113 mmol, 3.3 equiv) and 2,5-dihydroxyterephthalic acid (66.3 mg, 0.335 mmol, 1 equiv) are dissolved in a 15:1:1 (v/v/v) mixture of DMF-ethanol-water (30 mL) in a 50 mL screw cap jar. The reaction jar is capped tightly and heated in an oven at 125°C for 3 days. The sample is then removed from the oven and allowed to cool to RT. The product was partly stored immediately without washing and partly washed with methanol several times and then stored, in order to analyze both the washed and as synthesized compounds.

For the first (Co)-MOF-74-1 the synthesis procedure follows the one reported in literature[52] with little variations. For a typical synthesis 70.8 mg of 2,5-dihydroxyterephthalic acid (dobdc) and 214.8 mg of $\text{Co}(\text{NO}_3)_2 \cdot 6\text{H}_2\text{O}$ are dissolved in a 50 mL jar in 10 mL of dimethylformamide(DMF), 10 mL of ethanol and 10 mL of water. The jar is capped tightly and placed in oven at 125°C for 3 days. The sample is then removed from the oven and allowed to cool to RT. It is partly stored immediately without washing and partly washed several times with methanol and then stored, in order to analyze both the washed and as synthesized compounds.

4.1.2 IR characterization of synthesized (Mn) and (Co)-MOF-74-1

The (Mn) and (Co)-MOF-74-1 samples were analyzed with IR spectroscopy (ATR-FTIR, instrument details in the experimental section) both as synthesized (labelled as “AS”) and after washing procedures (labelled as “EXEX”). Figures 4.2 and 4.3 show the IR spectra of (Mn) and (Co)-MOF-74-1 respectively.

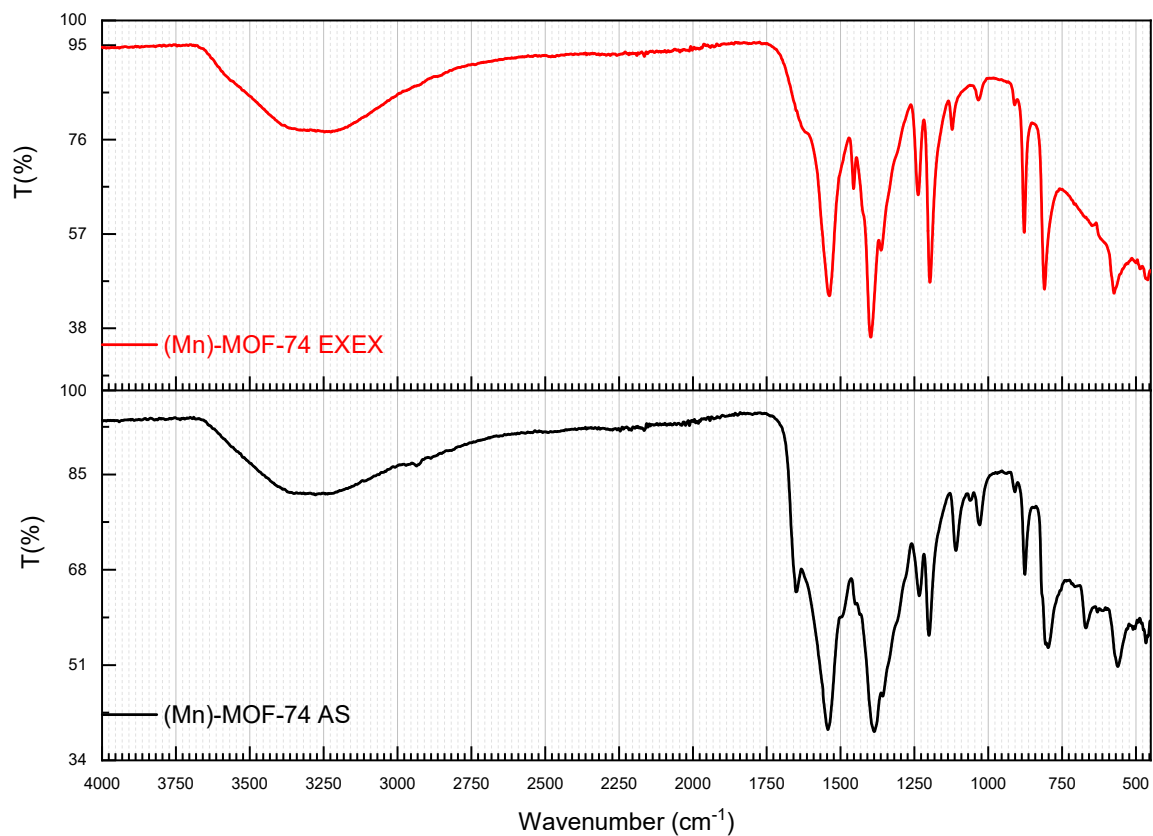


Fig. 4.2: ATR-FTIR spectra of (Mn)-MOF-74-1 (AS---black, EXEX---red)

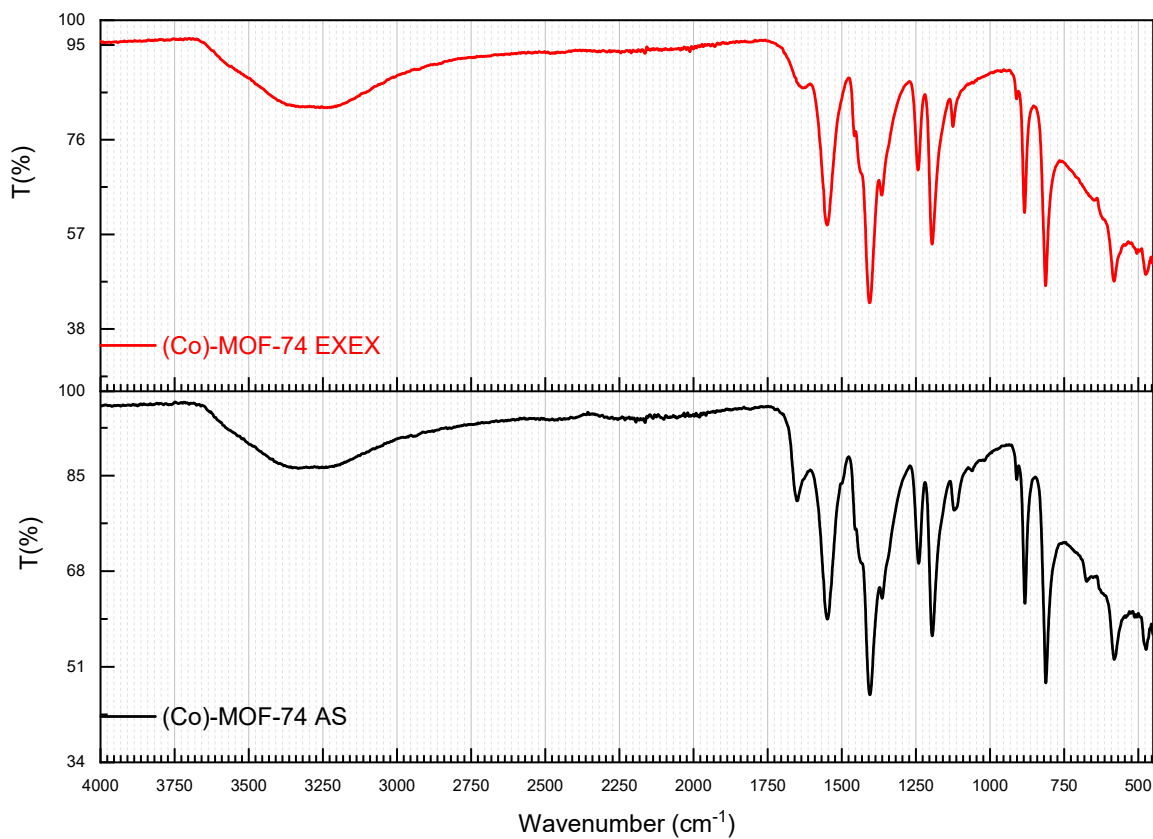


Fig. 4.3: ATR-FTIR spectra of (Co)-MOF-74-1 (AS---black, EXEX---red)

For both Co and Mn MOFs, the washed (EXEX) spectra showed a decreased intensity for the peak at $\sim 1650\text{ cm}^{-1}$ due to the carbonyl of DMF, and the disappearance of the peak at $\sim 670\text{ cm}^{-1}$ due to the stretching of C-N bonds of DMF, sign that the methanol washing has been effective in removing a major part of DMF from the pores. Probably the little peaks remaining are due to DMF strongly chemisorbed on the open metal sites (IR spectra of DMF and dobdc ligand are reported in the experimental section).

4.1.3 Investigation of Mn and Co-MOF-74-1 samples stability to air

The as-synthesized (AS) (Mn)-MOF-74-1 and (Co)-MOF-74-1 series were analyzed with X-ray powder diffraction (PXRD) to confirm the success of the synthetic procedures and, also, after being washed with methanol one time (EX) and two times (EXEX) to monitor the cleaning process. Moreover, to check the stability to air of such compounds, both the AS and EX/EXEX samples were stored uncapped and analyzed at PXRD several times for 2 months, approximately once a week. Figures 4.4 and 4.5 show the trend of PXRD patterns of the as synthesized (AS) (Mn)-MOF-74-1 and of the washed series (EX/EXEX) (Mn)-MOF-74-1, while figures 4.6 and 4.7 show the PXRD pattern of the (AS) (Co)-MOF-74-1 and (EX/EXEX) (Co)-MOF-74-1 respectively.

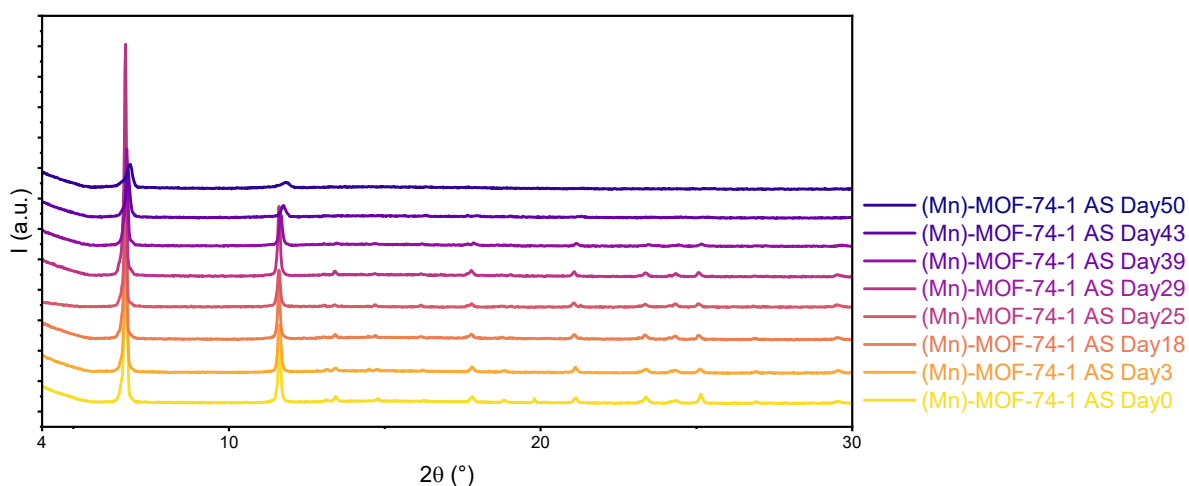


Fig. 4.4: PXRD patterns of the As Synthesized (Mn)-MOF-74-1: time flows from bottom to top. From the 5th pattern from bottom (Day 29) the sample was kept uncapped in contact with air and immediately started to decompose, suggesting instability to air.

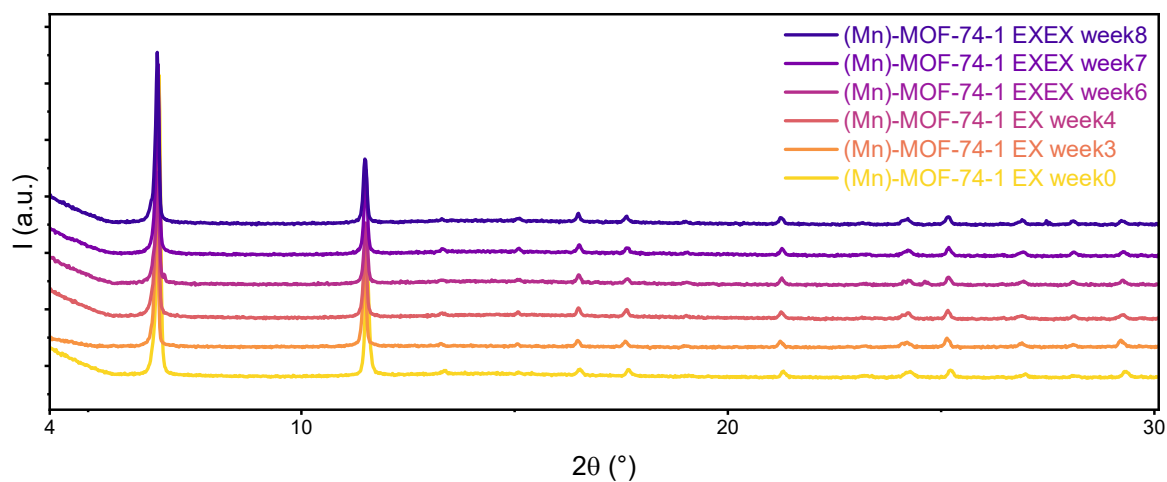


Fig. 4.5: PXRD patterns of the (Mn)-MOF-74-1 exchanged with methanol and stored uncapped: time flows from bottom to top. From the sixth week the sample was washed a second time with methanol (EXEX) in order to complete the washing. The exchanged (Mn)-MOF-74-1 showed great stability towards air and time.

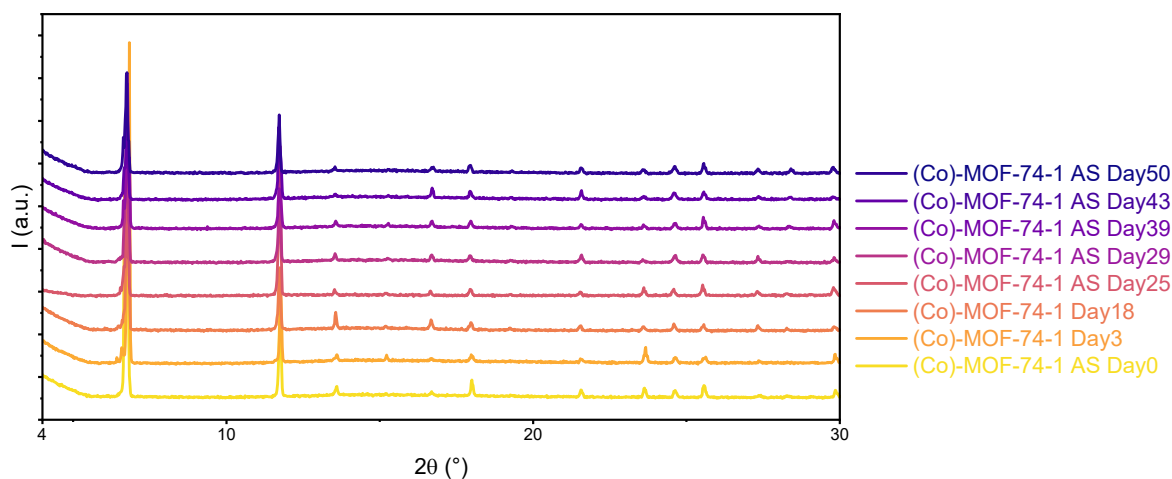


Fig. 4.6: PXRD patterns of the As Synthesized (Co)-MOF-74-1: time flows from bottom to top with the black pattern recorded the day of synthesis. The AS (Co)-MOF-74-1 showed great stability towards air and time.

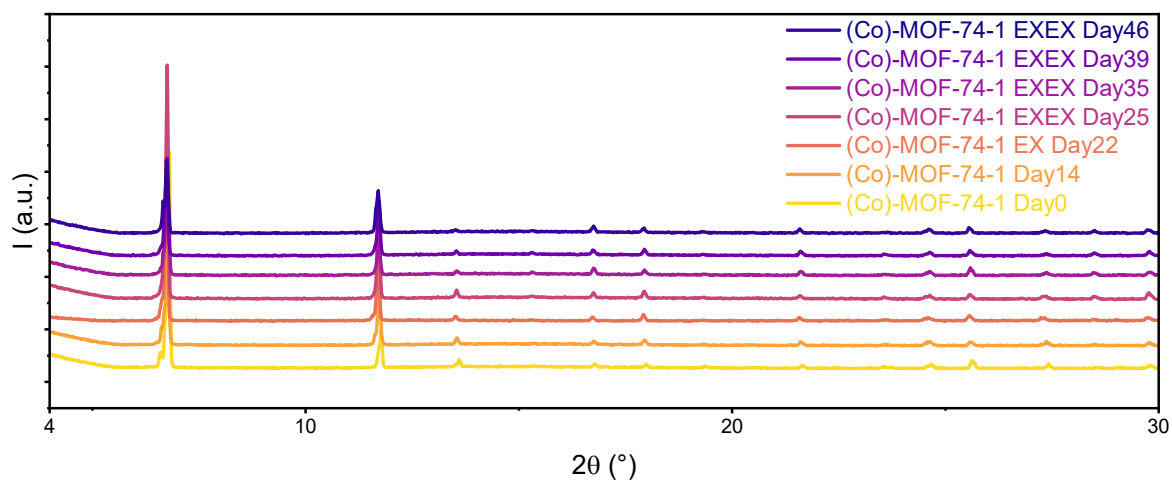


Fig. 4.7: PXRD patterns of the (Co)-MOF-74-1 Exchanged with methanol: time flows from bottom to top. From the fourth pattern the sample was washed a second time with methanol (EXEX) in order to complete the washing. The exchanged (Co)-MOF-74-1 showed great stability towards air and time.

Exchanged (Mn)-MOF-74-1 and (Co)-MOF-74-1 resulted being stable to air and time as well as the AS (Co)-MOF-74-1. Interestingly, the AS (Mn)-MOF-74-1 started to decompose when left uncapped in contact with air. To confirm this trend in the AS (Mn)-MOF-74 behaviour towards air, another experiment has been conducted synthesizing new (second) (Mn)-MOF-74-2 sample and monitoring the new AS sample through time.

With these results confirming the stability of washed samples, we proceeded to synthesize a new batch of Co and Mn MOF-74.

4.1.4 Synthesis of a new batch of (Mn) and (Co)-MOF-74

The synthesis of new (Mn)-MOF-74-2 has been conducted in four 250 mL vials following the procedure of references [46], [51]. Into each vial were added ~0.3825 g of dobdc dissolved in 152 mL of DMF and a solution of ~1.2675 g of $\text{MnCl}_2 \cdot 4\text{H}_2\text{O}$ dissolved in 10 mL EtOH + 10 mL H_2O . The reaction jars were capped tightly and heated in an oven at 135°C for 24 hours (time and temperature exact as in the referenced literature, hence slightly different from the previous batch of (Mn)-MOF-74-1 that used 125°C for 3 days). Once cooled to RT the jars were filtered on vacuum on a septum with filter paper and washed with MeOH. Part of the AS MOF was stored capped separately for few days, analyzed at PXRD then left stored uncapped to see if it degrades when exposed to air. The remaining product was first washed with methanol (MeOH) than washed with ethanol (EtOH), hence part of the sample was washed also with deionized water (H_2O) to check water stability.

For the new (Co)-MOF-74-2 the reaction has been conducted in four 250 mL vials following directions from [52]. Into each vial were added ~0.9675 g of $\text{Co}(\text{NO}_3)_2 \cdot 6\text{H}_2\text{O}$ dissolved in 45+45 mL of H_2O + EtOH and a solution of ~0.3175 g of dobdc dissolved in 45 mL DMF. The reaction jars were capped tightly and heated in an oven at 125°C for 72 hours, as exactly for the previous batch (hence slightly different from the cited literature). A little part of the product was stored as synthesized and the remaining was washed several times with methanol. Hence, part of the washed sample was sunk in deionized water to check water stability.

4.1.4 IR characterization of synthesized (Mn) and (Co)-MOF-74-2

The AS synthesized (Mn)-MOF-74-2 showed many additional signals in the IR spectrum: two DMF peaks are present (~1650 cm^{-1} carbonyl stretching and ~670 cm^{-1} C-N stretching) and a broad detailed band between ~3200 and ~2700 cm^{-1} due to the stretching of acid O-H of unreacted dobdc ligand which overlap with the water/phenol O-H stretching broad band

between ~ 3600 and ~ 3200 cm^{-1} (fig. 4.8-D). After washing with MeOH and EtOH the DMF peaks disappeared as well as the broad band between ~ 3200 and ~ 2700 cm^{-1} of the unreacted dobdc (fig. 4.8-C and B). However, the cleaning was not fully effective because the PXRD patterns of the samples washed with methanol and ethanol showed many peaks belonging to additional phases a part of the one of MOF-74, as illustrated in the following section.

We also soaked part of the washed (Mn)-MOF-74-2 in deionized water and collected an IR spectrum to check for water stability: no significant changes were observed in the new IR suggesting that the (Mn)-MOF-74 is stable in liquid water (fig. 4.8-A).

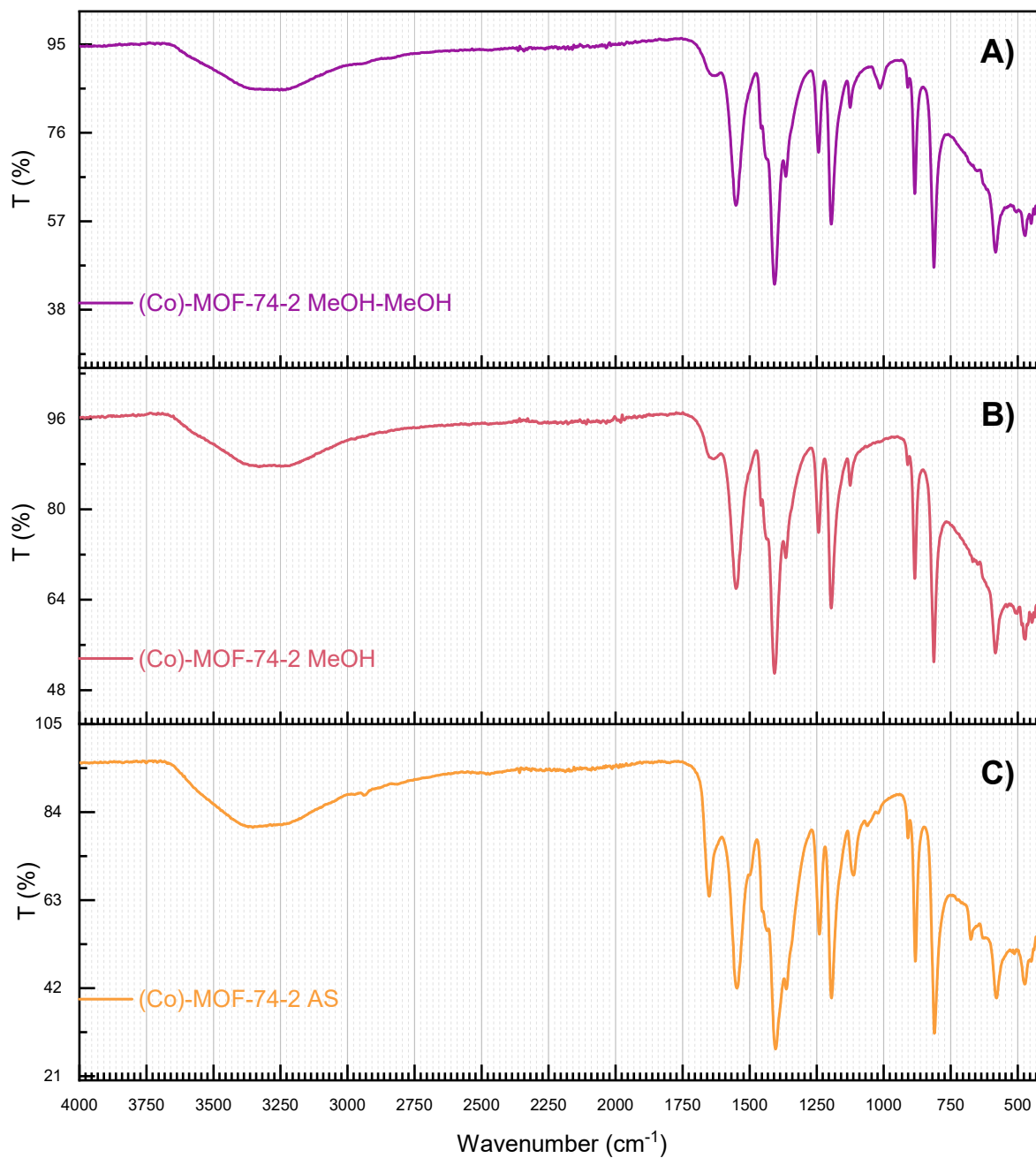


Fig. 4.9: IR spectra of (Co)-MOF-74-2

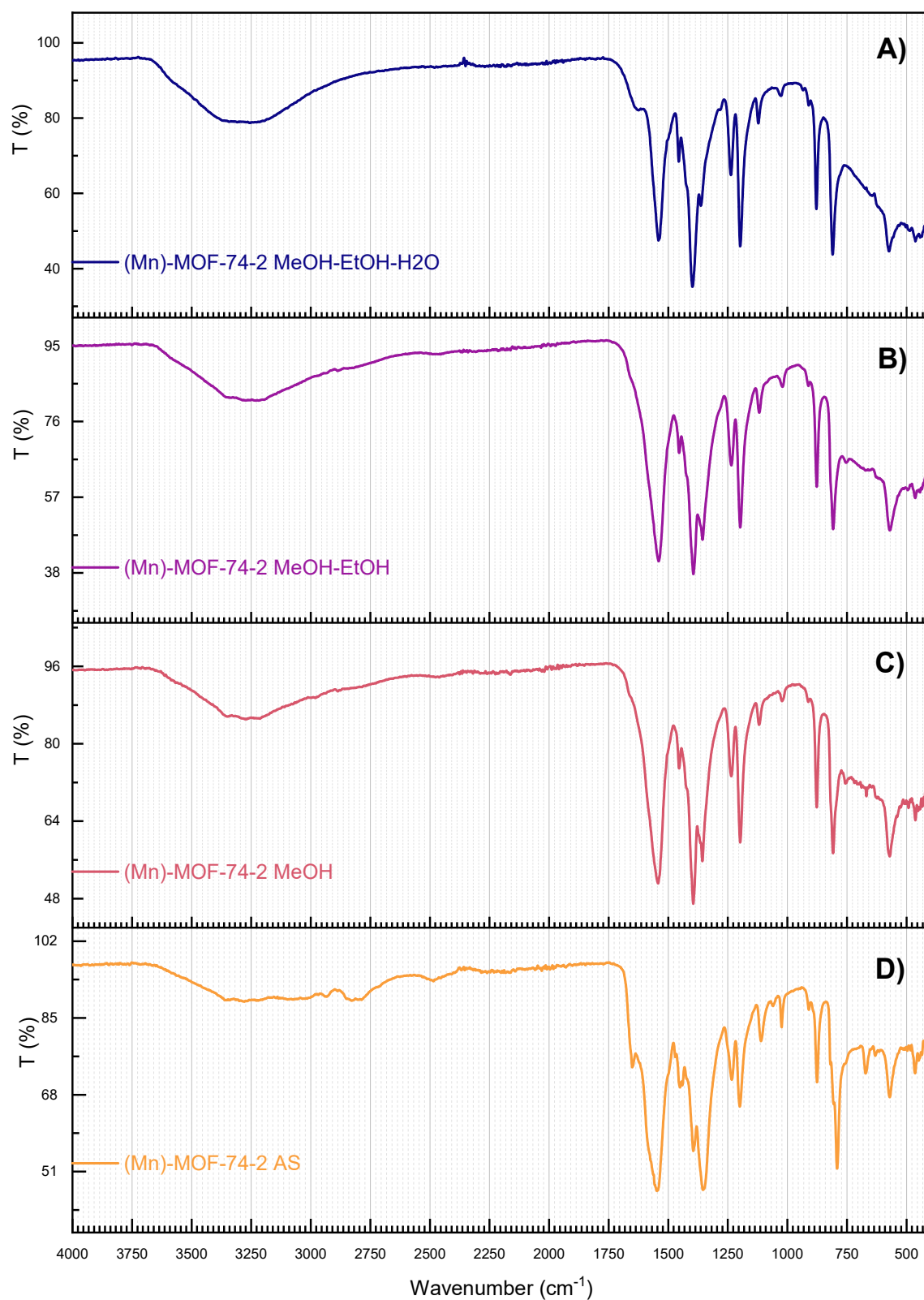


Fig. 4.8: IR spectra of (Mn)-MOF-74-2

For (Co)-MOF-74-2, the MeOH-washed spectra showed a decreased intensity for the DMF's peaks at $\sim 1650\text{ cm}^{-1}$ and $\sim 670\text{ cm}^{-1}$ as compared to the AS one (fig. 4.9 A,B and C), suggesting that the methanol washing has been effective in removing a major part of DMF from the pores. Probably the little peaks remaining are due to DMF strongly chemisorbed on the open metal sites (IR spectra of DMF and dobdc ligand are reported in the experimental section).

4.1.5 Checking air instability of “as synthesized” (Mn)-MOF-74-2

The as synthesized (AS) (Mn)-MOF-74-2 (second batch) was analyzed with PXRD through time to double-check the instability to air observed for the previous batch of as synthesized (Mn)-MOF-74-1. The new PXRD patterns confirmed the trend: after almost two months (56 days) of exposure to air the AS sample's PXRD pattern showed great loss of crystallinity (fig. 4.10).

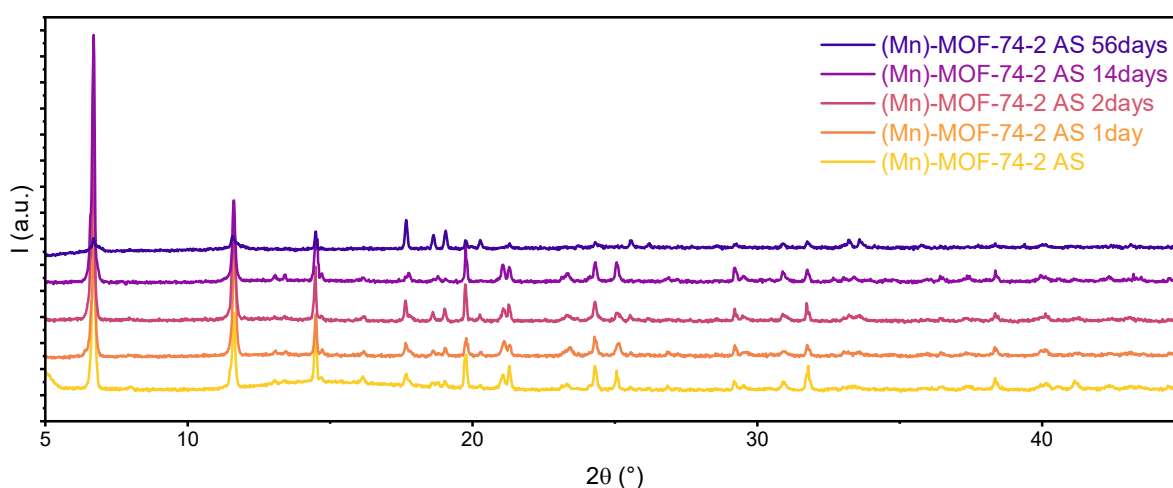


Fig. 4.10: PXRD pattern of the as synthesized (AS) (Mn)-MOF-74-2 (second batch). Time flows from bottom (yellow pattern just left to air) to top (blue pattern, 56 days of air exposure). In the last pattern the main peaks of the MOF-74 at ~ 6.5 and ~ 11.5 2θ are almost disappeared.

The as synthesized compound is not pure: each pattern was analyzed with Le Bail procedure and showed some little peaks not attributable to (Mn)-MOF-74, sign that more than one phase is present in the sample. (fig. 4.11 shows the Le Bail fitting of (Mn)-MOF-74-2 AS). Since the washed sample is stable to air, we hypothesize that the impurities may induce or accelerate the degradation mechanism of the MOF.

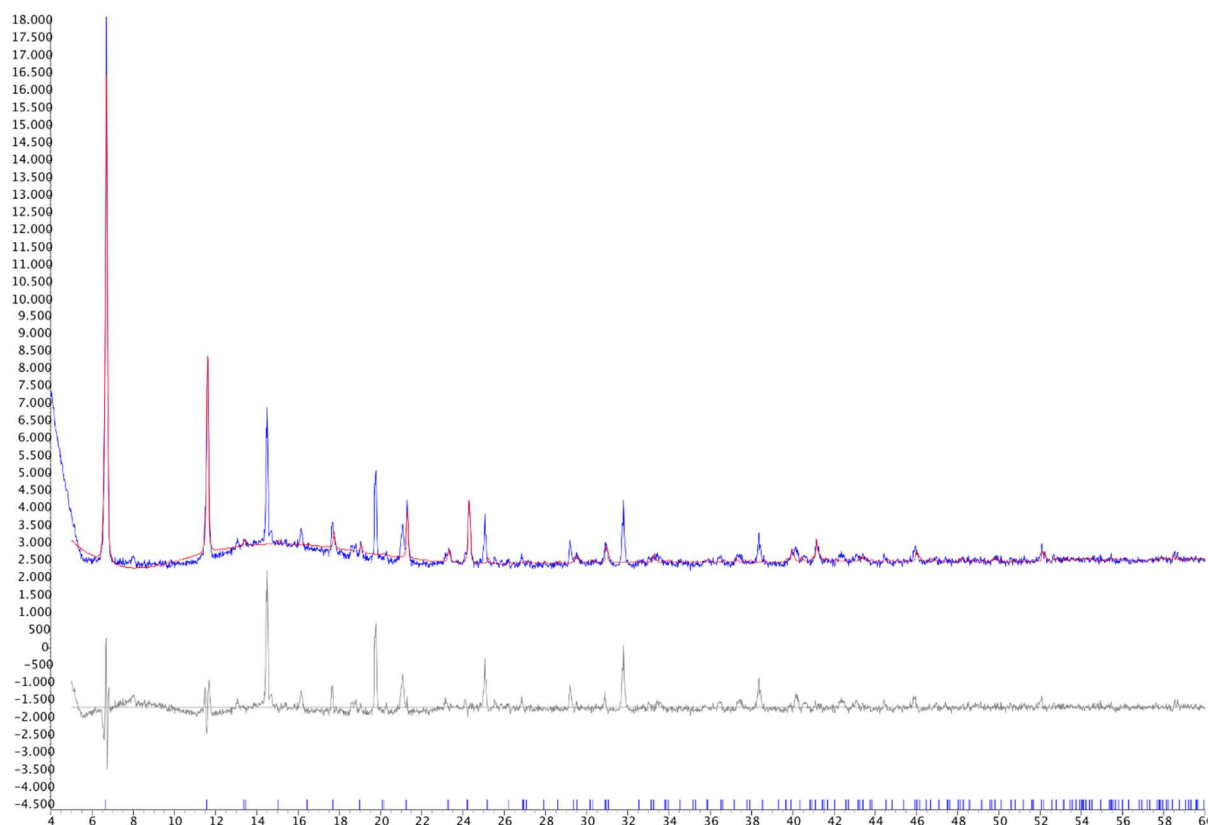


Fig. 4.11: Le Bail fitting of (Mn)-MOF-74-2 AS pattern. (Blue—calculated pattern, red—experimental pattern, grey—difference between calculated and experimental patterns). The red pattern was calculated with parameters

Rwp	Space group	Volume/Å ³	a / Å	b / Å	c / Å	α / °	β / °	γ / °
7.01	R-3	4179.576	26.502	26.502	6.871	90	90	120

4.1.6 PXRD characterization of washed & activated (Mn)-MOF-74-2

The cleaning procedure consists of several washing steps in MeOH and EtOH. Although this procedure has been proven effective for other materials, in the case of (Mn)-MOF-74-2 PXRD pattern still showed peaks of impurities (fig. 4.13).

Hence, a small amount of the sample was sunk in deionized water to check water stability and we observed that not only (Mn)-MOF-74 is stable to water but also that it has washed completely, and that the crystallinity has improved (fig 4.13): the Le Bail of the water washed sample showed no more unindexed peaks (fig. 4.12).

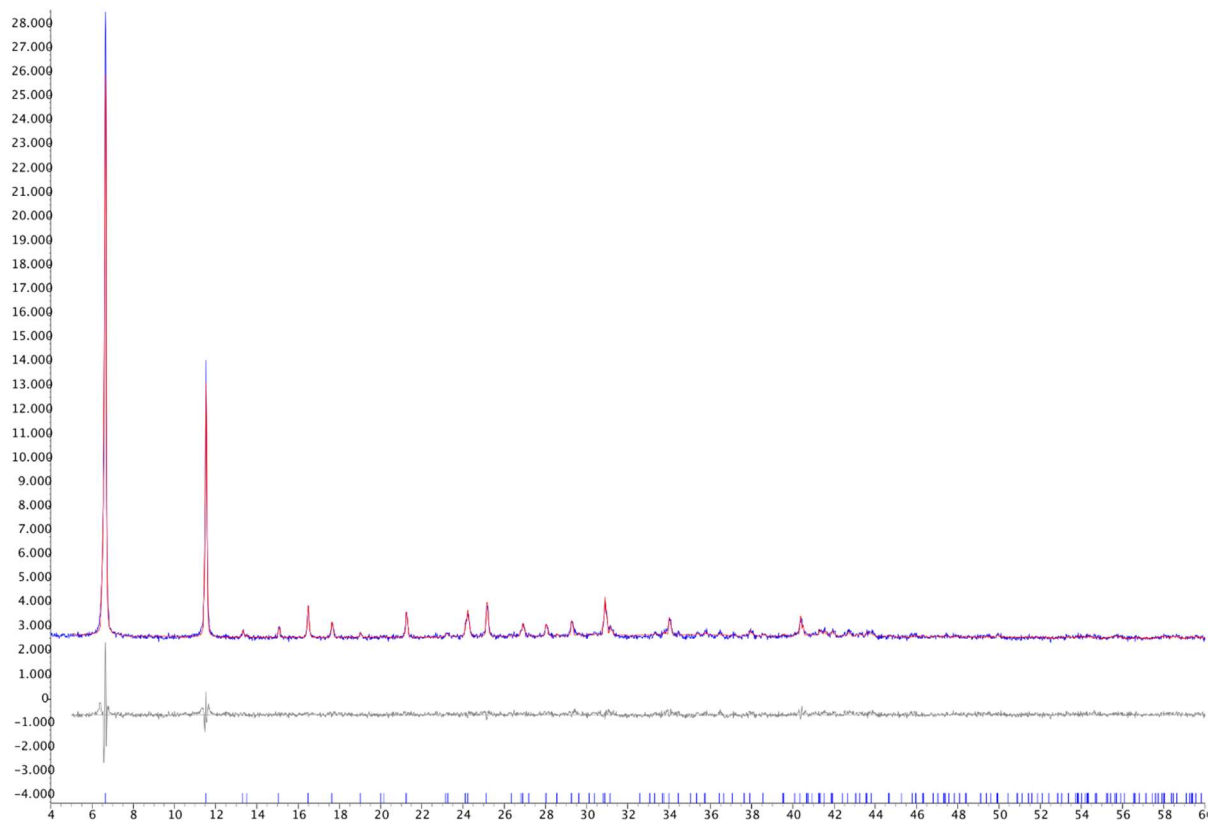


Fig. 4.12: Le Bail of (Mn)-MOF-74-2 washed with MeOH, EtOH and sunk in deionized water. All peaks are well fitted by the Le Bail calculation suggesting purity of the sample. (red---calculated pattern, blue---experimental pattern, grey---difference between calculated and experimental patterns).

Rwp	Space group	Volume/Å ³	a / Å	b / Å	c / Å	α / °	β / °	γ / °
2.82	R-3	4188.246	26.593	26.593	6.838	90	90	120

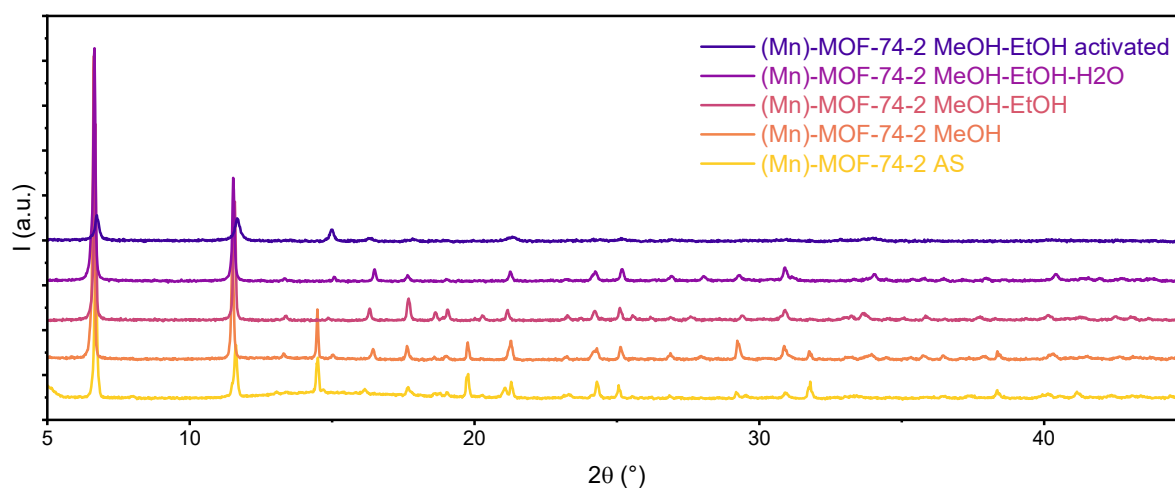


Fig. 4.13: PXRD patterns of (Mn)-MOF-74-2 during the stages of washing: as synthesized (AS), washed with MeOH, washed with MeOH than with EtOH and washed with MeOH, EtOH than sunk in deionized water. The last pattern (blue, at the top) has been recorded after activation of the sample washed with MeOH and EtOH: it shows great loss of crystallinity.

The (Mn)-MOF-74 sample washed with MeOH and EtOH was subsequently activated under vacuum to remove any DMF left in the pores by heating at 170°C. However, after 1 hour of heating the color of the sample shifted into a darker brown, so the temperature was lowered to 120°C for one night. PXRD pattern of the activated sample (labelled as “MeOH-EtOH activated”) showed great loss of crystallinity: the peaks lowered and broadened significantly (fig. 4.13), suggesting instability to high temperature.

4.1.7 Water induced re-crystallization of activated (Mn)-MOF-74-2

Since the PXRD pattern of the activated (Mn)-MOF-74-2 washed with MeOH-EtOH showed loss of crystallinity, a small amount of the activated sample was washed in deionized water aiming to restore crystallinity and then re-activated. However, the PXRD pattern showed complete degradation after the re-activation (fig. 4.14).

We wondered if only washing in water without re-activating the sample would restore the crystallinity, hence we made three tests:

- **H₂O drop:** we put a pinch of the MeOH-EtOH activated powder sample on a petri glass and dropped on it two drops of deionized water then left it to air dry. Hence, we collected an PXRD pattern of this “H₂O drop” sample to check if water itself, without even washing away impurities, is enough to restore crystallinity. It is: crystallinity has improved (fig. 4.14). However, the sample was not completely pure: according to Le Bail analysis of the pattern some peaks are not attributable to (Mn)-MOF74
- **H₂O decanted:** a small amount of the activated sample was washed with deionized water and the waste waters were decanted. The powder was then collected and analyzed at PXRD. Crystallinity improved (fig. 4.14) and phase is pure: Le Bail analysis fitted all the peaks well.
- **H₂O filtered:** a small amount of the activated sample was washed with deionized water and the waste waters were filtered. The powder was then collected and analyzed at PXRD. Crystallinity improved even more than the one sample of which waste waters were decanted (fig. 4.14). The phase is pure: Le Bail analysis fitted all the peaks well.

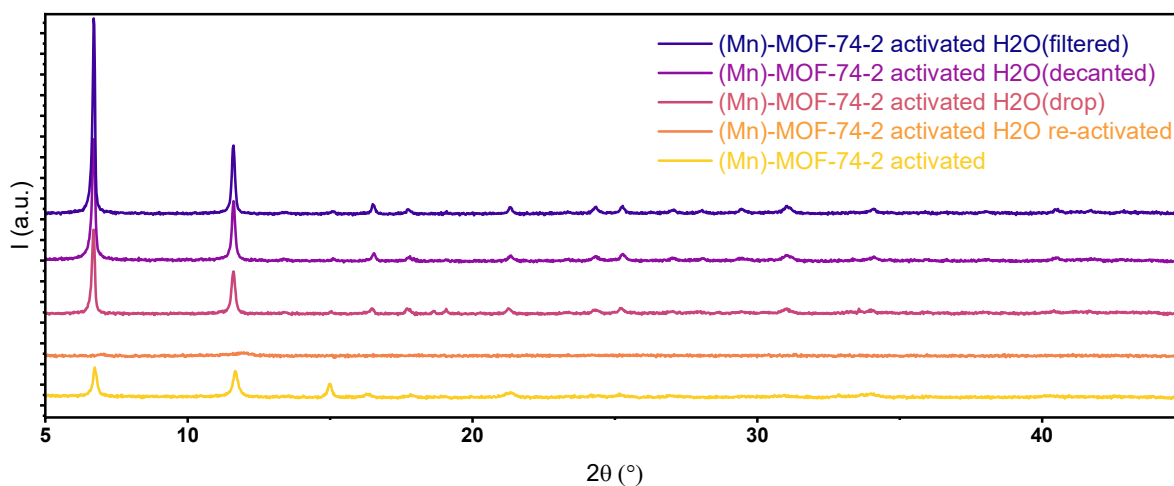


Fig. 4.14: PXRD patterns of (Mn)-MOF-74-2 activated (yellow), washed with water and re-activated (orange), hydrated with water drops (magenta), washed with water and decanted (purple), washed with water and filtered (blue).

Given that interesting behavior of re-crystallization after water baths we hypothesize that the MOF may collapse when its pores got vacuumed and re-organizes while sunk in water, helped by solvation and water molecules filling the pores.

4.1.8 PXRD characterization of synthesized (Co)-MOF-74-2

Unlike (Mn)-MOF-74-2, the cobalt analogue resulted almost pure immediately when synthesized. Le Bail fitting of the as synthesized (AS) PXRD(Co)-MOF-74-2 PXRD pattern has confirmed phase purity of the sample. (fig. 4.15). The sample has been washed anyway with methanol two times in order to exchange DMF inside the pores. Later, it has been activated under vacuum at 170°C for 1 hour then lowered at 120°C overnight due to a color shift to a slightly darker brown. After the activation procedure the crystallinity worsened a little, as illustrated by PXRD patterns in fig. 4.16, maintaining, in any case, a quite good crystallinity, much better if compared to the manganese one which resulted almost amorphous after activation (fig. 4.17).

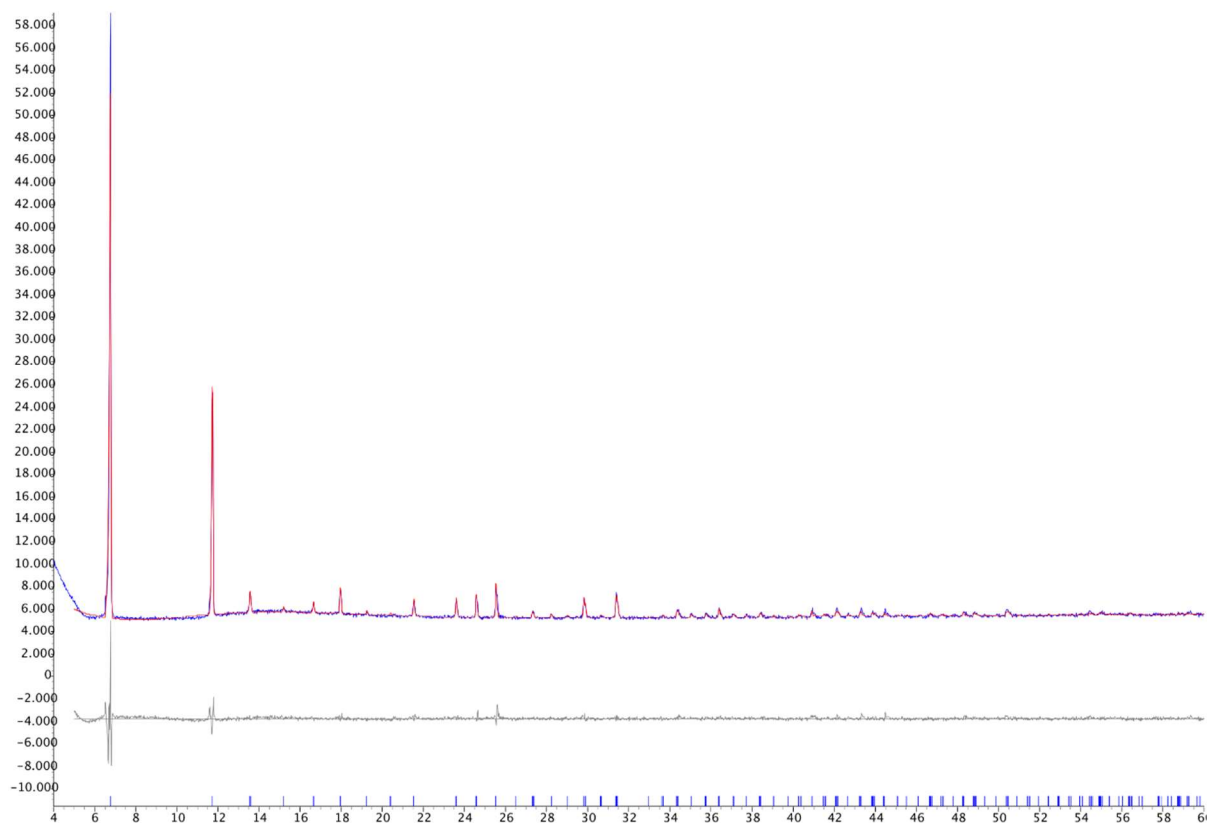


Fig. 4.15: Le Bail of as synthesized (AS) (Co)-MOF-74-2, all peaks are well fitted (red---calculated pattern, blue---experimental pattern, grey---difference between calculated and experimental pattern).

Rwp	Space group	Volume/Å ³	a / Å	b / Å	c / Å	α / °	β / °	γ / °
3.05	R-3	4012.242	26.109	26.109	6.796	90	90	120

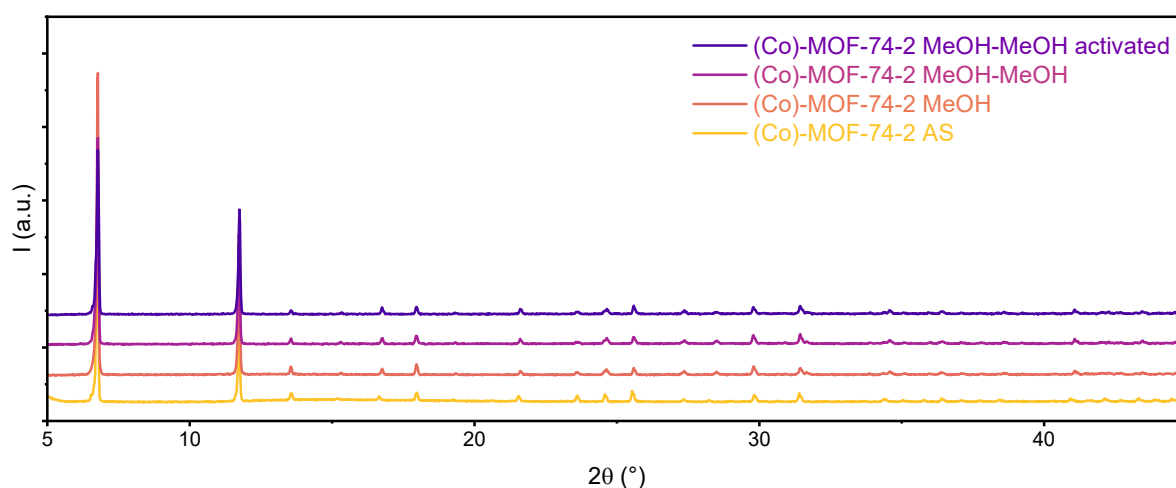


Fig. 4.16: PXRDs of (Co)-MOF-74-2 (second batch). As synthesized (AS), washed with methanol one time (MeOH) and two times (MeOH-MeOH) and after activation (MeOH-MeOH activated). The AS patterns and washed ones are very similar in crystallinity, the activated one instead shows lower peaks. All the patterns have been analyzed with Le Bail method to confirm pureness of the phase (Le Bail analyses are reported in the experimental section).

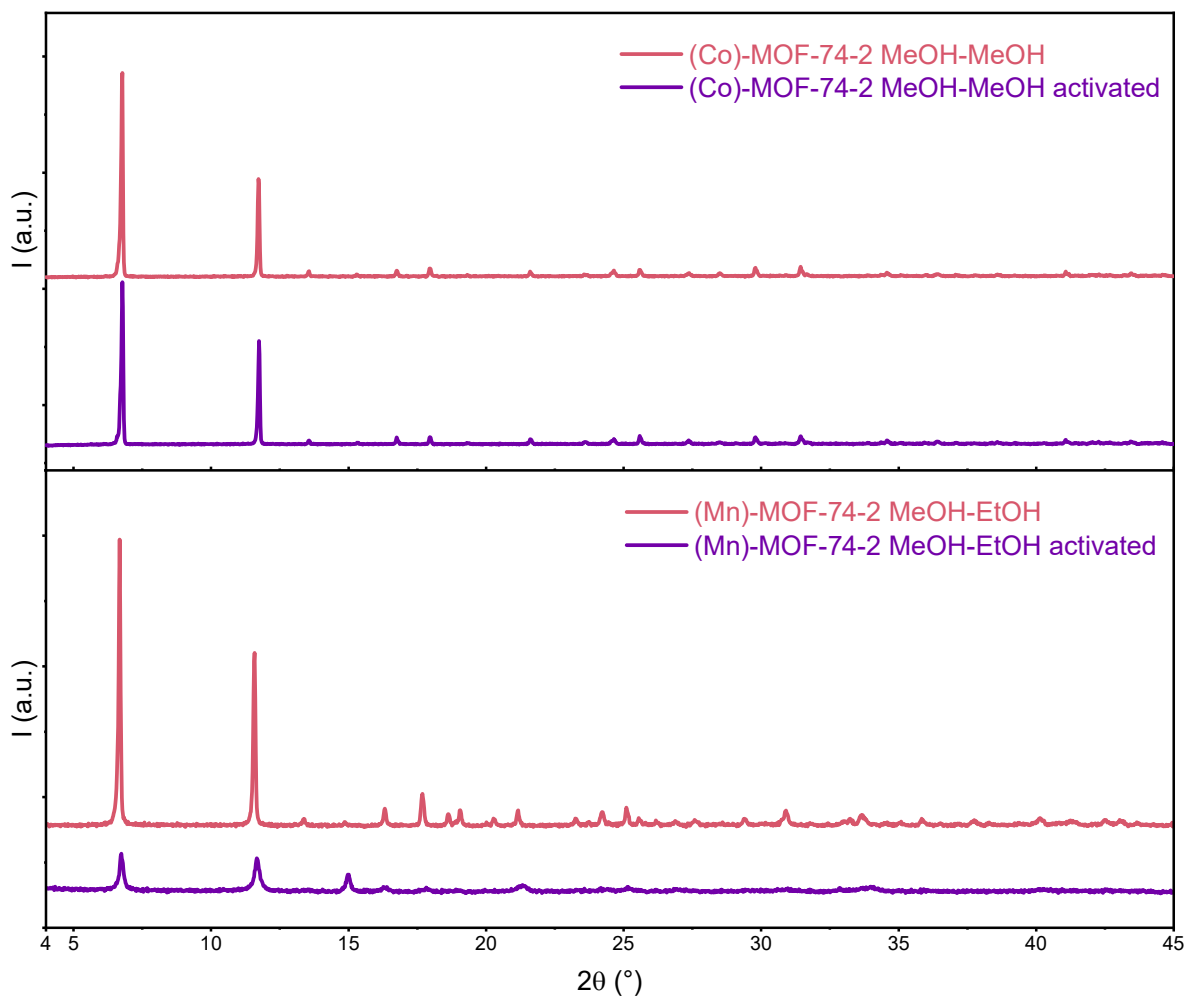


Fig. 4.17: Comparison between (Mn)-MOF-74- 2 (bottom) and (Co)-MOF-74-2 (top) loss of crystallinity after activation. The manganese sample worsened much more than the cobalt one.

4.2 Fe MIL-100

Fe MIL-100 is a Fe(III) based MOF which features a large pore structure [53]. Its SBU (second building unit) contains three Fe(III) ions in octahedral coordination sharing one vertex (the single O atom). The equatorial positions are occupied by the O atoms of the ligands BTC (Trimesic acid, $C_6H_3(CO_2H)_3$, fig. 4.19). The apical position of one of the three octahedra coordinates an anion which can vary depending on the synthetic route (F^- or OH^-) while the last two apical positions present two adsorbed water molecules (fig. 4.18). The MOF in the fully activated form, has chemical formula $Fe_3O_2(BTC)_2$ with three open metal sites, while the hydrated formula, with water coordinated to the OMS, is $Fe_3O(H_2O)_2(X)(BTC)_2$ [54].

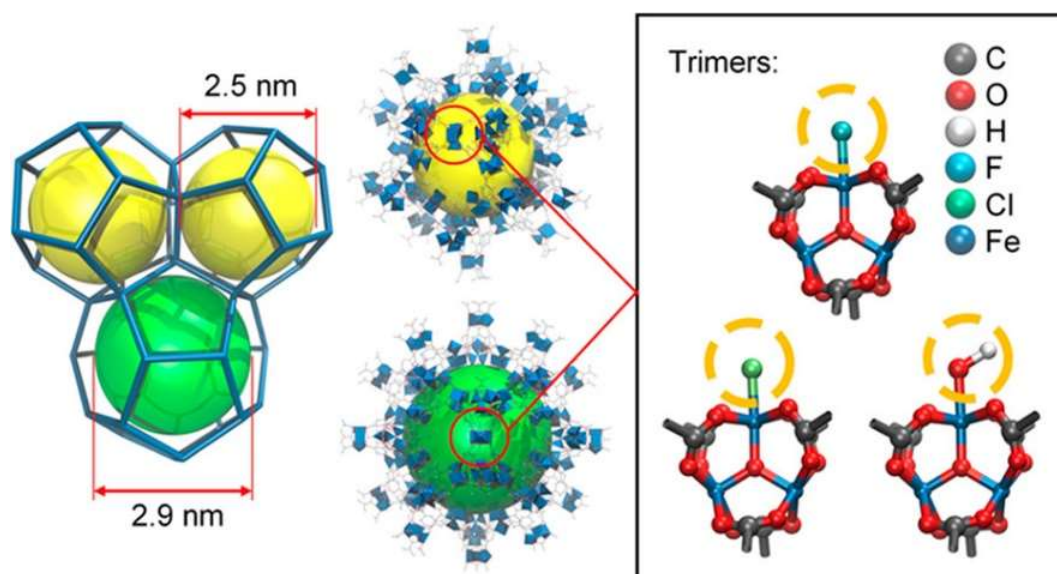


Fig. 4.18: Structure of (Fe)-MIL-100. On the right, in the frame, is shown the Fe(III) SBU with different anions possibilities and two open metal sites per SBU, in the centre the small cage (yellow) and large cage (green), on the left how the small and large cages combine in the MOF into a MTN topology [54].

The structure of (Fe)-MIL-100 is characterized by four SBUs connected by other BTC ligands forming a supertetrahedron. (fig 4.19). More supertetrahedra combine themselves in a MTN topology that shows 2 different mesoporous cages (fig. 4.18 and 4.19). The larger one is 29 Å (2.9 nm) across and shows pentagonal and hexagonal windows of 5.5 Å and 8.6 Å across, while the small cage measures 25 Å (2.5 nm) across and shows only pentagonal windows of 5.5 Å diameter.

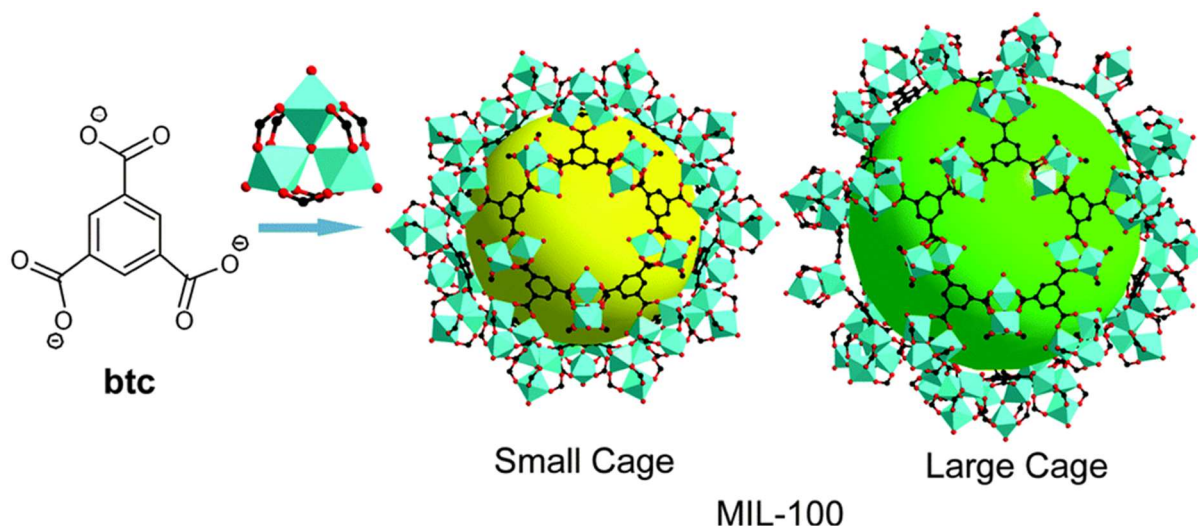


Fig. 4.19: Trimesic acid (btc) and Fe(III) SBU combining into the small and large cage of MIL-100 framework [55].

Thanks to its large surface area (BET surface area is as high as $2300 \text{ m}^2\text{g}^{-1}$), (Fe)-MIL-100 can reach adsorption capacity of 0.75 g of water per gram of MOF at 298 K [12], [53].

4.2.1 Synthesis of the first batch of (Fe)-MIL-100

For (Fe)-MIL-100 we followed the mechanochemical green synthesis developed by B. E. Souza *et al* [25] that makes no use of solvent except for water. In this procedure, ligand and metallic salt powders were ground together, heated in an oven and then washed in water to start a reconstruction process of the framework (fig. 4.20).

More specifically, 245.6 mg of $\text{Fe}(\text{NO}_3)_3 \cdot 9\text{H}_2\text{O}$ [iron(III)nitrate 9-hydrate] and 85.6 mg of H_3BTC [benzene-1,3,5-tricarboxylic acid] were combined in the agate mortar and manually ground for 15 mins. The resulting material was heated in the oven in a screw cap jar at 160°C for 4h to complete the annealing process. Part of the product was stored as synthesized (AS) while the remaining (and major) part of the product was washed by centrifugation with methanol (10 min) and deionized water (10 min) to remove any unreacted components and allowed to dry at RT one night.

Hence, the sample has undergone numerous washes in deionized water at RT in order to enhance its crystallinity. In fact, according to B. E. Souza *et al* [25], the as synthesized (Fe)-MIL-100 presents a defective structure in which the ligand is still protonated and doesn't coordinate directly with the metal centre. Water baths would “reconstruct” the MOF. Acting as a weak base, water would deprotonate the ligand thus allowing the metal and the trimesic acid to link together (fig. 4.20).

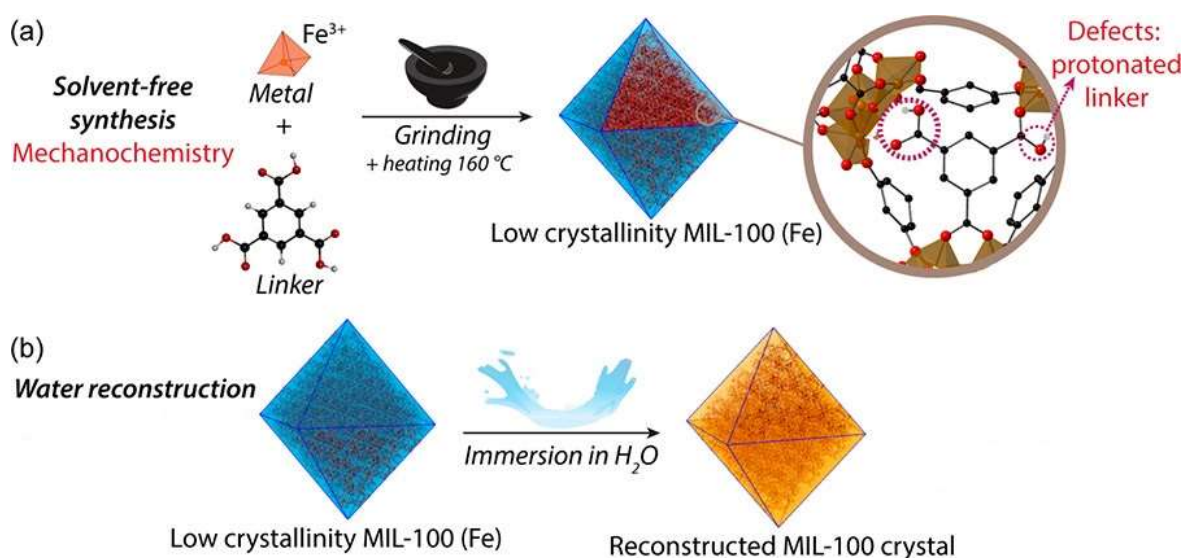


Fig. 4.20: Scheme of mechanochemical synthesis (a) and water reconstruction (b) from[25].

4.2.2 Water reconstruction attempts of the first batch of (Fe)-MIL-100

After the annealing, the sample has been washed several times (always around 1-2 days each) in deionized water under stirring at RT for the reconstruction process. In order to understand which washing procedures allowed a faster increase in crystallinity, different washing times were tried. The first washes (1 to 5) were generally short (few hours in total) and water was changed frequently. For the last washes, instead, the samples were kept in water for longer times (1-3 days). After each wash the sample was centrifugated to allow for the decanting of the supernatant waters, hence it was left to air dry on a watch glass.

We expected to see an improvement of the crystallinity in the PXRD patterns after each wash, as observed by B. E. Souza *et al* [25]. However, our sample only improved a little after the first wash (W1) while the subsequent washes (W2-W9) seemed to have no effect on the sample's crystallinity, if not, even, to make it worsen (fig 4.21).

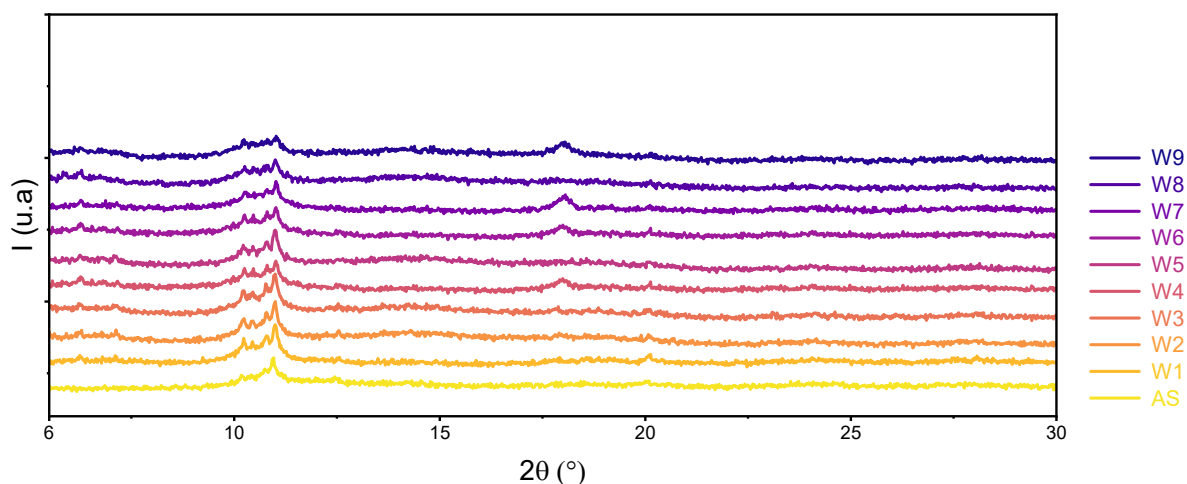


Fig. 4.21: PXRD patterns of the first batch of (Fe)-MIL-100 after subsequential washes in deionized water. Only W1 pattern (washed 1 time) improved compared to the previous as synthesized one (AS). The following washes had no effect in enhancing the crystallinity.

To notice, after the eighth wash (W8) the sample was heated with an air pump at 60°C in order to accelerate the drying process. As a result, the PXRD pattern showed one peak less than the previous pattern (W7).

To investigate whether the sample's crystallinity depends on the temperature, some of the W9 powder was refrigerated at 5°C then analyzed at PXRD: no significant changes were observed suggesting that cold temperatures do not help in restoring the crystallinity (fig 4.22).

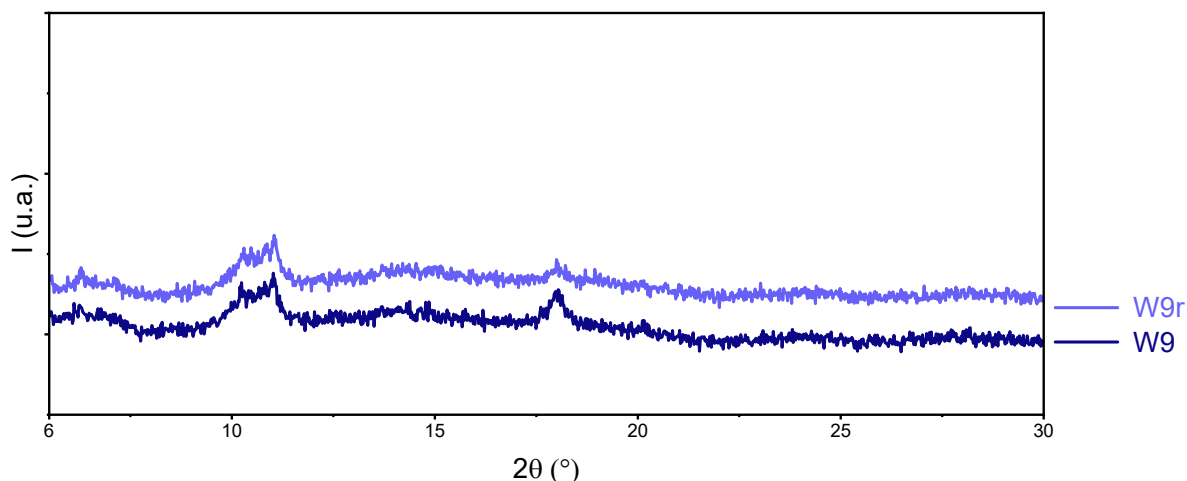


Fig. 4.22: Comparison between PXRD patterns of W9 (washed nine times) and W9r (washed nine times and refrigerated) samples.

4.2.3 Synthesis of a new batch of (Fe)-MIL100

Since the previous batch hadn't recovered in crystallinity, we decided to synthesize a new batch of (Fe)-MIL-100 still following the synthetic procedure [20] but paying closer attention to the washing steps and skipping the methanol washing before the reconstruction process.

More specifically, 4.912 g of $\text{Fe}(\text{NO}_3)_3 \cdot 9\text{H}_2\text{O}$ (iron(III)nitrate 9-hydrate) and 1.712 g of H_3BTC (benzene-1,3,5-tricarboxylic acid) were combined in the agate mortar and manually ground for 15 mins. The resulting material was heated in the oven in a screw cap 50 mL jar at 160°C for 4h to complete the annealing process. Part of the product was stored as synthesized (AS) while the remaining (and major) part of the product has undergone water reconstruction.

4.2.2 Water reconstruction of the new batch of (Fe)-MIL-100

For the new water reconstruction process, we took special care not to centrifuge the sample or heat it during the drying process.

The sample powder was divided into 7 vials of 40 mL each with deionized water under stirring at RT. Each vial was kept under water reconstruction for different times (refreshing the water once a day) then filtered under vacuum pump and let to air dry on a petri glass for few hours (except for the vial W7 that was decanted - after being left to settle overnight - then put in the oven at 36°C overnight to dry) and analyzed at PXRD, in order to record gradually the increase of crystallinity. The table below shows the steps followed.

Name	Time in water	Mass / g	Color
FeMIL100 AS	none	~0.080	Rust orange
FeMIL100 W1	3 h	0.4393	Light orange
FeMIL100 W2	6 h	0.4086	Light orange
FeMIL100 W3	1 day	0.3509	Light orange
FeMIL100 W4	2 days	0.4338	Light pinkish orange
FeMIL100 W5	3 days	0.4193	Light pinkish orange
FeMIL100 W6	4 days	0.4043	Light pinkish orange
FeMIL100 W7	7 days	~0.4988	Light pinkish orange

Gradually the color of the powder shifted into a lighter orange (fig. 4.23).

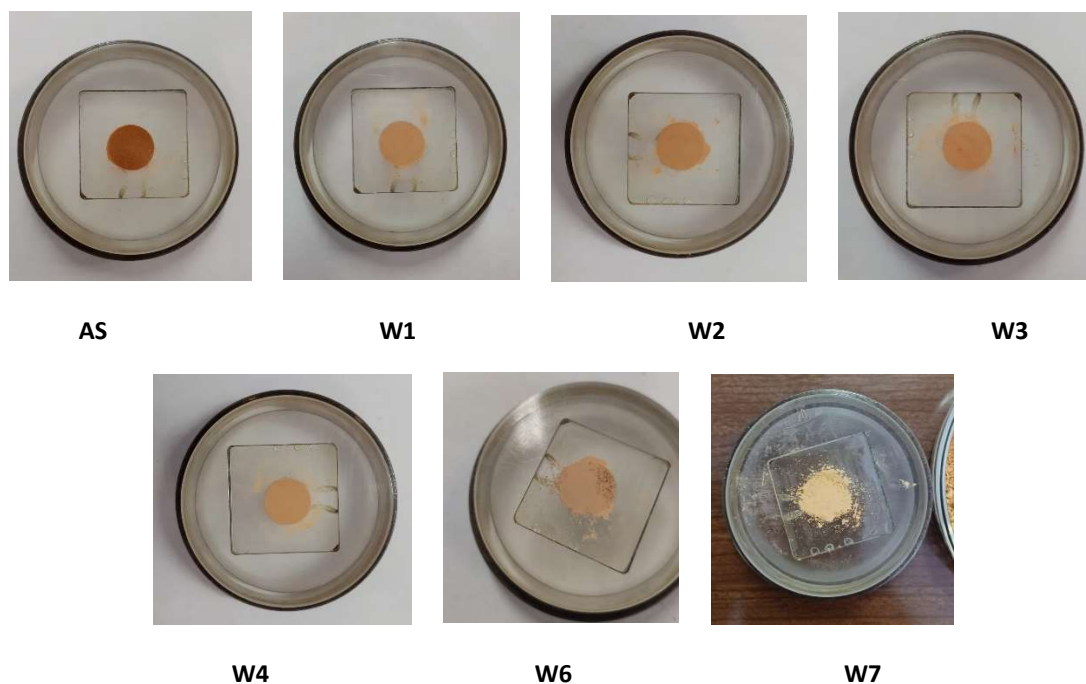


Fig. 4.23: Color shifting of the new batch of (Fe)-MIL-100 after different water washing times

Very interestingly the PXRD patterns of the samples AS and W1 to W6 showed a very slow improvement of crystallinity and slow emergence of the low angle peaks – instead the sample W7 showed a surprisingly faster improvement (fig. 4.24). We hypothesize that the different drying method is the key to higher crystallinity. We also took into account the possibility that with the previous drying methods the samples may not have dried completely. However, further experiments need to be conducted to better understand the actual influence of each parameter.

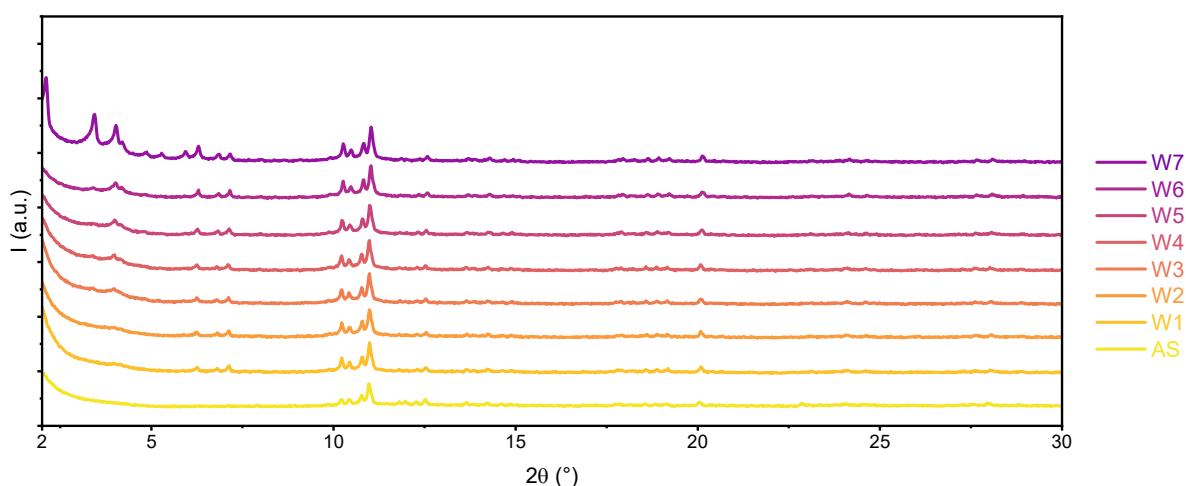


Fig. 4.24: PXRD patterns of the new batch of (Fe)-MIL-100 samples after different water washing times

Chapter 5

Advanced synchrotron radiation techniques

Some of the samples, synthesized as described in the previous chapters, were brought to APE beamline at Elettra Synchrotron of Trieste for further analyses. The APE (Advanced Photoelectric effect Experiments) beamline is conceived as a surface science laboratory for advanced spectroscopies and is composed of two distinct branches: APE-LE (Low Energy) devoted to Angle-resolved photoemission spectroscopy (ARPES) and APE-HE (High Energy) dedicated to X-ray absorption spectroscopy (XAS) and X-ray photoelectron spectroscopy (XPS) in the soft X-ray range. Despite the use of synchrotron radiation APE-HE beamline offers the chance to use a second XPS supplied by a personal Roentgen X-ray tube. We measured the samples with this independent XPS instrumentation in order to obtain preliminary results useful for the future XAS experiment scheduled at the end station of APE-HE beamline.

5.1 XPS: X-ray Photoelectron Spectroscopy

X-ray Photoelectron Spectroscopy (XPS), also known as Electron Spectroscopy for Chemical Analysis (ESCA), is commonly used to investigate the chemical composition of surfaces. XPS enables to explore the first few atomic layers and finds its main application in the assignment of the chemical states of detected atoms.

5.1.1 Introduction

X-ray Photoelectron Spectroscopy (XPS) was developed by Kai Siegbahn and his research group in the mid-1960s at the University of Uppsala, Sweden. In 1981, thanks to his work with XPS, Siegbahn was awarded with the Nobel Prize for Physics [56].

Surface analysis using XPS involves irradiating a solid *in vacuo* with soft monoenergetic X-rays and analyzing the emitted electrons by energy. Since the average free electron path in solids is very short, the detected electrons only come from the top few atomic layers, rendering XPS a surface-sensitive technique for chemical analysis.

The spectrum obtained is a chart of the number of electrons detected (intensity) versus their kinetic or binding energy (that is the energy of the orbital of the electron in the atom). The spectrum of a single element is unique, like a fingerprint. The spectrum of a mixture of elements is approximately the sum of the peaks of the single components [56]. Quantitative data can be extracted from peak heights or peak areas, and the identification of chemical states of the elements can often be made from the exact measurement of peak positions (which often show small energy shifts depending on the oxidation state) and shape [56].

5.1.2 Physical phenomenon involved: photoelectric effect

The sample is irradiated with soft X-ray, as $K\alpha_1$ line of Al (1486.7 eV) or Mg (1253.6 eV), which penetrate the solid by only 1-10 micrometers. Hence, they interact only with the surface of the sample causing electron emission by photoelectric effect from the top atoms [56].

The X-ray photon is first absorbed by the sample causing the expulsion of one electron from its atomic orbital (fig. 5.2-a). According to the energy conservation law, the emitted photoelectron moves with a kinetic energy given by [56]:

$$KE = h\nu - BE - \phi$$

where $h\nu$ is the energy of the incident photon, BE is the binding energy of the atomic orbital from which the photoelectron originates, and ϕ is the spectrometer work function

The binding energy is the energetic difference of the electron between the Fermi level (free electron) and the original orbital. The more the electron is bound and close to the nucleus the higher the binding energy is. The p, d and f orbitals become split upon ionization due to the spin-orbit effect [56]. Moreover, there is a different probability or cross-section for each orbital to undergo ionization [56]. Relative binding energies and ionization cross-sections for an atom are shown schematically in fig. 5.1. Each element has its unique energy levels hence unique XPS spectrum. Little shifts in the elemental binding energies arise from differences in the chemical potential and polarizability due to different chemical states of the compound [56].

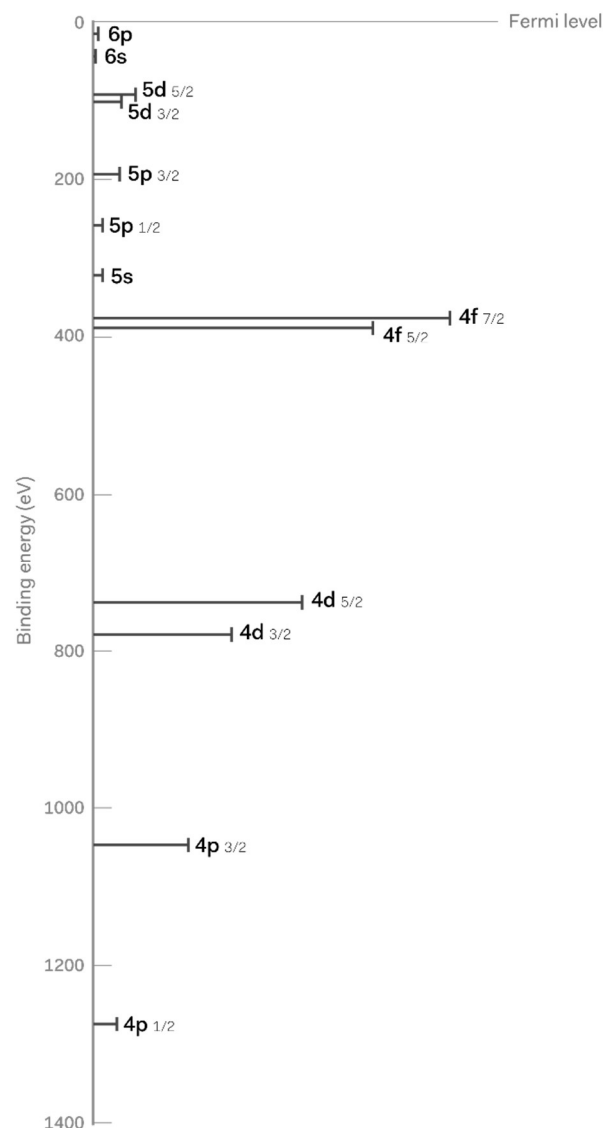


Fig. 5.1: example of an atomic energy structure

The excited state resulting from the photoelectron emission process consists of a core hole. After the absorption the atom undergoes a relaxation process in which the core-hole is filled by an electron from a higher energy level [57]. For energy balance another and less tightly bound electron is emitted (Auger emission) (fig. 5.2-b) [57]. The competing emission of a fluorescent X-ray photon is a minor process in this energy range [56].

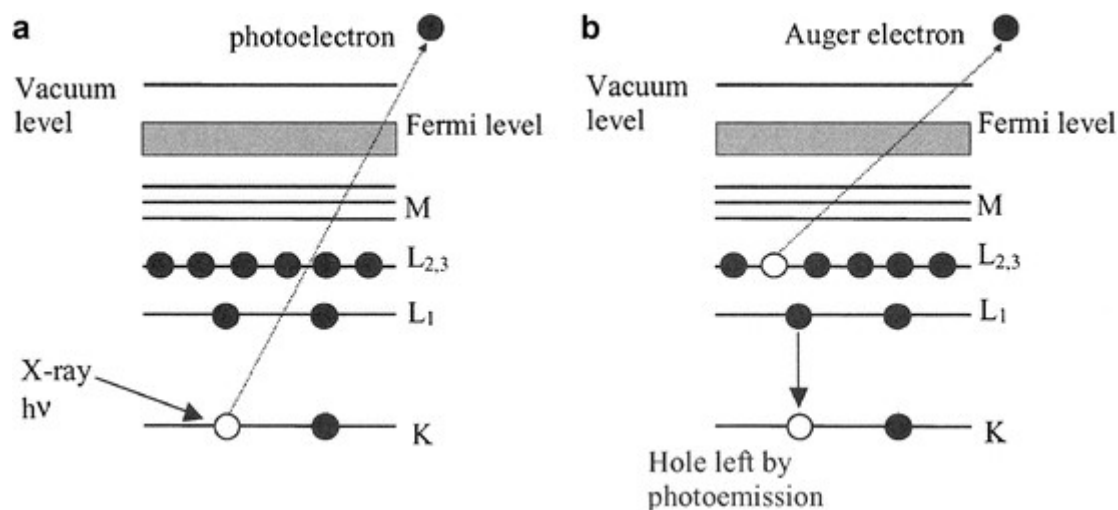


Fig. 5.2: a) absorption of an X-ray photon causing the emission of an electron from the core levels (photoelectron). b) relaxation process of Auger emission: one electron from a higher level fills the vacancy left by the photoelectron and simultaneously another electron is emitted for achieving energy conservation. [57]

While photoelectrons have fixed binding energies and shifted kinetic energies as the energy of the X-ray source changes, Auger electrons have fixed kinetic energies and shift their binding energy positions.

An XPS spectrum is the sum of photoelectrons (which give information about the core levels energies of the atom) and of the Auger electrons [56].

Electrons interact with matter much more easily than photons, hence while the photons excite atoms up to few micrometers deep, only electrons generated a few Angstroms from the surface reach the detector without energy loss [56]. Electrons that, instead, undergo inelastic scattering against matter, and lose energy before being detected, are called secondary electrons and are responsible for the background line of the XPS spectrum.

CHAPTER 6

XPS characterization of synthesized samples

For each of the target frameworks, the sample with the highest crystallinity was analyzed at the Roentgen tube supplied XPS of APE beamline in, at least, three different states: pristine, activated and treated *ex situ* with water vapour, aiming to observe the effect of activation and water to the surface of our MOFs.

6.1: (Mn) and (Co) MOF-74

The available sample of (Co)-MOF-74 showing the highest crystallinity, hence selected for XPS analyses, was the *activated* one (no powder was left of the non-activated and slightly more crystalline state) while, for the (Mn)-MOF-74, was the *MeOH, EtOH and water* washed without activation.

6.1.1 Data collection

The analyses were performed with Al $K\alpha_1$ line (1486.7 eV) in a cell kept under ultra-high vacuum ($\sim 10^{-9}$ mbar). (Mn)-MOF-74 sample was prepared on carbon tape adhering to Mo sample-holder (fig. 6.1-a) while (Co)-MOF-74 sample was prepared on carbon tape adhering to Cu sample-holder (fig. 6.1-b). Both Mn and Co samples were analysed:

- **Pristine**
- **XPS-activated:** activated under ultra-high vacuum ($P \sim 10^{-9}$ mbar) for 45 minutes, heated by a filament at 0.8 A at a temperature of $\sim 100^\circ\text{C}$ (fig. 6.2-a)
- **XPS-H₂O:** exposed to distilled water vapour at $\sim 10^{-7}$ mbar for 20 minutes after activation

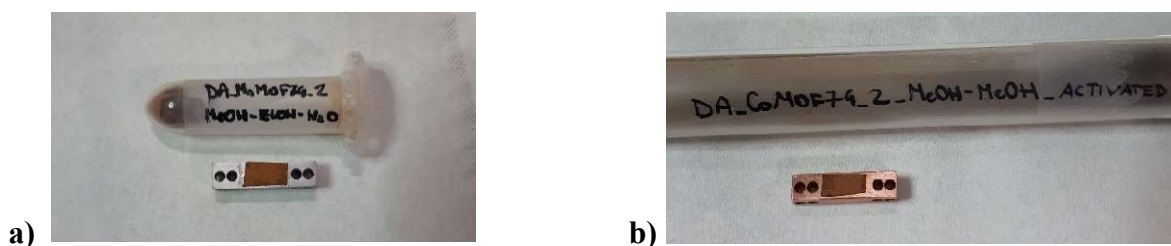


Fig. 6.1: Mn (a) and Co (b) prepared sample for XPS.

For each state a survey spectrum covering a wide range of energies (from 100 to 1490 eV of kinetic energy) was taken as well as short range highly resolved spectra of the metal 2p lines and oxygen 1s line.

Since after activation and water exposure no huge differences were observed, especially in the 2p lines of the metals, more extreme activation and water exposure were performed on the manganese sample as follows:

- **XPS-activated-2:** activated under ultra-high vacuum ($P \sim 10^{-9}$ mbar) for 45 minutes, heated by a filament at 1.1 A at a temperature of $\sim 120^\circ\text{C}$ (fig. 6.2-b)
- **XPS-activated-3:** activated under ultra-high vacuum ($P \sim 10^{-9}$ mbar) for 30 minutes at 1.3 A and 30 minutes at 1.4 A at a temperature of $\sim 150^\circ\text{C}$ (fig. 62-c)
- **XPS-H₂O-2:** exposed to distilled water vapour at $\sim 10^{-7}$ mbar for 1 hour after the third activation



Fig: 6.2: (Mn)-MOF-74 sample under activation at 0.8 A (a), 1.1 A (b) and 1.14 A (c)

6.1.2 Data manipulation

Each collected survey and core levels spectra were plotted on binding energies aligned with 4f lines of Au. Core levels spectra have also undergone a $K\alpha_3$ $K\alpha_4$ subtraction process that allowed for an efficient removal of the satellites caused by non-monochromatic source (fig 6.3). For subtraction, the values of the satellites' energies displacement and intensity reported

in book [56] were followed (table 6.1). To compare the core levels peaks of the sample in different states each spectrum was also normalized.

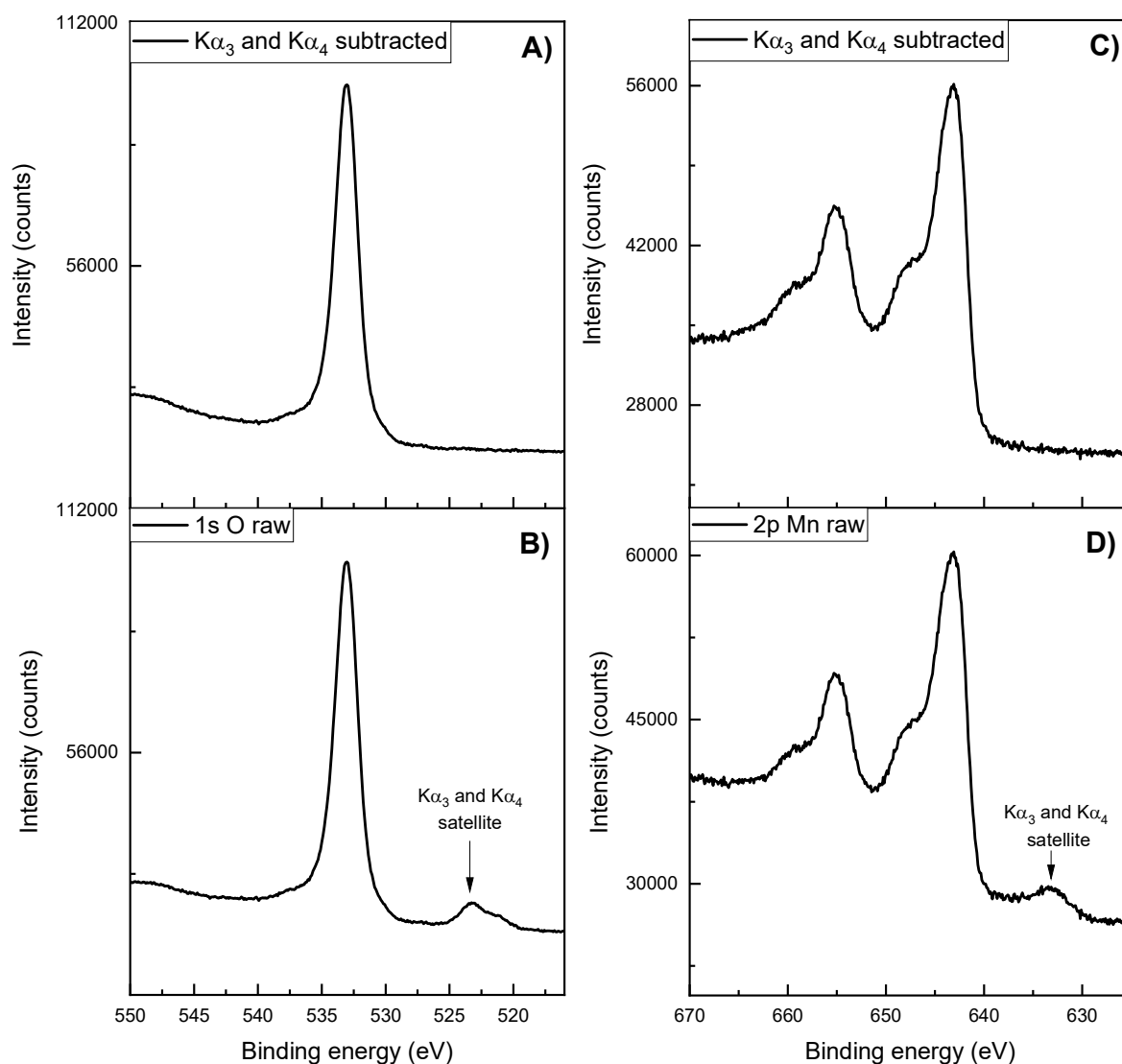


Fig. 6.3: 1s O core-level (A and B) and 2p Mn (C and D) of the manganese MOF-74 XPS-activated sample before (raw, bottom) and after subtraction of $K\alpha_3$ $K\alpha_4$ satellites ($K\alpha_3$ $K\alpha_4$ subtracted, top).

Table 6.1: Al X-ray satellites energies and intensities

	$K\alpha_{1,2}$	$K\alpha_3$	$K\alpha_4$
Energy displacement (eV)	0	9.8	11.8
Relative height	100	6.4	3.2

Moreover, some Auger peaks were analysed smoothing the raw data to lower the background noise and thus allowing for a clearer first derivative which has been plotted on kinetic energy.

6.1.3 Results and data interpretation

Peaks assignment

The survey spectra of (Co) and (Mn)-MOF-74 Pristine samples (fig.6.4) confirm the presence of Co, O, C and of Mn, C and O in the samples respectively. Co/Mn 2p, 3s and 3p lines were identified as well as O 1s line and C 1s line and, also, many Auger lines of Co/Mn, O and C. Also, some lines of the sample-holder (Cu in (Co)-MOF-74 and Mo in (Mn)-MOF-74) are visible.

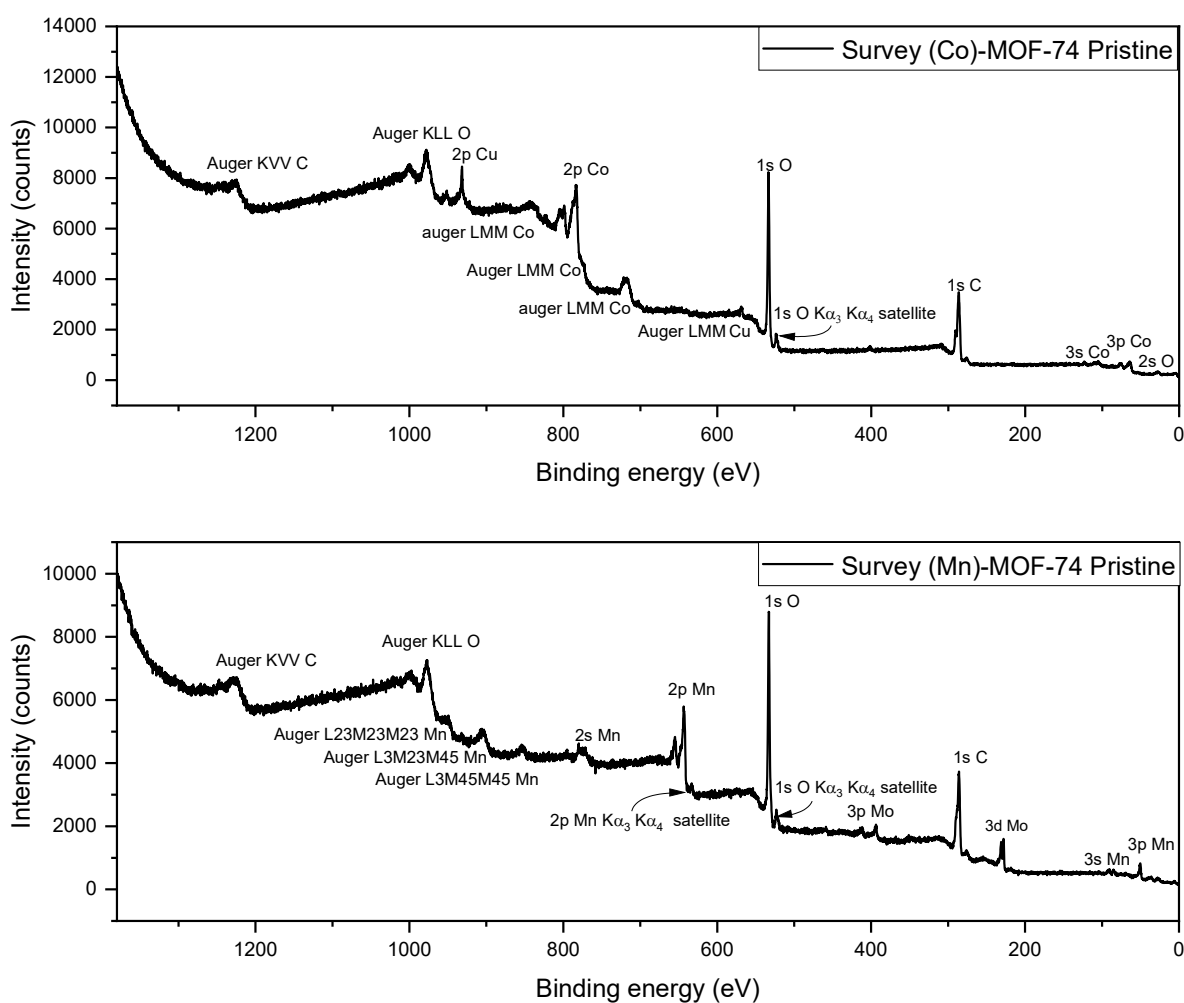


Fig. 6.4: XPS survey spectra of (Co)-MOF-74 (top) and (Mn)-MOF-74 (bottom).

After alignment with 4f lines of gold we observed that the positions of the peaks of the sample-holders (Cu and Mo) are perfectly in agreement with the ones reported in literature for the metallic state and, also, that the valence band of such metals ends exactly at 0 eV, sign that no charge effect occurred on the sample-holders. Insulators, on the other hand, may

charge during the measurement because they fail to compensate for the loss of electrons due to the photoelectric effect. If this happens, the ejected electrons are influenced by the electric field generated, causing a rigid shift in the peak positions (“charge effect”).

Even though the sample-holders haven’t charged, both Mn and Co lines shows unrealistic shifts if considered both metallic or M(II) oxide and non-charged. Instead, considering a charge effect of +2 eV for the (Mn)-MOF-74 and of +3 eV for the (Co)-MOF-74 makes all the experimental 3p, 3s and 2p shifts matching with the ones reported in literature for Mn(II) in MnO and Co(II) in CoO (table 6.2 and 6.3), suggesting that Mn(II) and Co(II) are present on the surface of our samples, as expected for the MOF-74 framework.

More specifically we obtained 2p_{3/2} line of Mn at 643 eV while in literature the position for MnO and/or for Mn(II) in MOF-74 framework is reported around 641eV [56], [58]–[60]. For Co we observed the 2p_{3/2} line at 783.3 eV and literature reports values around 780-781 eV for Co(II) in CoO and/or (Co)-MOF-74 [56], [61], [62].

Table 6.2: Mn(II) XPS core levels binding energies in (Mn)-MOF-74. *: values observed with gold alignment. ** literature data for MnO

Mn(II)	Experimental*/ eV	Literature **/ eV	Δ / eV	Literature source
3p	50	48.2	1.8	NIST XPS database
3s	85	82.8	2.2	NIST XPS database
2p_{3/2}	643	641	2.0	[56]

Table 6.3: Co(II) XPS core levels binding energies in (Co)-MOF-74. *: values observed with gold alignment. ** literature data for CoO

Co(II)	Experimental*/ eV	Literature**/ eV	Δ / eV	Literature source
3p	63.5	60.6	2.9	NIST XPS database
3s	105.5	102.2	3.3	NIST XPS database
2p_{3/2}	783.3	780.5	2.8	[56]

Another proof that the metal-organic framework samples have charged is suggested by the Auger lines: in the first derivative plot of the LMM lines of Mn and Co we qualitatively observed kinetic energy shifts of ~-2 eV for Mn and of ~-3 eV for Co, which correspond to binding energy shifts of ~+2 and ~+3 eV respectively.

Moreover, the 1s line of oxygen is shifted of ~+3 and ~+3.5 eV in the Mn and Co sample in respect to literature reported positions for O in Mn and Co oxides [63]–[65] (table 6.4 and 6.5). Considering that in the MOF-74 framework there are two types of oxygen, the coordinated to the metal M-O one and the one of the hydroxyl groups of the ligands, and considering also that the shifts for O in O-H groups are generally at higher binding energies [63], the experimental values of our 1s O line, which is given by both types of O, well match with the charge effect proposed.

Table 6.4: O XPS 1s core level binding energies in (Mn)-MOF-74. *: values observed with gold alignment. ** literature data for MnO

O	Experimental*/ eV	Literature**/ eV	Δ / eV	Literature source
1s	533	530	3	NIST XPS database

Table 6.5: O XPS 1s core level binding energies in (Co)-MOF-74. *: values observed with gold alignment. ** literature data for CoO

O	Experimental*/ eV	Literature**/ eV	Δ / eV	Literature source
1s	533.5	530	3.5	NIST XPS database

Manganese(II) and cobalt(II) 2p satellites

The 2p metal core level of both (Mn) and (Co)-MOF-74 shows less intense components at higher binding energies (fig. 6.5). Since the 3p and 3s lines of the metals don't show any double peak, we have ruled out the possibility of two oxidation states of the metal inside the sample and, according to previous literature, we attributed those peaks to the satellites of the 2p lines occurring for MnO and CoO [62], [66], [67].

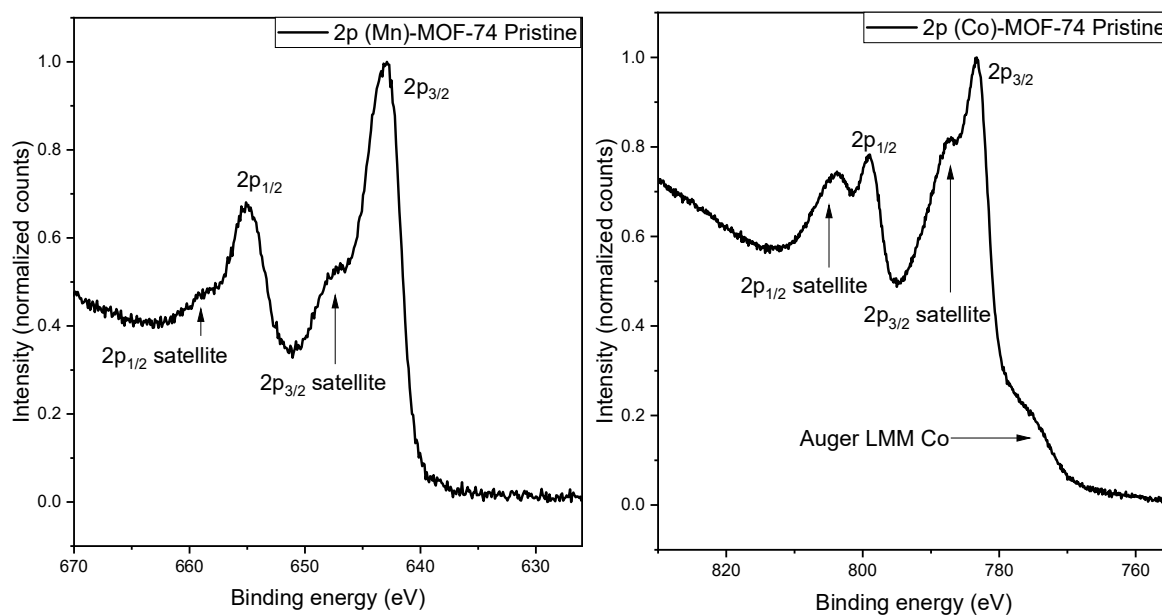


Fig. 6.5: 2p lines of (Mn)-MOF-74 (left) and of (Co)-MOF-74 (right) with respective satellites.

Pristine, XPS-activated, XPS-H₂O core levels comparison

Both (Mn)-MOF-74 and (Co)-MOF-74 were analyzed with XPS pristine, then activated at ~100°C for 45 minutes heated by a filament at 0.8 A and then re-analyzed with XPS.

For the Co sample no change in the XPS spectra of 1s O or 2p Co were observed, sign that the activation procedure has not modified the sample (fig. 6.6-B). For Mn sample, instead, after activation was observed the loss of the small component at lower binding energies in the

1s O peak (fig. 6.6-C). We attribute this small peak to oxygen present in impurities strongly adsorbed on the sample, while the main peak is due to the O of the framework. In fact, the manganese MOF-74 had not undergone any activation process prior to the XPS measurement. In contrast, the cobalt sample, which had previously undergone an activation process, does not display this additional component of the oxygen peak.

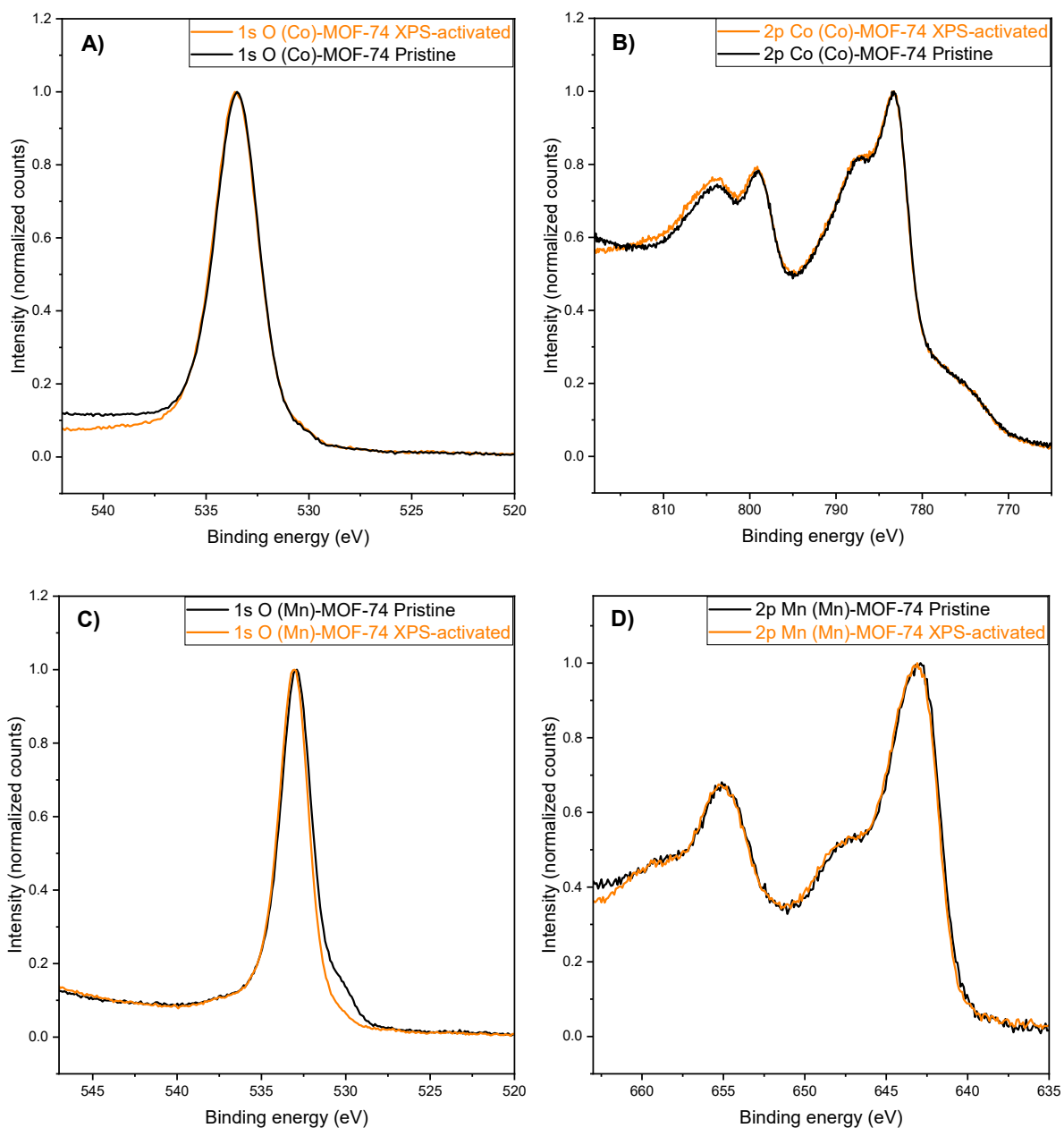


Fig. 6.6: 1s O (A) and 2p Co (B) core levels of pristine (black) and XPS-activated (orange) (Co)-MOF-74 sample and 1s O (C) and 2p Mn (D) core levels of pristine (black) and XPS-activated (orange) (Mn)-MOF-74 sample. Peaks' positions are affected by estimated charge effect of +3 and +2 eV for Co and Mn samples respectively.

After activation the samples have been treated *ex situ* with distilled water vapour at $\sim 10^{-7}$ mbar for 20 minutes then measured with XPS: the survey spectrum of both compounds shows no change in respect to the XPS-activated one, suggesting that the activation procedure was

not effective in vacuuming the pores (and thus making space for new water molecules) or that water was not absorbed permanently by the sample because immediately desorbed due to the ultra-high vacuum environment in which the samples were permanently stored.

(Mn)-MOF-74 further activations and water exposure

Therefore, stronger activations were investigated for the (Mn)-MOF-74 sample, heating at $\sim 120^\circ\text{C}$ (XPS-activated-2) and $\sim 150^\circ\text{C}$ (XPS-activated-3). After activation at $\sim 120^\circ\text{C}$ the sample's survey spectrum still showed no difference. After the third activation, at $\sim 150^\circ\text{C}$, the resulting XPS spectrum presented some small differences: the 2p Mn lines and 1s O line were shifted toward lower binding energies of ~ 0.7 eV (fig 6.7). and the 1s C peak intensity ratio modified (fig 6.8). We think that the high temperatures degraded the carbon tape on which the sample was glued causing different charge effect on the MOF (hence the small shift of Mn and O lines) and diverse intensity ratio of the 1s line of carbon.

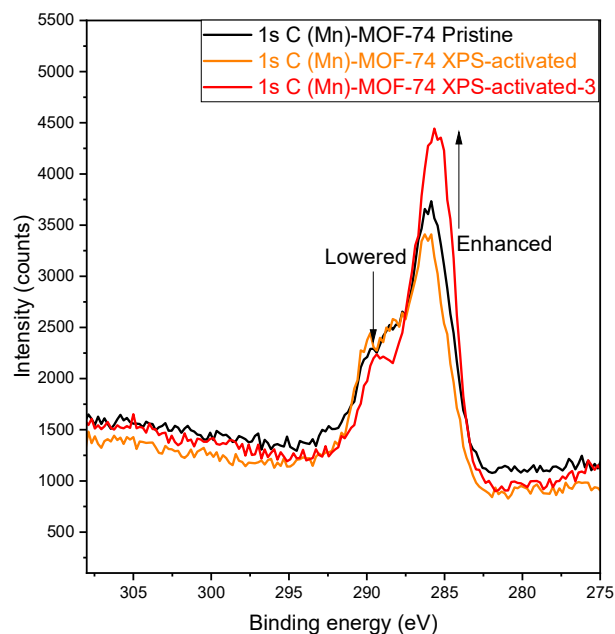


Fig. 6.8: 1s C peak from low resolution survey spectra: the XPS-activated-3 one shows a significantly different intensity ratio of the two components

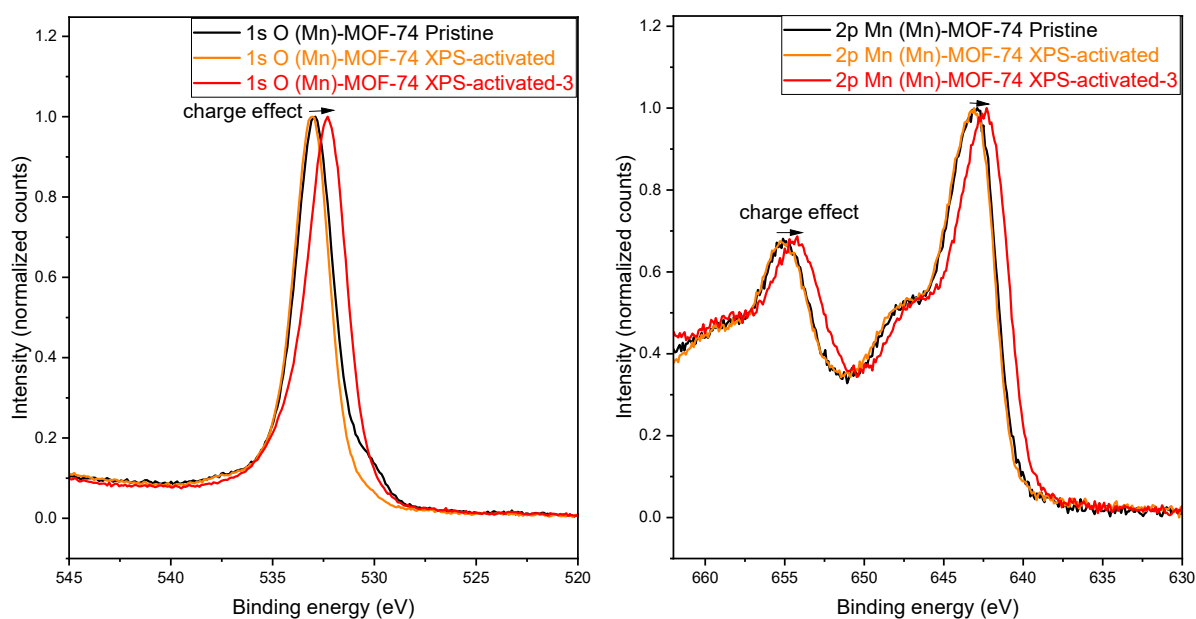


Fig 6.7: Different charge effect of the XPS-activated-3 sample in respect to the one of pristine and XPS-activated. Note that the peaks of pristine and XPS-activated samples are still affected by estimated charge effect of +2 eV.

Also, after correction of the new charge effect aligning the XPS-activated-3 peaks with the ones of the pristine sample, the 1s O line displays an enlargement toward higher binding energies ascribable to carboxylates or highly oxidated carbonyl compounds generated during the strong heating [68] (fig. 6.9). After the third activation the sample has been again exposed to water vapour for a longer time (1 h) however both Mn 2p and O 1s spectra remained perfectly identical to the XPS-activated-3 ones (fig. 6.9).

Hence, since even after stronger activation and water exposure the sample's XPS spectrum hadn't showed traces of water, we ruled out the possibility of an incomplete activation and deduced that water desorbs very quickly from the MOF under ultra-high vacuum conditions.

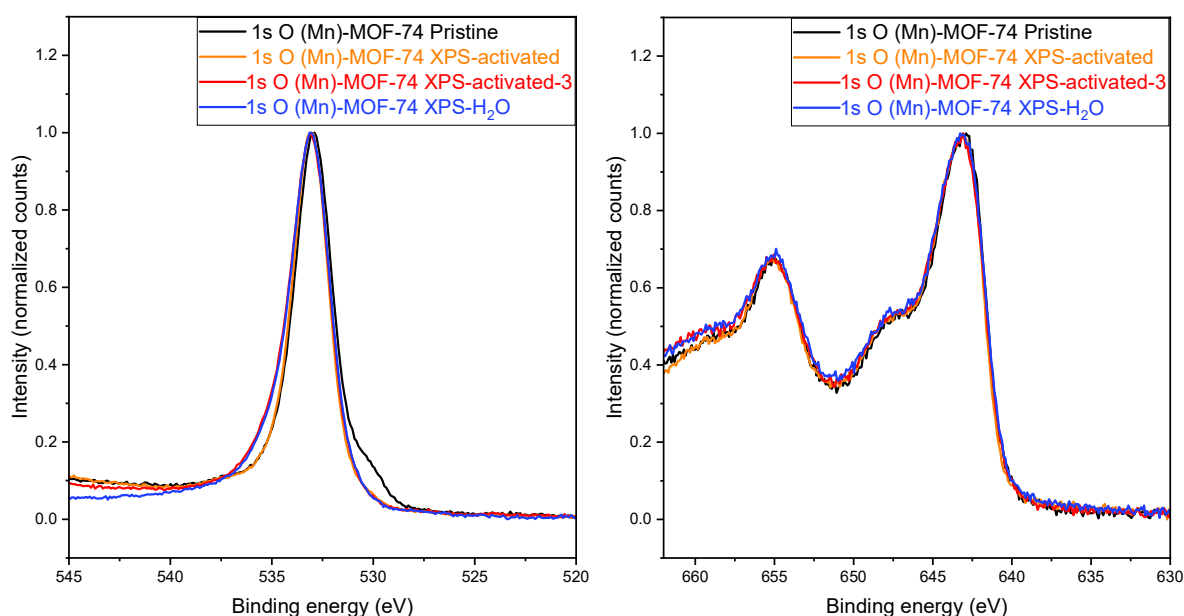


Fig. 6.9: Comparison between the 1s O (left) and 2p Mn (right) of different states of (Mn)-MOF-74 sample. XPS-activated-3 and XPS-H₂O spectra have been aligned with the Pristine and XPS-activated ones correcting the difference in the charge effect shift. Note that the peaks are still affected by estimated charge effect of +2 eV.

Work-up comparison for (Mn)-MOF-74

(Mn)-MOF-74 sample analyzed until here was, as previously described, the one showing the highest crystallinity, that is the methanol, ethanol and water washed without previous activation before XPS analyses. We also analysed with XPS another sample of (Mn)-MOF-74 that had undergone a different work-up, i.e. one that had been washed with methanol and ethanol, activated at 170°C and then re-crystallised with water baths. Thus, we compared the pristine spectra of the two differently processed sample. As illustrated in fig. 6.10, the 2p lines of Mn overlap nicely, showing no significant changes, while the 1s O line of the activated and re-crystallised (Mn)-MOF-74 broadened toward lower binding energies. This

may be attributed to more components generating the O peak: in fact the re-crystallised sample underwent an activation process which had completely degraded it, as PXRD analyses showed, and it's likely to assume that, even after the re-crystallization in water, some defects in the structure remained, so that multiple chemical states of oxygen may be present.

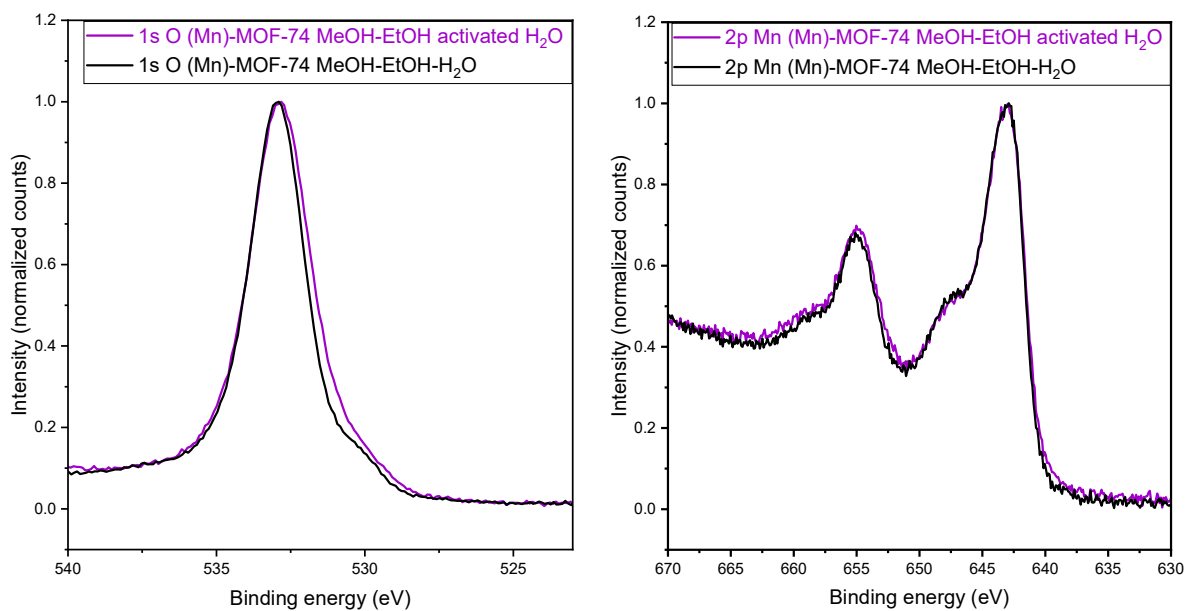


Fig. 6.10: comparison of the O and Mn core levels of differently processed (Mn)-MOF-74. Peaks' positions are affected by estimated charge effect of +2 eV.

6.2 (Fe)-MIL-100

The sample of (Fe)-MIL-100 showing the highest crystallinity, hence selected for XPS analyses, was the one which had been washed seven times(W7).

6.2.1 Data collection

The analyses were performed with Al $K\alpha_1$ line (1486.7 eV) in a cell kept under ultra-high vacuum ($\sim 10^{-9}$ mbar). (Fe)-MIL-100 W7 sample was prepared on carbon tape adhering to Mo sample-holder (fig. 6.11-a). As for the MOF-74, also (Fe)-MIL-100 has been analysed in three different states:

- **Pristine**
- **XPS-activated:** activated under ultra-high vacuum ($P \sim 10^{-9}$ mbar) for 45 minutes, heated by a filament at 0.8 A at a temperature of $\sim 100^\circ\text{C}$ (fig. 6.11-b)
- **XPS- H_2O :** exposed to distilled water vapour at $\sim 10^{-7}$ mbar for 20 minutes after activation

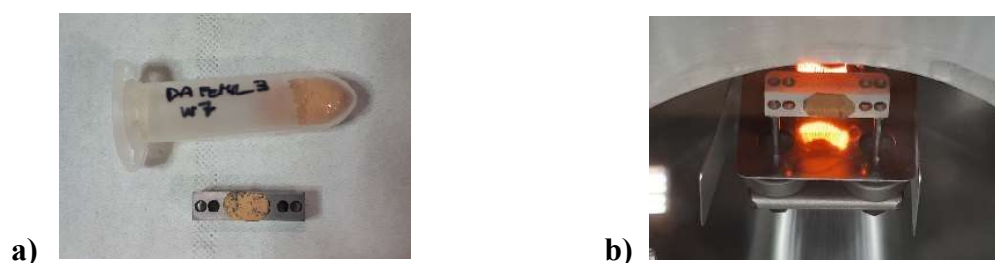


Fig. 6.11: (Fe)-MIL-100 prepared sample for XPS (a) and during activation heated by a filament at 0.8 A (b)

For each state a survey spectrum covering a wide range of energies (from 100 to 1490 eV of kinetic energy) was taken as well as short range highly resolved spectra of the metal 2p lines and oxygen 1s line.

6.2.2 Data manipulation

Data collected from (Fe)-MIL100 framework were subjected to the same data processing as those from (Mn) and (Co)-MOF-74, i.e. alignment with 4f lines of Au for all spectra and $K\alpha_3$ $K\alpha_4$ subtraction process for the spectra of the core levels (fig 6.12).

To compare the core levels peaks of the sample in different states, each spectrum was also normalized. Moreover, some Auger peaks were analysed calculating the first derivative on kinetic binding energy.

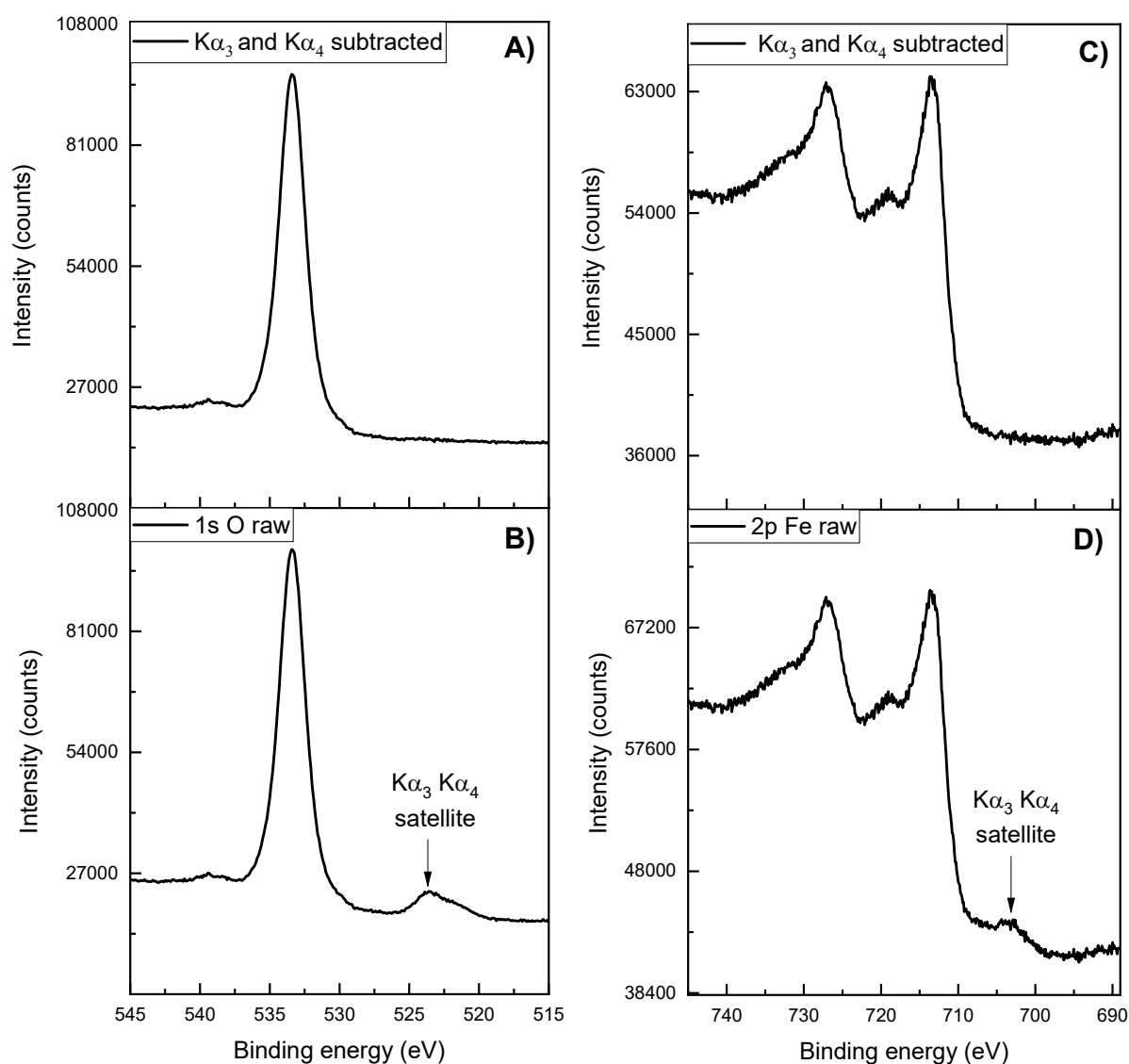


Fig. 6.12: 1s O core-level (A and B) and 2p Fe core level (C and D) of (Fe)-MIL-100 pristine before (raw, bottom) and after subtraction of $K\alpha_3$ $K\alpha_4$ satellites ($K\alpha_3$ $K\alpha_4$ subtracted, top).

6.2.3 Results and data interpretation

Peaks assignment

The survey spectra of (Fe)-MIL-100 Pristine sample (fig.6.13) confirm the presence of Fe, O, C. Fe 2p, 3s and 3p lines were identified as well as O 1s line and C 1s line and, also, many Auger lines of Fe, O and C. More, some lines of the Cu sample-holder are visible.

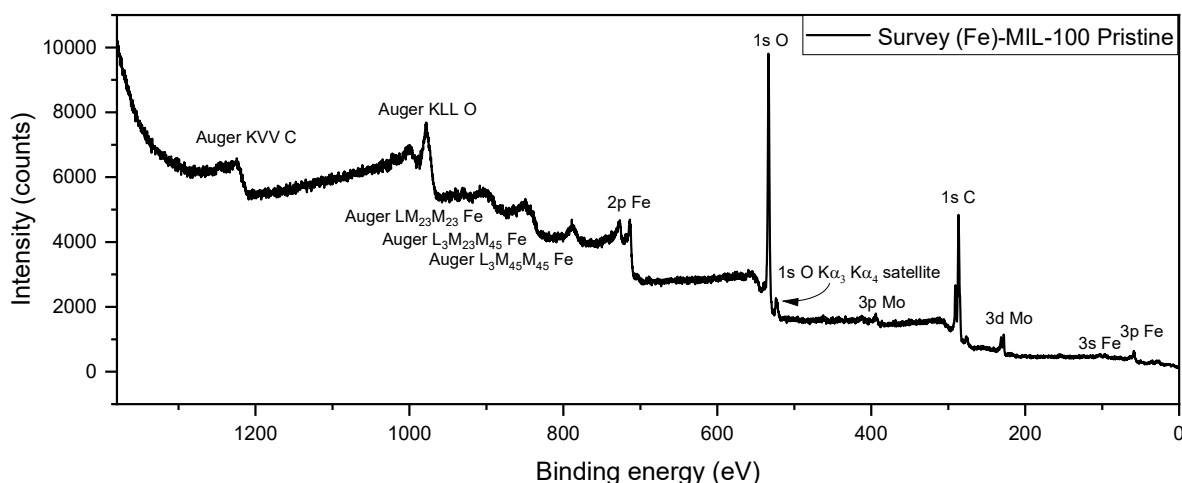


Fig. 6.13: XPS survey spectra of (Co)-MOF-74 (top) and (Mn)-MOF-74 (bottom).

After alignment with 4f lines of gold we observed, also for (Fe)-MIL-100, that the positions of the peaks of the sample-holder (Cu) are perfectly in agreement with the ones reported in literature for the metallic state, and that the valence band ends exactly at 0 eV, sign that no charge effect occurred on the sample-holder

However, as occurred for both Mn and Co, the Fe lines shows unrealistic shifts if considered non-charged, while, considering a charge effect of +1 or + 2 eV makes all the experimental 3p, 3s and 2p shifts matching with the ones reported in literature for Fe(III) in Fe₂O₃ and (Fe)-MIL-100 (table 6.6) More specifically we obtained Fe 2p_{3/2} line at 713 eV while in literature the position for Fe 2p in (Fe)-MIL-100 framework is reported around 711-712 eV [56], [69], [70].

Table 6.6: Fe(III) XPS core levels binding energies in (Fe)-MIL-100. *: values observed with gold alignment. ** literature data for Fe₂O₃

Fe(III)	Experimental*/ eV	Literature **/ eV	Δ / eV	Literature source
3p	58	56	2	NIST XPS database
3s	96.	94	2	NIST XPS database
2p _{3/2}	713.5	711-712.6	0.9 to 2.5	[56], [70]

Moreover, looking at the Auger $L_3M_{45}M_{45}$ position of Fe in the first derivative plot of the raw data, we obtained a value <700 eV in kinetic energy that is in agreement with the trend studied by Z. Li and U. Becker [71] in Fe compounds showing a shift toward kinetic energy <700 eV for Fe_2O_3 .

Also, we observed 1s O line around 533.5 eV, that is shifted of $\sim+1.5$ eV in respect to the value (532 eV) reported in literature [70] for Fe-O-C species (table 6.7), validating the estimation of the charge effect shift around 2 eV.

Table 6.7: O XPS 1s core level binding energies in (Fe)-MIL-100. *: values observed with gold alignment. ** literature data for Fe-O-C species.

O	Experimental*/ eV	Literature**/ eV	Δ / eV	Literature source
1s	533.5	532	1.5	[70]

Iron(III) 2p satellites

As reported in literature Fe(III) 2p lines are accompanied by small satellites at higher binding energies [70], [72]. In figure 6.14 is reported the spectrum of our experimental 2p lines of Fe showing $2p_{3/2}$ at 713.5 eV and $2p_{1/2}$ at 727 (values affected by estimated charge effect of $\sim+1$ or 2 eV). Each 2p line presents two satellites, for the $2p_{3/2}$ peak the second and more distant satellite falls under the $2p_{1/2}$ peak, while for $2p_{1/2}$ both satellites are visible. Table 6.8 reports the positions of observed satellites.

Table 6.8: Binding energies of 2p satellites of Fe(III). Values are affected of an estimate charge effect of +1 or +2 eV.

	1st sat. / eV	2nd sat. / eV
$2p_{1/2}$.	733	745
$2p_{3/2}$	719	Not visible

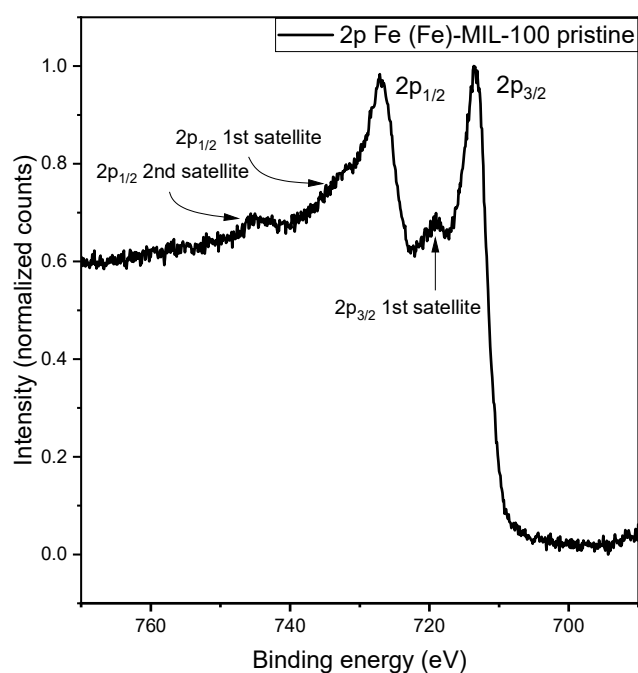


Fig. 6.14: (Fe)-MIL-100 2p lines of Fe and satellites. Peaks' positions are affected by estimated charge effect of +1 to +2 eV.

Pristine, XPS-activated, XPS-H₂O core levels comparison

We compared the core level spectra of 1s O and 2p Fe of the three different states of (Fe)-MIL-00 we analyzed: pristine, activated at $\sim 100^\circ\text{C}$ (XPS-activated) and exposed to water vapour at $\sim 10^{-7}$ mbar after activation (XPS-H₂O) (fig.6.15). Despite the 1s line of oxygen doesn't change from one state to another the 2p lines of Fe shows a slight widening toward lower binding energies, suggesting the formation of Fe(II) [69]. We think that after activation and water exposure, reduction of some of the Fe(III) ions in the MIL-100 framework to Fe(II) began [22], [73]–[75].

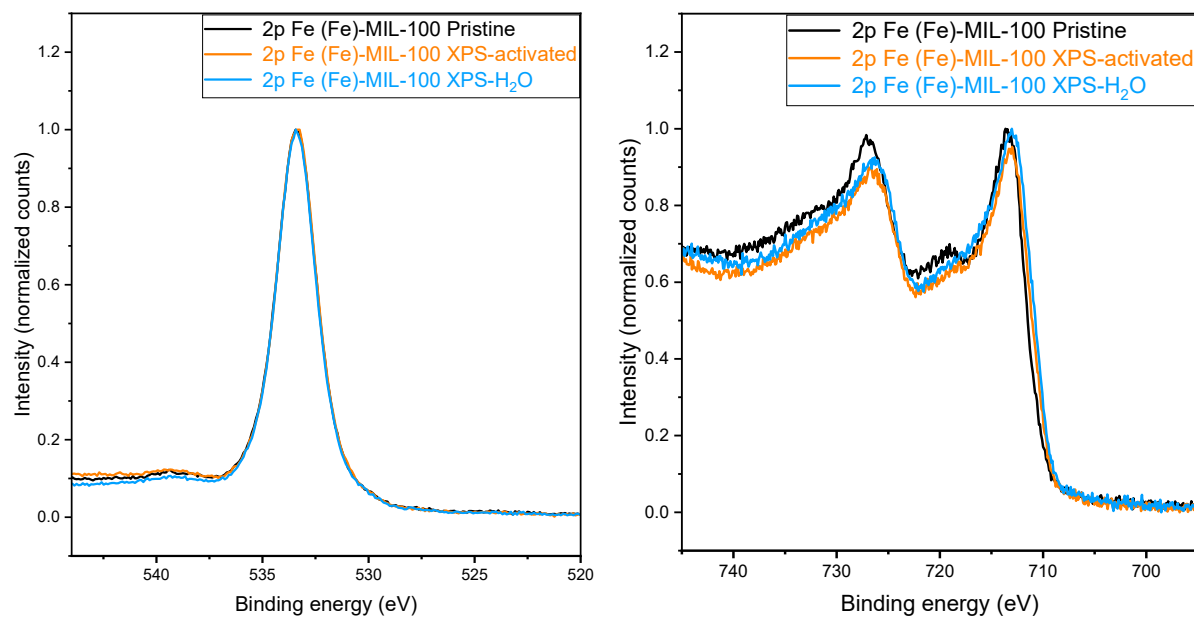


Fig. 6.15: XPS spectra comparison of 1s O and 2p Fe core levels of (Fe)-MIL-100 in three different states. Peaks' positions are affected by estimated charge effect of +1 to +2 eV.

Chapter 7

Experimental section

7.1 Instrumental characteristics

7.1.1 Infrared Spectroscopy

IR spectra were obtained using a Perkin-Elmer Paragon 1000 spectrometer (University of Milan) in the 4000-400 cm⁻¹ range. The analysis of the spectra was carried out with the software "Spectrum" provided by Perkin-Elmer itself.

7.1.2 Powder X-ray Diffraction

PXRD diffractograms were recorded using a Bruker D8 Advance diffractometer (University of Milan) equipped with a Lynxeye detector and Cu-K α radiation ($\lambda = 1.5418 \text{ \AA}$). Generator settings: 40 kV, 40 mA. The diffraction patterns were processed with the EVA software. The fast data collections were performed with a scanspeed of 0.2s per step. More precise collections were performed with a scanspeed of 1s per step.

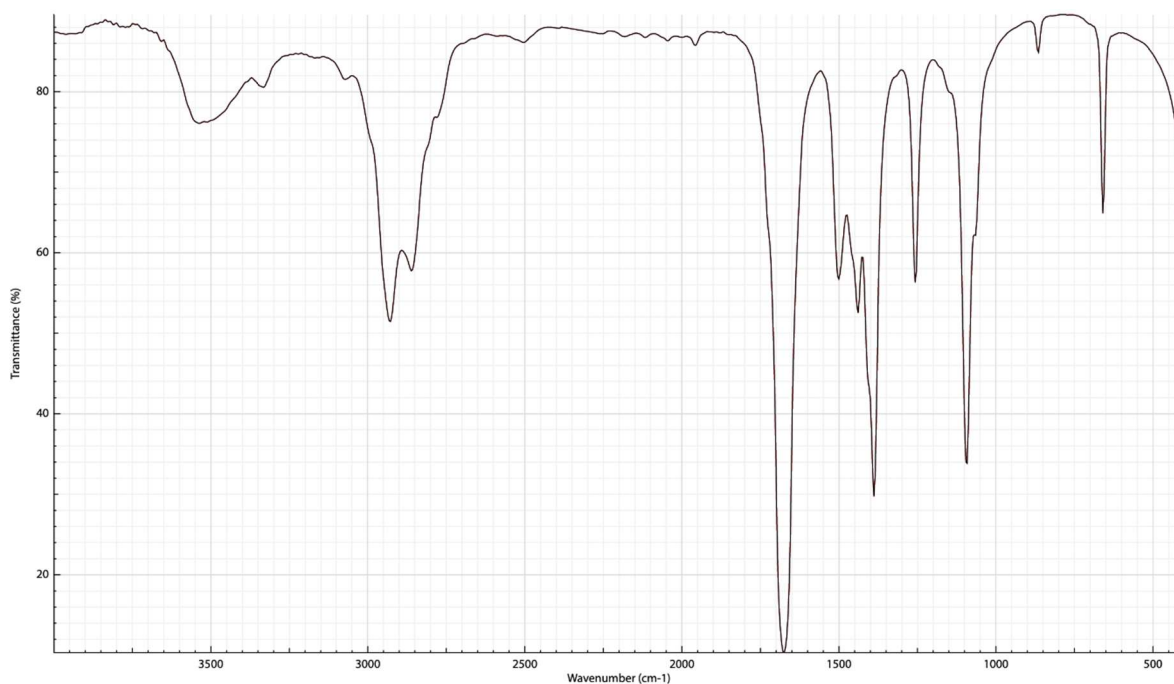
7.1.3 Le Bail fitting of PXRD data

For the Le Bail fitting of the PXRD data, the "Topas 3" software has been used which makes advantage of Le Bail algorithm.

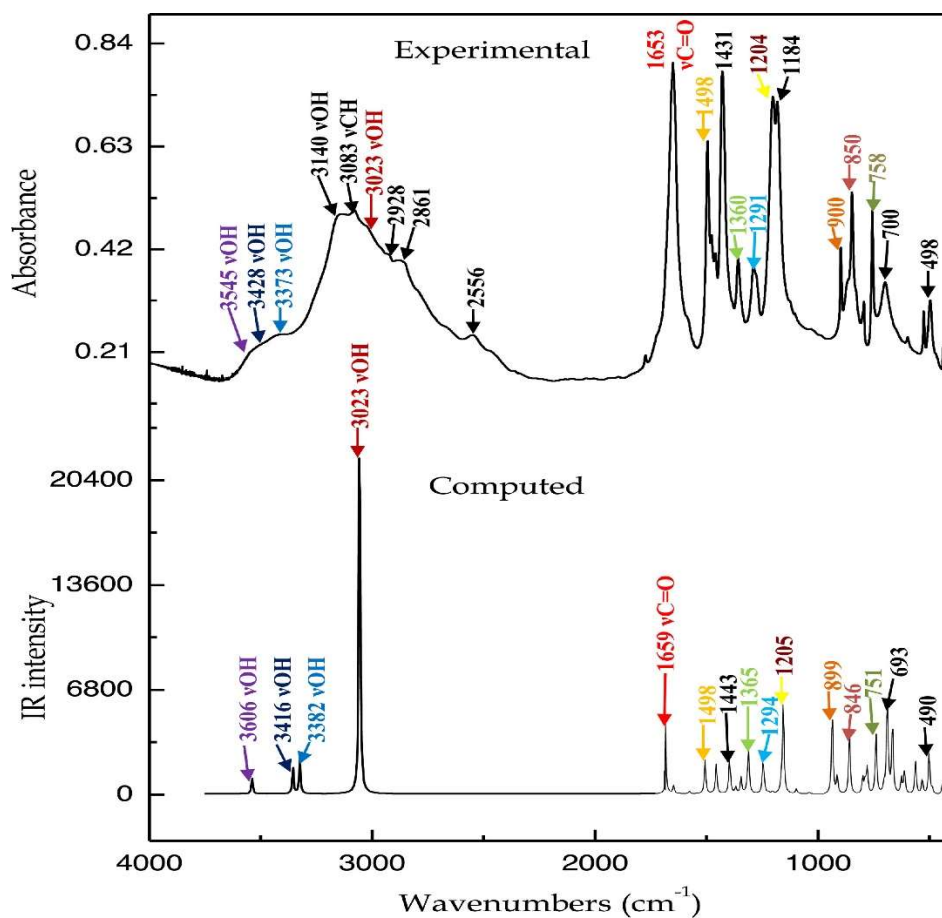
7.1.4 X-ray Photoelectron Spectroscopy

XPS analyses were performed with Al K α_1 (1486.7 eV) X-ray source in a cell under ultra-high vacuum ($<10^{-9}$ mbar). The hemispherical dispersing element of the analyzer is a commercial one, recently developed by MB Scientific AB [76]. Survey spectra are a 1 scan spectra covering a range from 100 to 1490 eV kinetic energy and were performed with a channel width of 2.3 mm, dwell time of 500 ms, PE (pass energy) of the analyzer set to 50 eV, MCP front 100, anode 100, MCP bias 1850. Core levels' spectra instead are the sum of 10 scans (for O 1s and 2p Mn lines) or 15 scans (for 2pFe lines) or 20 scans (for 2p Co lines) and were performed with a channel width of 1.1 mm, dwell time of 500 ms, PE (pass energy) of the analyzer set to 50 eV, MCP front 100, anode 100, MCP bias 1850.

7.2 Supplementary IR spectra



DMF IR spectrum



Dobdc (MOF-74's ligand) predicted IR spectrum (bottom) and experimental (top) from [77].

Chapter 8

Conclusions and future projects

8.1 Conclusions

The aim of this thesis work was the synthesis and characterization of (Mn) and (Co)-MOF-74 and (Fe)-MIL-100 metal-organic frameworks, three systems which feature open metal sites in the activated form, with a view to possible applications in the field of water harvesting.

(Mn) and (Co)-MOF-74 have been successfully synthesized and characterized with IR and PXRD to confirm the obtaining of the desired phase and crystallinity. We observed that the synthesized (Mn)-MOF-74 is not stable to air and degrades in 1-2 months, thus we hypothesize that impurities may induce or accelerate the degradation mechanism of the MOF. On the other hand, we successfully tested the water stability of both (Co) and (Mn)-MOF-74 after the washing procedures. After activation at 170°C, both (Co) and (Mn)-MOF-74 showed loss of crystallinity but, while the cobalt sample maintained, in any case, a quite good crystallinity, the Mn one almost fully degraded. Interestingly, the degraded (Mn)-MOF-74 re-crystallized with water baths and we hypothesize that the MOF may collapse when its pores got vacuumed and re-organizes while sunk in water, helped by solvation and water molecules filling the pores.

For (Fe)-MIL-100 we tested a reported mechanochemical green synthesis followed by a reconstruction procedure in water. The first attempt of the synthesis ended with a very low crystallinity compound. At the second attempt we obtained a discretely crystalline (Fe)-MIL-100. We hypothesize that the slow RT air drying method after water reconstruction is the key to achieve higher crystallinity. However, more experiments need to be done for better understanding which parameters affect the result.

For each of the target frameworks, the sample with the highest crystallinity was analyzed at the Roentgen tube supplied XPS of APE beamline at Elettra synchrotron (Trieste) in, at least, three different states: pristine, activated under ultra-high vacuum and treated *ex situ* with water vapour, aiming to observe the effect of activation and water to the surface of our MOFs.

The XPS analyses confirmed the presence of Mn(II) and Co(II) on the surface of the MOF-74 samples, ascribable to the metal ions of the framework, as well as Fe(III) on the surface of MIL-100 sample. We observed that, under ultra-high vacuum conditions, water is not permanently adsorbed by such frameworks and quickly desorbs away before it can be detected. Also, for (Fe)-MIL-100, after the activation and water exposure, starting of the reduction of some Fe(III) ions into Fe(II) has been noted.

8.3 Future projects

Since it is not possible to observe water adsorbed on the samples' surface with normal XPS because of the quick desorption under ultra-high vacuum conditions, it would be interesting to take advantage of NAP-XPS (Near Ambient Pressure X-ray Photoelectron Spectroscopy) technique present at Elettra synchrotron which would allow to study through XPS the behavior and kinetics of our samples' surface in real pressure conditions and/or while exposed to water vapour fluxes.

Also, we would like to take advantage of a novel reactor present at APE beamline [78] which performs *operando*-XAS (X-ray Absorption Spectroscopy) at ambient pressure and through which it is possible to monitor the $L_{2,3}$ edges of the transitions metal atoms during the whole process of gas adsorption. In particular, it would be possible to observe the water adsorption phenomena at the open metal sites and thus to better understand the structural-electronic modifications acting in the chemical environment around those exposed metal sites.

Greetings

I would like to thank all the people who contributed to the realization of this thesis project. In particular, a heartfelt thankyou to Marco Vandone who followed and coordinated me throughout my period of work at the University of Milan and who made a significant contribution to the drafting of this thesis. I would also like to thank all the guys in the group I worked with at the university (Tony Grell, Stephanie Terruzzi, Giovanni Moreddu, Giulia Taini) for all their advice and time spent together, and Il Son Khan, whom I had the pleasure to meet during his internship here in Italy.

I would also like to thank Luca Braglia, PostDoc at Elettra synchrotron, for his patient guidance, explanations and advice and answers to my questions and all the support during my internship on the APE-HE beamline, and Piero Torelli, responsible of the APE-HE beamline, for his important help in interpreting the data from XPS. I am also grateful to all the guys working at beamline APE-HE for their warm welcome and technical support in using the instruments.

Finally, I would like to give special thanks to my supervisor, professor Valentina Colombo, for the opportunity she gave me to participate in the wonderful internship I had at the Elettra synchrotron in Trieste.

Bibliography

- [1] R. Freund *et al.*, “25 Years of Reticular Chemistry,” *Angewandte Chemie International Edition*, vol. 60, no. 45, pp. 23946–23974, Nov. 2021, doi: 10.1002/ANIE.202101644.
- [2] S. R. Batten *et al.*, “Terminology of metal-organic frameworks and coordination polymers (IUPAC recommendations 2013),” *Pure and Applied Chemistry*, vol. 85, no. 8, pp. 1715–1724, Jul. 2013, doi: 10.1351/PAC-REC-12-11-20/MACHINEREADABLECITATION/RIS.
- [3] J. L. C. Rowsell and O. M. Yaghi, “Metal-organic frameworks: a new class of porous materials,” 2004, doi: 10.1016/j.micromeso.2004.03.034.
- [4] H. Li, M. Eddaoudi, M. O’Keeffe, and O. M. Yaghi, “Design and synthesis of an exceptionally stable and highly porous metal-organic framework,” *Nature 1999 402:6759*, vol. 402, no. 6759, pp. 276–279, Nov. 1999, doi: 10.1038/46248.
- [5] S. S. Y. Chui, S. M. F. Lo, J. P. H. Charmant, A. G. Orpen, and I. D. Williams, “A chemically functionalizable nanoporous material [Cu₃(TMA)₂(H₂O)₃](n),” *Science (1979)*, vol. 283, no. 5405, pp. 1148–1150, Feb. 1999, doi: 10.1126/SCIENCE.283.5405.1148/SUPPL_FILE/986116S4_THUMB.GIF.
- [6] A. G. Slater and A. I. Cooper, “Function-led design of new porous materials,” *Science (1979)*, vol. 348, no. 6238, p. aaa8075, May 2015, doi: 10.1126/SCIENCE.AAA8075/ASSET/452C8BC6-279A-4418-81AC-DE11D6E071B3/ASSETS/GRAPHIC/348_AAA8075_FA.JPEG.
- [7] “(PDF) Functionalized Metal-Organic Frameworks as Selective Metal Adsorbents.”
https://www.researchgate.net/publication/317577477_Functionalized_Metal-Organic_Frameworks_as_Selective_Metal_Adsorbents (accessed Aug. 18, 2022).
- [8] M. Fujita, J. Yazaki, and K. Ogura, “Preparation of a Macrocyclic Polynuclear Complex, [(en)Pd(4,4'-bpy)]₄(NO₃)₈, 1 Which Recognizes an Organic Molecule in Aqueous Media,” *J Am Chem Soc*, vol. 112, no. 14, pp. 5645–5647, 1990, doi: 10.1021/JA00170A042/ASSET/JA00170A042.FP.PNG_V03.
- [9] S. Horike, S. Shimomura, and S. Kitagawa, “Soft porous crystals,” *Nature Chemistry 2009 1:9*, vol. 1, no. 9, pp. 695–704, Nov. 2009, doi: 10.1038/nchem.444.

- [10] H. Furukawa, K. E. Cordova, M. O’Keeffe, and O. M. Yaghi, “The chemistry and applications of metal-organic frameworks,” *Science*, vol. 341, no. 6149. American Association for the Advancement of Science, 2013. doi: 10.1126/science.1230444.
- [11] W. L. Queen *et al.*, “Comprehensive study of carbon dioxide adsorption in the metal–organic frameworks M₂(dobdc) (M = Mg, Mn, Fe, Co, Ni, Cu, Zn),” *Chem Sci*, vol. 5, no. 12, pp. 4569–4581, Oct. 2014, doi: 10.1039/C4SC02064B.
- [12] F. Jeremias, A. Khutia, S. K. Henninger, and C. Janiak, “MIL-100(Al, Fe) as water adsorbents for heat transformation purposes—a promising application,” *J Mater Chem*, vol. 22, no. 20, pp. 10148–10151, May 2012, doi: 10.1039/C2JM15615F.
- [13] J. Ehrenmann, S. K. Henninger, and C. Janiak, “Water Adsorption Characteristics of MIL-101 for Heat-Transformation Applications of MOFs,” *Eur J Inorg Chem*, vol. 2011, no. 4, pp. 471–474, Feb. 2011, doi: 10.1002/EJIC.201001156.
- [14] H. Zhao, Q. Li, Z. Wang, T. Wu, and M. Zhang, “Synthesis of MIL-101(Cr) and its water adsorption performance,” 2020, doi: 10.1016/j.micromeso.2020.110044.
- [15] X. Zhang, X. Wang, W. Fan, and D. Sun, “Pore-Environment Engineering in Multifunctional Metal-Organic Frameworks,” *Chin J Chem*, vol. 38, no. 5, pp. 509–524, May 2020, doi: 10.1002/CJOC.201900493.
- [16] C. Zheng, D. Liu, Q. Yang, C. Zhong, and J. Mi, “Computational study on the influences of framework charges on CO₂ uptake in metal-organic frameworks,” *Ind Eng Chem Res*, vol. 48, no. 23, pp. 10479–10484, 2009, doi: 10.1021/IE901000X/ASSET/IMAGES/LARGE/IE-2009-01000X_0004.JPEG.
- [17] T. M. Al-Jadir and F. R. Siperstein, “The influence of the pore size in Metal–Organic Frameworks in adsorption and separation of hydrogen sulphide: A molecular simulation study,” *Microporous and Mesoporous Materials*, vol. 271, pp. 160–168, Nov. 2018, doi: 10.1016/J.MICROMESO.2018.06.002.
- [18] D. A. Reed *et al.*, “Reversible CO scavenging via adsorbate-dependent spin state transitions in an iron(II)-triazolate metal-organic framework,” *J Am Chem Soc*, vol. 138, no. 17, pp. 5594–5602, May 2016, doi: 10.1021/JACS.6B00248/SUPPL_FILE/JA6B00248_SI_002.CIF.
- [19] L. Geng *et al.*, “Redox property switching in MOFs with open metal sites for improved catalytic hydrogenation performance,” *J Alloys Compd*, vol. 888, p. 161494, Dec. 2021, doi: 10.1016/J.JALLCOM.2021.161494.

- [20] N. Abdollahi and A. Morsali, "Catalytic improvement by open metal sites in a new mixed-ligand hetero topic metal–organic framework," *Polyhedron*, vol. 159, pp. 72–77, Feb. 2019, doi: 10.1016/J.POLY.2018.11.045.
- [21] P. Goyal *et al.*, "Fe doped bimetallic HKUST-1 MOF with enhanced water stability for trapping Pb(II) with high adsorption capacity," *Chemical Engineering Journal*, vol. 430, p. 133088, Feb. 2022, doi: 10.1016/J.CEJ.2021.133088.
- [22] Ü. Kökçam-Demir *et al.*, "Coordinatively unsaturated metal sites (open metal sites) in metal–organic frameworks: design and applications," *Chem Soc Rev*, vol. 49, no. 9, pp. 2751–2798, May 2020, doi: 10.1039/C9CS00609E.
- [23] Y. Sun and H.-C. Zhou, "Recent progress in the synthesis of metal-organic frameworks," *Sci Technol Adv Mater*, vol. 16, p. 054202, 2015, doi: 10.1088/1468-6996/16/5/054202.
- [24] M. Ahmadi *et al.*, "An investigation of affecting factors on MOF characteristics for biomedical applications: A systematic review," *Heliyon*, vol. 7, no. 4, p. e06914, Apr. 2021, doi: 10.1016/J.HELIYON.2021.E06914.
- [25] B. E. Souza, A. F. Mö, K. Titov, J. D. Taylor, R. Rudić, and J.-C. Tan, "Green Reconstruction of MIL-100 (Fe) in Water for High Crystallinity and Enhanced Guest Encapsulation," 2020, doi: 10.1021/acssuschemeng.0c01471.
- [26] W. Li, T. Zhang, L. Lv, Y. Chen, W. Tang, and S. Tang, "Room-temperature synthesis of MIL-100(Fe) and its adsorption performance for fluoride removal from water," 2021, doi: 10.1016/j.colsurfa.2021.126791.
- [27] F. Jeremias, S. K. Henninger, and C. Janiak, "Ambient pressure synthesis of MIL-100(Fe) MOF from homogeneous solution using a redox pathway," *Dalton Transactions*, vol. 45, p. 8637, 2016, doi: 10.1039/c6dt01179a.
- [28] L. Garzón-Tovar, A. Carné-Sánchez, C. Carbonell, I. Imaz, and D. Maspoch, "Optimised room temperature, water-based synthesis of CPO-27-M metal–organic frameworks with high space-time yields," *J Mater Chem A Mater*, vol. 3, no. 41, pp. 20819–20826, Oct. 2015, doi: 10.1039/C5TA04923G.
- [29] M. J. Kalmutzki, N. Hanikel, and O. M. Yaghi, "Secondary building units as the turning point in the development of the reticular chemistry of MOFs," *Science Advances*, vol. 4, no. 10. 2018. doi: 10.1126/sciadv.aat9180.
- [30] M. J. Kalmutzki, C. S. Diercks, O. M. Yaghi, M. J. Kalmutzki, C. S. Diercks, and O. M. Yaghi, "Metal–Organic Frameworks for Water Harvesting from Air," *Advanced Materials*, vol. 30, no. 37, p. 1704304, Sep. 2018, doi: 10.1002/ADMA.201704304.

- [31] P. Küsgens *et al.*, “Characterization of metal-organic frameworks by water adsorption,” *Microporous and Mesoporous Materials*, vol. 120, no. 3, pp. 325–330, Apr. 2009, doi: 10.1016/J.MICROMESO.2008.11.020.
- [32] M. de Toni, R. Jonchiere, P. Pullumbi, F. X. Coudert, and A. H. Fuchs, “How Can a Hydrophobic MOF be Water-Unstable? Insight into the Hydration Mechanism of IRMOFs,” *ChemPhysChem*, vol. 13, no. 15, pp. 3497–3503, Oct. 2012, doi: 10.1002/CPHC.201200455.
- [33] J. Canivet, A. Fateeva, Y. Guo, B. Coasne, and D. Farrusseng, “Water adsorption in MOFs: fundamentals and applications,” *Chem Soc Rev*, vol. 43, no. 16, pp. 5594–5617, Jul. 2014, doi: 10.1039/C4CS00078A.
- [34] R. G. Pearson, “Hard and Soft Acids and Bases,” *J Am Chem Soc*, vol. 85, no. 22, pp. 3533–3539, Nov. 1963, doi: 10.1021/JA00905A001/ASSET/JA00905A001.FP.PNG_V03.
- [35] X. Liao, X. Wang, F. Wang, Y. Yao, and S. Lu, “Ligand Modified Metal Organic Framework UiO-66: A Highly Efficient and Stable Catalyst for Oxidative Desulfurization,” *J Inorg Organomet Polym Mater*, vol. 31, no. 2, pp. 756–762, Feb. 2021, doi: 10.1007/S10904-020-01808-Y/TABLES/2.
- [36] S. Yuan *et al.*, “Stable Metal–Organic Frameworks: Design, Synthesis, and Applications,” *Advanced Materials*, vol. 30, no. 37, p. 1704303, Sep. 2018, doi: 10.1002/ADMA.201704303.
- [37] Y. S. Hong, F. Li, S. L. Sun, Q. Sun, and M. Ye, “Highly Connected Metal-Organic Framework Constructed from Heptanuclear SBUs: Structure, Topology, and Fluorescence,” *J Solid State Chem*, vol. 274, pp. 315–321, Jun. 2019, doi: 10.1016/J.JSSC.2019.03.048.
- [38] Z. Jia, “Metal-Organic Framework Composites-Volume I,” *Materials Research Forum LLC Materials Research Foundations*, vol. 53, pp. 170–176, 2019, doi: 10.21741/9781644900291-8.
- [39] P. Ghosh, Y. J. Colón, and R. Q. Snurr, “Water adsorption in UiO-66: the importance of defects,” *Chemical Communications*, vol. 50, no. 77, pp. 11329–11331, Aug. 2014, doi: 10.1039/C4CC04945D.
- [40] H. Furukawa *et al.*, “Water adsorption in porous metal-organic frameworks and related materials,” *J Am Chem Soc*, vol. 136, no. 11, pp. 4369–4381, Mar. 2014, doi: 10.1021/JA500330A/SUPPL_FILE/JA500330A_SI_010.PDF.
- [41] H. Kim *et al.*, “Water harvesting from air with metal-organic frameworks powered by natural sunlight,” *Science (1979)*, vol. 356, no. 6336, pp. 430–434, Apr. 2017, doi: 10.1126/science.1257553.

10.1126/SCIENCE.AAM8743/SUPPL_FILE/AAM8743_KIM_SM.REVISED.PDF.

- [42] V. v. Butova, I. A. Pankin, O. A. Burachevskaya, K. S. Vetlitsyna-Novikova, and A. v. Soldatov, “New fast synthesis of MOF-801 for water and hydrogen storage: Modulator effect and recycling options,” *Inorganica Chim Acta*, vol. 514, p. 120025, Jan. 2021, doi: 10.1016/J.ICA.2020.120025.
- [43] N. Hanikel *et al.*, “Evolution of water structures in metal-organic frameworks for improved atmospheric water harvesting,” *Science (1979)*, vol. 374, no. 6566, pp. 454–459, Oct. 2021, doi: 10.1126/SCIENCE.ABJ0890/SUPPL_FILE/SCIENCE.ABJ0890_SM.PDF.
- [44] P. M. Schoenecker, C. G. Carson, H. Jasuja, C. J. J. Flemming, and K. S. Walton, “Effect of water adsorption on retention of structure and surface area of metal-organic frameworks,” *Ind Eng Chem Res*, vol. 51, no. 18, pp. 6513–6519, May 2012, doi: 10.1021/IE202325P/SUPPL_FILE/IE202325P_SI_001.PDF.
- [45] A. de Oliveira, G. F. de Lima, and H. A. de Abreu, “Structural and electronic properties of M-MOF-74 (M = Mg, Co or Mn),” *Chem Phys Lett*, vol. 691, pp. 283–290, Jan. 2018, doi: 10.1016/J.CPLETT.2017.11.027.
- [46] W. Zhou, H. Wu, and T. Yildirim, “Enhanced H₂ adsorption in isostructural metal-organic frameworks with open metal sites: Strong dependence of the binding strength on metal ions,” *J Am Chem Soc*, vol. 130, no. 46, pp. 15268–15269, Nov. 2008, doi: 10.1021/JA807023Q/SUPPL_FILE/JA807023Q_SI_001.PDF.
- [47] A. Javed, I. Strauss, H. Bunzen, J. Caro, and M. Tiemann, “Humidity-Mediated Anisotropic Proton Conductivity through the 1D Channels of Co-MOF-74,” *Nanomaterials*, vol. 10, no. 7, pp. 1–9, Jul. 2020, doi: 10.3390/NANO10071263.
- [48] M. H. Rosnes, B. Pato-Doldán, R. E. Johnsen, A. Mundstock, J. Caro, and P. D. C. Dietzel, “Role of the metal cation in the dehydration of the microporous metal-organic frameworks CPO-27-M,” *Microporous and Mesoporous Materials*, vol. 309, p. 110503, Dec. 2020, doi: 10.1016/J.MICROMESO.2020.110503.
- [49] M. H. Rosnes *et al.*, “Intriguing differences in hydrogen adsorption in CPO-27 materials induced by metal substitution,” *J Mater Chem A Mater*, vol. 3, no. 9, pp. 4827–4839, Feb. 2015, doi: 10.1039/C4TA05794E.
- [50] P. D. C. Dietzel *et al.*, “An In Situ High-Temperature Single-Crystal Investigation of a Dehydrated Metal-Organic Framework Compound and Field-Induced Magnetization of One-Dimensional Metal-Oxygen Chains,”

Angewandte Chemie International Edition, vol. 44, no. 39, pp. 6354–6358, Oct. 2005, doi: 10.1002/ANIE.200501508.

- [51] W. Zhou, H. Wu, and T. Yildirim, “Supporting Information Enhanced H₂ Adsorption in Isostructural Metal-Organic Frameworks with Open Metal Sites: Strong Dependence of the Binding Strength on Metal Ions I. Synthetic procedures”.
- [52] T. Grant Glover, G. W. Peterson, B. J. Schindler, D. Britt, and O. Yaghi, “MOF-74 building unit has a direct impact on toxic gas adsorption,” *Chem Eng Sci*, vol. 66, no. 2, pp. 163–170, Jan. 2011, doi: 10.1016/J.CES.2010.10.002.
- [53] P. Horcajada *et al.*, “Synthesis and catalytic properties of MIL-100(Fe), an iron(III) carboxylate with large pores,” *Chemical Communications*, no. 27, pp. 2820–2822, Jul. 2007, doi: 10.1039/B704325B.
- [54] Y.-R. Chen, K.-H. Liou, D.-Y. Kang, J.-J. Chen, and L.-C. Lin, “Investigation of the Water Adsorption Properties and Structural Stability of MIL-100(Fe) with Different Anions,” *Langmuir*, vol. 34, no. 14, pp. 4180–4187, Apr. 2018, doi: 10.1021/acs.langmuir.7b04399.
- [55] W. Lu *et al.*, “Tuning the structure and function of metal–organic frameworks via linker design,” *Chem Soc Rev*, vol. 43, no. 16, pp. 5561–5593, Jul. 2014, doi: 10.1039/C4CS00003J.
- [56] J. F. Moulder, W. F. Stickle, P. E. ’ Sobol, K. D. Bomben, and J. Chastain, “Handbook of X-ray Photoelectron Spectroscopy A Reference Book of Standard Spectra for Identification and Interpretation of XPS Data.”
- [57] “X-ray Fluorescence and Moseley’s Law 1 Background 1.1 Ordering of the periodic table”.
- [58] B. R. Strohmeier and D. M. Hercules, “Surface Spectroscopic Characterization of Mn/Al₂O₃ Catalysts,” *J. Phys. Chem*, vol. 88, pp. 4922–4929, 1984, Accessed: Sep. 23, 2022. [Online]. Available: <https://pubs.acs.org/sharingguidelines>
- [59] Z. Huang *et al.*, “High performance of Mn-Co-Ni-O spinel nanofilms sputtered from acetate precursors,” *Scientific Reports 2015 5:1*, vol. 5, no. 1, pp. 1–8, Jun. 2015, doi: 10.1038/SREP10899.
- [60] S. Xie *et al.*, “MOF-74-M (M = Mn, Co, Ni, Zn, MnCo, MnNi, and MnZn) for low-temperature NH₃-SCR and in situ Drifts study reaction mechanism,” *ACS Appl Mater Interfaces*, vol. 12, no. 43, pp. 48476–48485, Oct. 2020, doi: 10.1021/ACSAMI.0C11035/ASSET/IMAGES/LARGE/AM0C11035_0014.JPG.

- [61] J. Sun, X. Zhang, A. Zhang, and C. Liao, "Preparation of Fe-Co based MOF-74 and its effective adsorption of arsenic from aqueous solution," 2018, doi: 10.1016/j.jes.2018.12.013.
- [62] P. Torelli, E. A. Soares, G. Renaud, S. Valeri, X. X. Guo, and P. Luches, "Nano-structuration of CoO film by misfit dislocations", doi: 10.1016/j.susc.2006.11.063.
- [63] Y. C. Wang, W. B. Li, L. Zhao, and B. Q. Xu, "MOF-derived binary mixed metal/metal oxide @carbon nanoporous materials and their novel supercapacitive performances," *Physical Chemistry Chemical Physics*, vol. 18, no. 27, pp. 17941–17948, Jul. 2016, doi: 10.1039/C6CP02374F.
- [64] M. Li *et al.*, "High-performance asymmetric supercapacitors based on monodisperse MnO nanocrystals with high energy densities," *Nanoscale*, vol. 10, no. 34, pp. 15926–15931, Aug. 2018, doi: 10.1039/C8NR04541K.
- [65] J. P. Bonnelle, J. Grimblot, and A. D'huysser, "Influence de la polarisation des liaisons sur les spectres esca des oxydes de cobalt," *J Electron Spectros Relat Phenomena*, vol. 7, no. 2, pp. 151–162, Jan. 1975, doi: 10.1016/0368-2048(75)80047-8.
- [66] V. di Castro and G. Polzonetti, "XPS study of MnO oxidation," *J Electron Spectros Relat Phenomena*, vol. 48, no. 1, pp. 117–123, Jan. 1989, doi: 10.1016/0368-2048(89)80009-X.
- [67] J. Haber and L. Ungier, "On chemical shifts of ESCA and Auger lines in cobalt oxides," *J Electron Spectros Relat Phenomena*, vol. 12, no. 3, pp. 305–312, 1977, doi: 10.1016/0368-2048(77)85081-0.
- [68] Y. C. G. Kwan, G. M. Ng, and C. H. A. Huan, "Identification of functional groups and determination of carboxyl formation temperature in graphene oxide using the XPS O 1s spectrum," *Thin Solid Films*, vol. 590, pp. 40–48, Sep. 2015, doi: 10.1016/J.TSF.2015.07.051.
- [69] A. R. Kim *et al.*, "Facile loading of Cu(I) in MIL-100(Fe) through redox-active Fe(II) sites and remarkable propylene/propane separation performance," *Chemical Engineering Journal*, vol. 331, pp. 777–784, Jan. 2018, doi: 10.1016/J.CEJ.2017.09.016.
- [70] F. Zhang, J. Shi, Y. Jin, Y. Fu, Y. Zhong, and W. Zhu, "Facile synthesis of MIL-100(Fe) under HF-free conditions and its application in the acetalization of aldehydes with diols," *Chemical Engineering Journal*, vol. 259, pp. 183–190, Jan. 2015, doi: 10.1016/J.CEJ.2014.07.119.

- [71] Z. Li and U. Becker, "Chemical state effects on the Auger transitions in Cr, Fe, and Cu compounds," *J Electron Spectros Relat Phenomena*, vol. 237, p. 146893, Dec. 2019, doi: 10.1016/J.ELSPEC.2019.146893.
- [72] P. S. Bagus, C. J. Nelin, C. R. Brundle, B. V. Crist, N. Lahiri, and K. M. Rosso, "Combined multiplet theory and experiment for the Fe 2p and 3p XPS of FeO and Fe₂O₃," *J Chem Phys*, vol. 154, no. 9, p. 094709, Mar. 2021, doi: 10.1063/5.0039765.
- [73] A. R. Kim *et al.*, "Facile loading of Cu(I) in MIL-100(Fe) through redox-active Fe(II) sites and remarkable propylene/propane separation performance," *Chemical Engineering Journal*, vol. 331, pp. 777–784, Jan. 2018, doi: 10.1016/J.CEJ.2017.09.016.
- [74] J. Woong Yoon *et al.*, "Controlled Reducibility of a Metal–Organic Framework with Coordinatively Unsaturated Sites for Preferential Gas Sorption," *Angewandte Chemie International Edition*, vol. 49, no. 34, pp. 5949–5952, Aug. 2010, doi: 10.1002/ANIE.201001230.
- [75] M. C. Simons *et al.*, "Beyond Radical Rebound: Methane Oxidation to Methanol Catalyzed by Iron Species in Metal–Organic Framework Nodes," *J Am Chem Soc*, vol. 143, no. 31, pp. 12165–12174, Aug. 2021, doi: 10.1021/JACS.1C04766/SUPPL_FILE/JA1C04766_SI_002.ZIP.
- [76] G. Vinai *et al.*, "An integrated ultra-high vacuum apparatus for growth and in situ characterization of complex materials," *Review of Scientific Instruments*, vol. 91, no. 8, p. 085109, Aug. 2020, doi: 10.1063/5.0005302.
- [77] R. P. Kavali, J. Tonannavar, J. Bhovi, and J. Tonannavar, "Study of OH···O bonded-cyclic dimer for 2,5-Dihydroxyterephthalic acid as aided by MD, DFT calculations and IR, Raman, NMR spectroscopy," *J Mol Struct*, vol. 1264, p. 133174, Sep. 2022, doi: 10.1016/J.MOLSTRUC.2022.133174.
- [78] C. Castán-Guerrero *et al.*, "A reaction cell for ambient pressure soft x-ray absorption spectroscopy," *Review of Scientific Instruments*, vol. 89, no. 5, p. 054101, May 2018, doi: 10.1063/1.5019333.